Universidade do Minho
Escola de Ciências

Samantha Faria Oliveira da Costa

Development of a skin-on-a-chip device for toxicological evaluation of nanomaterials

Development of a skin-on-a-chip device for toxicological evaluation of nanomaterials

Samantha Costa

UMinho | 2022

October 2022

INTERNATIONAL IBERIAN NANOTECHNOLOGY LABORATORY

Universidade do Minho
Escola de Ciências

Samantha Faria Oliveira da Costa

Development of a skin-on-a-chip device for toxicological evaluation of nanomaterials

Master Thesis
Master's Degree in Biophysics and Bionanosystems

Work developed under the supervision of
Dr. Ana Rosa Lopes Pereira Ribeiro
and
Prof. Dr. Cacilda Maria Lima de Moura

October 2022

AGRADECIMENTOS

A presente dissertação representa um enorme marco a nível profissional e pessoal e, como tal, gostaria de deixar um agradecimento especial a todos os que contribuíram direta ou indiretamente ao longo destes dois anos de mestrado.

Em primeiro lugar, gostaria de expressar a minha sincera gratidão à minha orientadora, Doutora Ana Rosa Lopes Pereira Ribeiro, por me conceder a oportunidade de trabalhar neste projeto emocionante e interdisciplinar. Pela amizade, motivação e ajuda imprescindível no desenvolvimento do meu pensamento crítico e científico, foi um pilar fundamental nesta fase da minha formação académica.

Igualmente agradeço à minha co-orientadora, Professora Doutora Cacilda Maria Lima de Moura, pelo apoio, auxílio, conselhos e esclarecimentos dados.

To the Nanosafety group, I want to express my gratitude. I could always count on each of you, and all of you were a huge part of my professional growth in the past year. I can say that without any doubt I chose the right project to be in.

To the Food Processing and Nutrition group, I want to thank you for all your help and support.

Aos meus colegas de mestrado, Ricardo, Hugo e Daniela, pela amizade, boa disposição e, sobretudo pelo carinho com que me ajudaram sempre que precisei.

Um enorme obrigada ao meu namorado, João Sousa, pela paciência, incentivo e apoio incondicional, e a todos os amigos que percorreram este caminho ao meu lado, Sara, Clara, Mónica, Paulo, Rodrigo e Rafa, por também acreditarem em mim.

Por fim, palavras não expressam o quanto tenho de agradecer aos meus pais, irmão e família, por me colocarem como prioridade para que eu tenha uma vida melhor, por me ajudarem, ampararem e serem a minha inspiração e o meu porto de abrigo desde sempre.

STATEMENT OF INTEGRITY

I hereby declare having conducted this academic work with integrity. I confirm that I have not used plagiarism or any form of undue use of information or falsification of results along the process leading to its elaboration.

I further declare that I have fully acknowledged the Code of Ethical Conduct of the University of Minho.

Desenvolvimento de um dispositivo microfluídico de pele humana reconstruída para avaliação toxicológica de nanomateriais

RESUMO

A pele é o maior órgão do corpo humano e está constantemente exposta a partículas nanométricas provenientes de poluentes ambientais (partículas ultrafinas) bem como cosméticos (protetores solares contendo nanopartículas de dióxido de titânio). Estas ocorrências resultam em várias reações com consequências adversas significativas para a saúde, como envelhecimento precoce da pele, alergias, pigmentação excessiva, agravamento dos quadros de psoríase e em último caso cancro da pele.

Atualmente, não há diretrizes da OCDE ou ISO para avaliar a nanotoxicidade *in-vitro*, nem revisões das diretrizes de toxicocinética para avaliar o impacto desses nanomateriais na pele ou o seu potencial para provocar danos permanentes. Modelos animais são amplamente utilizados para a compreensão das condições de saúde e das doenças da pele humana, bem como na fase pré-clínica para determinar o mecanismo de ação de cosméticos. No entanto, os modelos animais geralmente não são concisos e não conseguem prever a resposta humana devido a diferenças na anatomia, fisiologia e imunidade da pele, para além de desencadear várias preocupações éticas. Novos modelos capazes de replicar a fisiologia de órgãos bem como a resposta sistémica do corpo humano à exposição de nanomateriais são essenciais.

A tecnologia *organ-on-a-chip* apesar de estar repleta de desafios biológicos e de engenharia tem o potencial de revolucionar a avaliação de risco de nanomateriais de próxima geração. Assim, estimar a toxicidade na pele humana de nanomateriais manufaturados, bem como acidentais, em sistemas baseados em microfluídica, torna-se urgente e necessário.

O principal objetivo deste trabalho foi desenvolver e otimizar um sistema biomimético da epiderme com perfusão dinâmica e com uma arquitetura modular que permita a avaliação da toxicidade de nanomateriais. Nanopartículas de dióxido de titânio previamente caracterizadas foram introduzidas no dispositivo microfluídico e a sua toxicidade avaliada.

PALAVRAS-CHAVE: dispositivo microfluídico de pele humana, epiderme, queratinócitos, nanopartículas de dióxido de titânio, nanotoxicologia.

ABSTRACT

The skin is the largest organ in the human body and is constantly exposed to airborne nano-sized and ultrafine particles from environmental pollutants and cosmetics containing nanomaterials, such as sun protectors containing titanium dioxide nanoparticles. This results in several reactions that have significant adverse health consequences, such as early skin aging, allergies, pigmentation, worsening of psoriasis, and ultimately skin cancer.

Currently, there are no OECD or ISO guidelines for assessing *in-vitro* nanotoxicity, or revisions to toxicokinetics guidelines for evaluating the impact of these nanomaterials on the skin, or their potential to cause permanent harm. Animal models are widely used in basic research for understanding the health and disease conditions of human skin, as well as in the preclinical stage to determine the mechanism of action of drugs and cosmetics. However, animal models often poorly predict the human response due to differences in skin anatomy, physiology, and immunity as well as involving ethical concerns. New models capable of replicating human physiology and interactions with systemic responses of the human body are essential.

Organ-on-a-chip technology is filled with engineering and biological challenges, but it has the potential to revolutionize the next-generation risk assessment of nanomaterials. Taking that into consideration, estimating the skin human toxicity effect of engineered, as well as accidental nanomaterials, in microfluidic-based systems, becomes an urgent and much-needed task.

The main aim of this work was to develop and optimize a biomimetic epidermis-on-a-chip system with dynamic perfusion and a modular architecture to allow the assessment of the toxicity of nanomaterials. Titanium dioxide nanoparticles well-characterized were introduced into the microfluidic device, and their effect on epidermis toxicity was assessed.

KEY-WORDS: skin-on-a-chip, epidermis, keratinocytes, titanium dioxide nanoparticles, nanotoxicology.

TABLE OF CONTENTS

LIST OF ABBREVIATIONS AND ACRONYMS

2D – Two-dimensional

3D – Three-dimensional

Ag – Silver

AgCl – Silver chloride

ALI – Air-liquid interface

AOP – Adverse outcome pathway

Au – Gold

BE – Binding energy

BM – Basement membrane

BPE – Bovine pituitary extract

BSA – Bovine serum albumin

CAD – Computer-aided design

CDK4 – Cyclin-dependent kinase 4

CNC – Computer numerically controlled

CO_2 – Carbon dioxide

DAPI – 4′,6-diamidino-2-phenylindole

DEJ – Dermal-epidermal junction

DLS – Dynamic light scattering

DMEM – Dulbecco's Modified Eagle Medium

DPRA – Direct peptide reactivity assay

ECM – Extracellular matrix

EGF – Epidermal growth factor

ELISA – Enzyme-Linked Immunosorbent Assay

EoC – Epidermis-on-a-chip

FBS – Fetal bovine serum

Fe_2O_3 – Iron III oxide

FEM – Finite element modeling

FITC-Dextran – Fluorescein isothiocyanate-dextran

FT – Full-thickness

FTIR – Fourier transform infrared spectroscopy

GPMT – Guinea pig maximization test

HBSS – Hank's Balanced Salt Solution

h-CLAT – Human cell activation test

H&E – Hematoxylin and eosin

HaCaT – Spontaneously transformed aneuploid immortal keratinocyte cell line from adult human skin

HDFs – Human dermal fibroblasts

HEKn – Human epidermal keratinocytes neonatal

HPV-16 – Human papillomavirus type 16

HPV-18 – Human papillomavirus type 18

HSEs – Human skin equivalents

hTERT – Telomerase reverse transcriptase in humans

IARC – International Agency for Research on Cancer

ICCVAM – Interagency Coordinating Committee on the Validation of Alternative Methods

iEoC – Integrated epidermis-on-a-chip

IL-6 – Interleukin 6

iPSC – Induced pluripotent stem cells

ISO – International Organization for Standardization

K10 – Keratin-10

K14 – Keratin-14

KE – Kinetic energy

LCE – Laser cutter and engraving

LLNA – Local lymph node assay

Milli-Q – Tri-distilled water

MTT assay – (3-(4,5-dimethylthiazol-2-yl)-2,5-diphenyltetrazolium bromide) tetrazolium reduction assay

Multi-OoC – Multi-organ-on-a-chip

$NaHCO_3$ – Sodium bicarbonate

NHKs – Normal human keratinocytes

NIKS – Near-diploid spontaneous immortalized human keratinocytes

NMs - Nanomaterials

NPs – Nanoparticles

OECD – Organization for Economic Co-operation and Development

OoC – Organ-on-a-chip

PAMAM – Poly(amidoamine)

PBS – Phosphate buffered saline

PCTE – Polycarbonate

PDI – Polydispersity index

PDMS – Polydimethylsiloxane

PEG – Polyethylene glycol

Pen/strep – Penicillin/streptomycin

PET – Polyethylene terephthalate

PFA – Paraformaldehyde

PMMA – Polymethylmethacrylate

PTFE – Polytetrafluoroethylene

Q-dots – Quantum dots

RHE – Reconstructed human epidermis

Re – Reynolds number

ROS – Reactive oxygen species

RT – Room temperature

RT-PCR – Reverse transcription-polymerase chain reaction test

SB – Stratum basale

SC – Stratum corneum

SCC – Squamous cell carcinoma

SCCS – Scientific Committee on Consumer Safety

SDS – Sodium dodecyl sulfate

SG – Stratum granulosum

SL – Stratum lucidum

SoC – Skin-on-a-chip

SOP – Standard Operating Procedures

SS – Stratum spinosum

TEER – Trans-epithelial electrical resistance

TER – Transcutaneous electrical resistance

TNF-α – Transforming growth factor alpha

TGF-β – Transforming growth factor beta

TiO_2 – Titanium dioxide

TJs – Tight junctions

TRITC – Tetramethyl rhodamine isothiocyanate

XPS – X-ray photoelectron spectroscopy

XRD – X-ray diffraction

ZnO – Zinc oxide

LIST OF FIGURES

LIST OF TABLES

CHAPTER 1

INTRODUCTION

1.1 Motivation

The unique physicochemical properties of nanomaterials (NMs) allow their exponential growth and use in the cosmetic industry. However, their small size and strong ability to permeate biological barriers bring concerns about their potential toxicity to consumers.

The skin is the largest organ in the human body, and it has been demonstrated that nanoparticles (NPs) found in numerous cosmetics may penetrate the *stratum corneum* and reach the viable epidermis through various pathways. Depending on their size, these NPs may then enter the blood circulation and possibly cause systemic effects. Recently the International Agency for Research on Cancer (IARC) determined titanium dioxide as possibly carcinogenic to humans, posing a health risk to consumers and increasing the need for research in this field [1].

Data regarding the potential of dermal absorption and/or penetration of titanium dioxide nanoparticles (TiO_2 NPs) from sunscreens exhibit controversial results. Although several articles describe the inexistence of skin penetration and permeation of nanoparticles, other ones demonstrated the opposite effect revealing that TiO_2 NPs may penetrate the skin and have toxic effects on skin cells due to the release of reactive oxygen species (ROS) [2, 3]. Taking that into consideration, exploring the effect of TiO_2 NPs in skin cells mimicking real conditions is urgently needed.

Currently, the safety assessment of NMs applied in cosmetics uses essentially two-dimensional (2D) skin cell monolayers that cannot reproduce the highly complex and dynamic skin environment. While more effective than conventional 2D cultures, recent developments in three-dimensional (3D) cultures, are still far from simulating the complex *in-vivo-like* interactions between cells and the extracellular matrix. Additionally, they are unable to reproduce the systemic response of the body. Animal models, on the other hand, may simulate the complex interactions between organs and provide a systemic response, but the results cannot be extrapolated to humans. Furthermore, ethical guidelines dictate that animal models should be replaced, reduced, and refined, established as the 3R principle [4]. Consequently, there is a strong need for cosmetic, pharmacological, and toxicological sciences to replace those methods with reliable, reproducible, and high-yield alternative approaches.

Platforms known as organ-on-a-chip (OoC) have been developed as a result of the latest innovations at the interface of microscale technology and tissue engineering. By mimicking *in-vivo* tissue composition, function, and environment, these platforms aim to close the gap between human biology and current *in-*

vitro models. This thesis project consisted of the design and fabrication of an epidermis-on-a-chip (EoC) device for the safety assessment of TiO_2 NPs as well as other possible NMs used in cosmetics.

1.2 Context and Objectives

This dissertation was developed under the umbrella of the innovative and ambitious SiNfONiA project founded by the European Union's Horizon 2020. The main goal to be achieved was to establish a microfluidic device that can simulate the epidermis microenvironment, to become an ideal tool for nanomaterials screening and toxicity evaluation. It is contextualized within the scope of the research Nanosafety group, taking place at the International Iberian Nanotechnology Laboratory, under the supervision of Dr. Ana Rosa Lopes Pereira Ribeiro[1] and Prof. Dr. Cacilda Maria Lima de Moura[2].

Specifically, the objectives were:

→ Design and fabrication of a microfluidic device to cultivate and growth of an epidermis;

→ Establish an EoC and its complete characterization;

→ Toxicological evaluation of rutile TiO_2 NPs in the EoC model.

1.3 Dissertation Outline

In this first chapter – **Chapter 1** – an introduction to cosmetic nanoformulations and mechanisms of penetration and permeation of NPs is provided, as well as an introduction to the anatomy and physiology of the skin. The most important biological and technical aspects of producing a biomimetic microfluidic OoC are described, and the EoC models reported in the literature up to this point are also presented in detail to provide a background for the development of an EoC device for toxicological evaluation of NMs. **Chapter 2** contains the materials, methods, and techniques applied for the characterization and dispersion of the NPs. The cell culture protocols and procedures used are also described, as the optimizations implemented to design and build a dynamic microfluidic device. **Chapter 3** presents the results obtained and a detailed discussion of them. **Chapter 4** concludes this thesis with a summary of the obtained results and presents some expected future perspectives. Lastly, in **Chapter 5**, the references used throughout this thesis dissertation are presented.

[1] Staff Researcher of International Iberian Nanotechnology Laboratory.

[2] Assistant Professor at the University of Minho, working in the field of materials characterization by Raman spectroscopy.

1.4 Scientific Output

The work carried out as part of this MSc thesis yields a flash talk describing some stages of the development of a skin-on-a-chip device, that was presented at the INL Annual Research Symposium 2022, and the following group review papers:

→ F. Lebre, N. Chatterjee, S. Costa, E. Fernández-de-Gortari, C. Lopes, J. Meneses, L. Ortiz, A. R. Ribeiro, V. Vilas-Boas, and E. Alfaro-Moreno. Nanosafety: An Evolving Concept to Bring the Safest Possible Nanomaterials to Society and Environment. Nanomaterials. 2022. Nanomaterials impact factor: 4.9.

→ S. Costa, V. Vilas-Boas, F. Lebre, J.M Granjeiro, C.M Catarino, L Moreira Teixeira, P. Loskill, Ernesto Alfaro-Moreno, A. R. Ribeiro. Microfluidic-assisted skin-on-chip systems for the next-generation risk assessment of nanomaterials, in preparation, to submit to Trends in Biotechnology Journal (invited review accepted by the editor). Trends in Biotechnology impact factor 19.5.

1.5 Toxicological Evaluation of Nanomaterials used in Cosmetic Applications

Nanotechnologies involve designing and producing objects or structures at a very small scale. According to the International Organization for Standardization, NMs are defined as natural, incidental, or manufactured materials containing particles (unbound, aggregated, agglomerated state), where 50% or more of the particles, have one or more external dimensions in the size range between 1 and 100 nm [2].

NMs occur ubiquitously in the environment, resulting from both natural processes and anthropogenic sources. They can be usually grouped into four types: a) carbon-based materials such as carbon nanotubes and fullerenes; b) metal-based materials such as gold (Au), silver (Ag), quantum dots (Q-dots), and metal-oxides like titanium dioxide (TiO_2), zinc oxide (ZnO) and iron III oxide (Fe_2O_3); c) dendrimers or nanosized polymers; and d) composites combining particles with other NPs and/or larger bulk-type materials [5].

Due to their unique interesting properties, NMs have gained great attention in recent years. They have been found in applications such as healthcare, electronics, cosmetics, textiles, information technology, and environmental protection. Its properties are not always well-characterized, calling for risk assessment of possible exposures arising during their manufacture and use. Oral, dermal, inhalation, and injection

routes are considered the main entry of NMs into the human body raising issues about their potential toxicity [5].

Cosmetics are “articles intended to be rubbed, poured, sprinkled, or sprayed on, introduced into, or otherwise applied to the human body or any part thereof for cleansing, beautifying, promoting attractiveness, or altering the appearance” [6].

The consumer product inventory refers that since 2006, NP-containing cosmetics have shown a large diffusion. It has been estimated that cosmetic products contain TiO_2 NPs (70/80%), ZnO NPs (70%), and Ag NPs (20%). TiO_2 NPs have been one of the predominant NMs synthesized and present in cosmetic products like sunscreens, food colors, and supplements nutritional. In cosmetics, TiO_2 NPs are applied as inorganic physical sun-blockers due to their photoprotective capacity with the advantage of being transparent to visible light [7, 8].

Carbon-based NPs are also marketed as components of cosmetics (fullerenes). As combustion products, fullerenes are found in low concentrations in nature and have antioxidant qualities that make them attractive for cosmetic use [8].

Dendrimers are covalently linked macromolecule NPs that are used as carriers for drug delivery, gene delivery, tissue targeting, solubilization, and other applications. The type of the terminal groups, which are classified as anionic, cationic, or neutral, determines the toxicity of dendrimers (e.g., carboxylate, amino, and polyethylene glycol (PEG), respectively). Dendrimers of the poly(amidoamine) (PAMAM) class are the most abundant and well-studied. PAMAM dendrimers are non-biodegradable, making them suitable for external use as pharmaceuticals with no evidence of systemic absorption [8].

Q-dots are NPs with a metalloid crystalline core and a hydrocarbon shell, with a diameter of 2 to 10 nm, which have unique diameter-dependent optical properties (e.g., photoluminescence and electroluminescence). Generally, Q-dots do not penetrate the viable epidermis of human skin, but they do accumulate in the infundibulum of hair follicles [8].

Liposomes are composed of small molecules held together by intermolecular forces resulting in stable nanoparticulate properties. They are usually spherical vesicles with an intra-liposomal aqueous phase created by a single or several continuous lipid bilayer/s separating the external aqueous medium from the intra-liposomal aqueous core. Liposomes are simple to produce and reasonably safe because they are composed of commercially available substances with recognized toxicity levels. Lipid vesicles can

help improve medication delivery for molecules with low solubility or permeability, as well as target pharmaceuticals to specific tissues, improve pharmacokinetics, and reduce adverse effects [8].

The skin penetration and permeation of NPs are affected by many factors, including their primary size, physicochemical properties (such as rigidity/flexibility of the nanostructure, dissolution rate in water/sweat, and morphology), and skin physiology. It is considered that NPs behave like large molecules and modeled their rate of penetration using diffusion theory, being that only particles of 1 nm or less are small enough to pass through intact skin. One would further assume that in healthy, intact skin, NPs larger than 4 nm (maximum intercellular space) cannot normally penetrate. However, there are experimental data that show that NPs larger than this size can pass through disrupted skin where intercellular gaps are larger than in normal skin. Even, the *in-vitro* and *in-vivo* data regarding the potential of dermal absorption and/or penetration of TiO_2 NPs from sunscreens exhibit controversial results [9, 10, 11]. Although several articles describe the opposite, the penetration of TiO_2 NPs in healthy as well as in damaged or lesioned skin (such as in cases of scarring, sunburn, and depilated skin) is demonstrated by the scientific community. It is important to refer that, the characterization techniques employed to evaluate NPs skin penetration sometimes entering in the detection limit of the equipment, contributing to this controversy [2, 12].

The mechanism of NPs penetration was not yet clarified, though, it is suggested that they may penetrate the *stratum corneum* reaching viable epidermis using different pathways that include the transcellular and paracellular transports, as well as hair follicles (transappendageal), sweat glands, skin folds or a combination of all (**Figure 1**) [2, 12, 3].

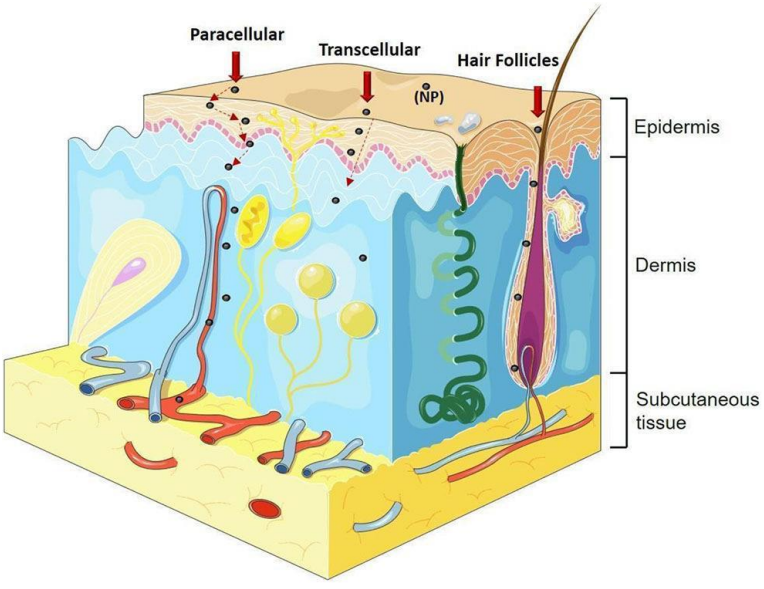

Figure 1 – Different pathways of NPs penetration *[2]*.

Upon NPs penetration, it has been shown that their interaction with skin proteins and skin cells can potentially lead to skin absorption, irritation, toxicity, corrosivity as well as sensitization [2, 5]. Some *in-vitro* literature already described that TiO_2 NPs induce toxicity, inflammation, and genetic modifications, due to oxidative stress, since TiO_2 NPs can trigger the formation of reactive oxygen species (ROS) [3].

One of the Scientific Committee on Consumer Safety's (SCCS) responsibilities is to recommend a set of guidelines for the cosmetic industries to consider when developing studies for use in the safety evaluation of cosmetic substances. According to Article 3 of the Cosmetics Regulation, a cosmetic product available for purchase must be safe for human health when used under normal or reasonably foreseeable conditions [6, 13].

Currently, the safety assessment of nanomaterials applied in cosmetics is carried out on a 2D monolayer of skin cells, and there are also commercially available 3D skin models as well as *in-house* constructs with several levels of biological complexity. . However, most of them lack the biological complexity of skin as well as its dynamic environment [2].

Skin irritation is defined as the formation of "reversible skin damage after the administration of a test material for up to 4 hours". Some *in-vitro* skin irritation tests have been officially validated, such as EpiSkin™, EpiDerm™, and SkinEthic™ reconstructed human epidermis (RHE). The main disadvantage of RHE it is that is not possible to distinguish the basal, *spinosum*, and *granulosum stratum*, which are important issues for penetration studies. Companies are also developing 3D skin models incorporating melanocytes (e.g., MelanoDerm™), and a full-thickness (FT) skin model, commercially known as EpiDerm-FT™, that consists of an epidermis and dermis (keratinocytes and fibroblasts) layers (**Figure 2**) [2, 13].

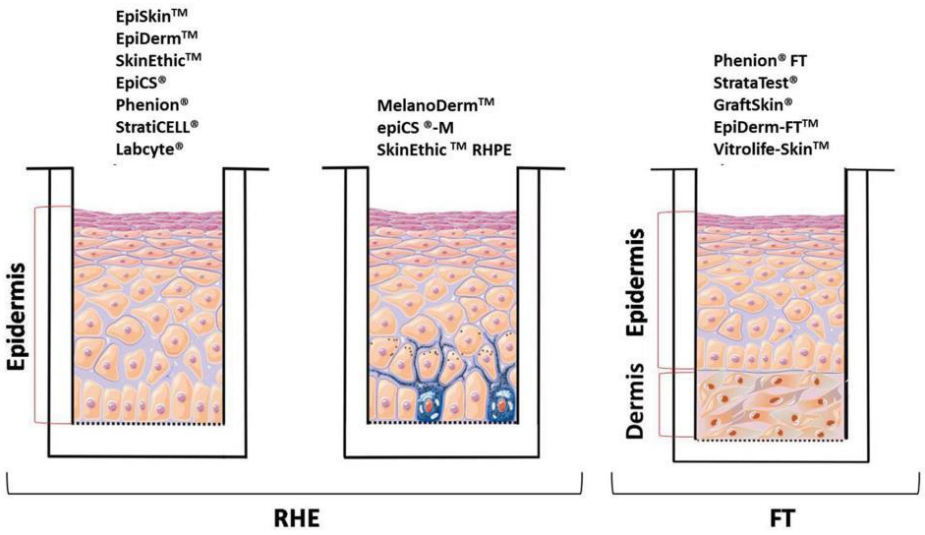

Figure 2 – Scheme of the main 3D skin models used *[2]*.

Chronic toxicity is a result of long-term exposure to a chemical that causes chronic or progressively deteriorating dysfunction of cells, organs, or multiple organ systems. When it comes to producing cosmetic compounds with specific biological features that will come into contact with human skin for extended periods, assessing systemic risk is an important factor in evaluating the safety of these new ingredients. There are no generally recognized alternatives to the traditional repeated dose toxicity *in-vivo* experiments. As a result, the SCCS believes that long-term animal tests to explore one or more potential toxic effects are still necessary in some cases [13].

Skin corrosion is defined as the formation of permanent tissue damage to the skin, and apparent necrosis through the epidermis and into the dermis. Corrosivity isn't something expected to find in cosmetics, but it can happen due to a production issue or consumer misuse. The rat skin Transcutaneous Electrical Resistance test (TER), which is technically an *ex-vivo* approach because a laboratory animal (rat) is required to obtain the skin with subsequent assessment of the TER, is one of the *in-vitro* procedures used to evaluate skin corrosion. Nonetheless, the SCCS expressed concerns about and believed that this method did not provide sufficient proof that this test could be used as a suitable endpoint to test cosmetic substances for their potential skillfulness [13].

On the other hand, one of the most prevalent cosmetics-related issues is skin sensitization. Skin sensitization consists of a type IV hypersensitivity response triggered in susceptible individuals after repeated dermal exposure to a potential allergenic material. The Mouse Local Lymph Node Assay (LLNA) and its non-radioactive modifications, the Guinea Pig Maximization Test (GPMT), and the Buehler occluded patch test are all accepted *in-vivo* animal testing methods for skin sensitization potential assessment. One of the last *in-vitro* methods is the human cell activation test (h-CLAT), which is based on the activation of the human monocytic leukemia cell line THP-1. Other were accepted in 2015, including Test 442C, the *in-chemico* Skin Sensitization: Direct Peptide Reactivity Assay (DPRA), and Test 442D, the *in-vitro* Skin Sensitization: ARE-Nrf2 Luciferase Test Method. These methods rely on cell systems that are capable of differentiating between sensitizers and non-sensitizers based on cytokine release profiles. They are, however, still in the early stages of research [13, 14].

1.6 Skin: Anatomy and Physiology

The skin is the largest organ in the human body and represents about 15% of the total adult body weight. It provides a protective physical barrier between the body and the environment, preventing losses of water

and electrolytes, reducing penetration by chemicals, and ultraviolet (UV) radiation, and protecting against pathogenic microorganisms. The skin also performs crucial functions for life such as thermoregulation and immunological surveillance [15].

The skin is simply structured in three layers, including from inner to outermost: a) hypodermis, b) dermis, separated from the epidermis by the dermal-epidermal junction, and c) epidermis (and its associated appendages, pilosebaceous follicles, and sweat glands) (**Figure 3**) [16].

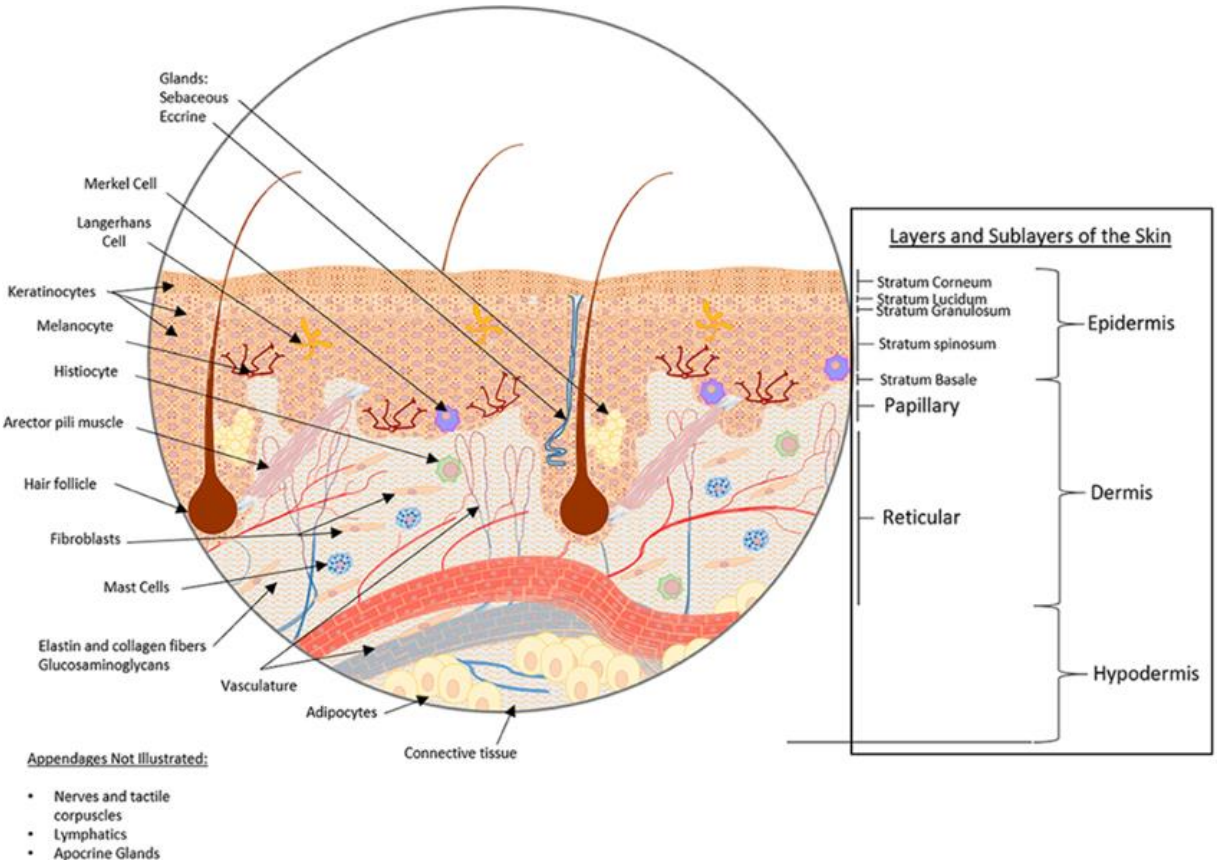

Figure 3 – Healthy skin structure: layers, sublayers, and appendages/macrostructures *[16]*.

The hypodermis, also known as the subcutaneous tissue (adipocytes, nerves, and blood vessels), is a fatty tissue representing the deepest part of the skin and functions as an insulator, shock absorber, and nutrient reservoir [16].

The dermis comprises the bulk of the skin, ranging between 0.5 mm and 5 mm, and provides its pliability, elasticity, and tensile strength through extracellular matrix (ECM). It protects the body from mechanical injury, binds water, aids in thermal regulation, and includes receptors of sensory stimuli. The papillary (superficial) dermis forms conic upward projections alternating with epidermal rete ridges, thus increasing the surface of contact between the dermis and epidermis and allowing for better adhesion between these layers. It contains several cells (fibroblasts, dermal dendrocytes, mast cells), vessels, and nerve endings.

It is made of collagen fibres arranged in loose bundles and of thin elastic fibres stretching perpendicularly to the dermal-epidermal junction. The reticular (deep) dermis contains the deep part of cutaneous appendages, and vascular and nerve plexuses, and is made of coarser collagen bundles, tending to lie parallel to the skin surface [15, 17].

The dermal-epidermal junction (DEJ) consists of a basement membrane (BM) which is a complex mixture of ECM proteins and fibres that anchor the epithelium to the underlying tissue. It plays a fundamental role as a mechanical support for the adhesion of the epidermis to the dermis and regulates the exchanges of metabolic products between these two compartments [15, 18, 19, 20].

The ECM is the largest component of normal healthy skin and gives the skin its unique properties of elasticity, tensile strength, and compressibility. It is composed of fibrous-forming structural molecules such as collagens, fibronectin, laminin, and elastin, nonfibrous-forming structural molecules, and matricellular proteins that do have a structure-function but modify cell-matrix interactions. Type IV collagen is the main structural constituent of the BM and has been immunolocalized mainly to the basal lamina (**Figure 4**) [15, 18, 19, 20].

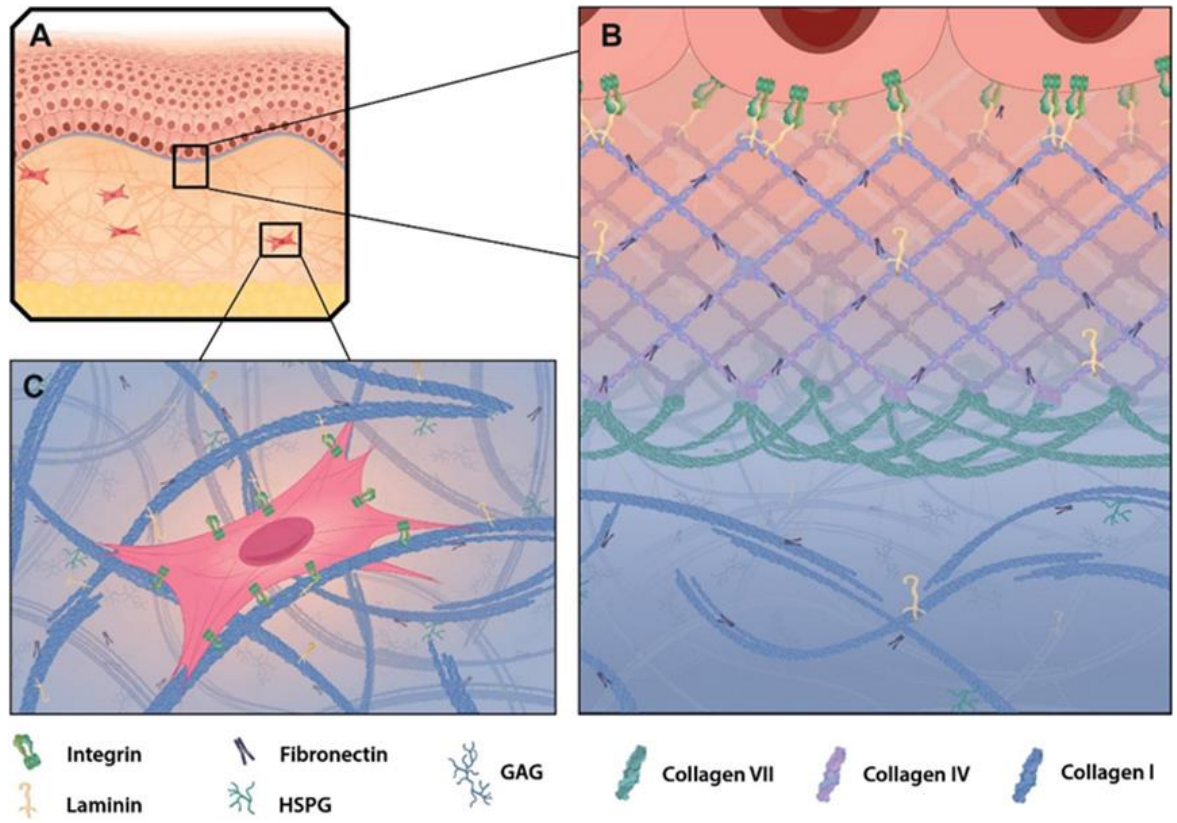

Figure 4 – ECM in healthy human skin *[20]*.

Derived from ectoderm, the epidermis is the superficial protective layer of the skin, with varying thickness between 60 μm and 100 μm over most areas and reaching 600 μm in the plantar and palmar region, composed of stratified squamous epithelium that renews itself continuously. It is made of various cell types, the majority of which (90-95%) are keratinocytes and 5 to 10% of them are non-keratinocytes, including mainly Langerhans cells, melanocytes, and Merkel cells [15, 17].

Commonly, epidermal cells are arranged in continuous layers, comprising: the *stratum basale* (SB) layer or *stratum germinativum* (single layer), the squamous cell layer or *stratum spinosum* (5-15 layers), the granular cell layer or *stratum granulosum* (1-3 layers) and the horny or cornified cell layer or *stratum corneum* (5-10 layers). In some body areas (namely the palmoplantar region) an additional layer, the *stratum lucidum (SL)*, can be seen between the granular and the horny layers [15, 17].

The *stratum spinosum* (SS) is the thickest layer of the epidermis and contains polyhedral cells with rounded nuclei and lamellar granules. Lamellar granules are membrane-bound organelles containing glycoproteins, glycolipids, phospholipids, free sterols, and several acid hydrolases, including lipases, proteases, acid phosphatases, and glycosidases. Desmosomes, which are abundant and support mechanical coupling between epidermal cells and give resistance to physical stressors, bridge the intercellular spaces between spinous cells. Keratin filaments in the cytoplasm are arranged concentrically around the nucleus and are connected to desmosomal plaques at one end while remaining free at the end that is closest to the nucleus. Another type of connection between epidermal cells is termed a gap junction. These junctions, which essentially create an intercellular pore, enable physiologic communication via chemical signals, which is essential in the control of cell metabolism, development, and differentiation. Langerhans cells are another component of the *stratum spinosum*, which acts as a dense network of immune system sentinels [15, 18, 19].

The *stratum granulosum* (SG) is composed of flattened cells holding abundant keratohyalin granules in their cytoplasm. These cells are in charge of the continued synthesis and alteration of keratinization-related proteins. The production of both the interfibrillar matrix that keeps keratin filaments together and the inner lining of the horny cells depends on the deeply basophilic, amorphous, and irregular keratohyalin granules. By providing periodic cutting of keratin filaments, the keratohyalin granule's enzyme action causes the epidermis to produce "soft" keratin. Due to the granular layer's status as a keratogenous layer of the epidermis, lysosomal enzymes that are only found in trace amounts in the *stratum germinativum* and *stratum spinosum* are abundant in the *stratum granulosum*. Cells in this *stratum* degenerate and undergo apoptosis as they migrate toward the upper layers, forming the *stratum corneum* [15, 18, 19].

The *stratum corneum* (SC) is the outermost layer of the skin constituted by large, flat, polyhedral-shaped horny cells that have lost their nuclei during terminal differentiation and are considered to be dead. The *stratum lucidum* is only present in thicker skin and is made of eleidin, a result of keratohyalin transformation [19].

Succinctly, keratinization is the consequence of the differentiation process that takes place as the cells migrate from the basal lamina to the surface of the skin, where the keratinocyte first goes through a synthetic and then a degradative phase. In the synthetic phase, the cell builds up a cytoplasmic supply of keratin, a fibrous intermediate filament arranged in an alpha-helical coil pattern that serves as part of the cell's cytoskeleton. Desmosomes are intercellular attachment plates made up of bundles of these keratin filaments that converge on and terminate at the plasma membrane. During the degradative phase of keratinization, cellular organelles are lost, the contents of the cell are consolidated into a mixture of filaments and amorphous cell envelopes, and the cell ultimately acquires the name horny cell or corneocyte (**Figure 5**). Terminal differentiation refers to the cell-death-inducing maturing process [15, 18, 19].

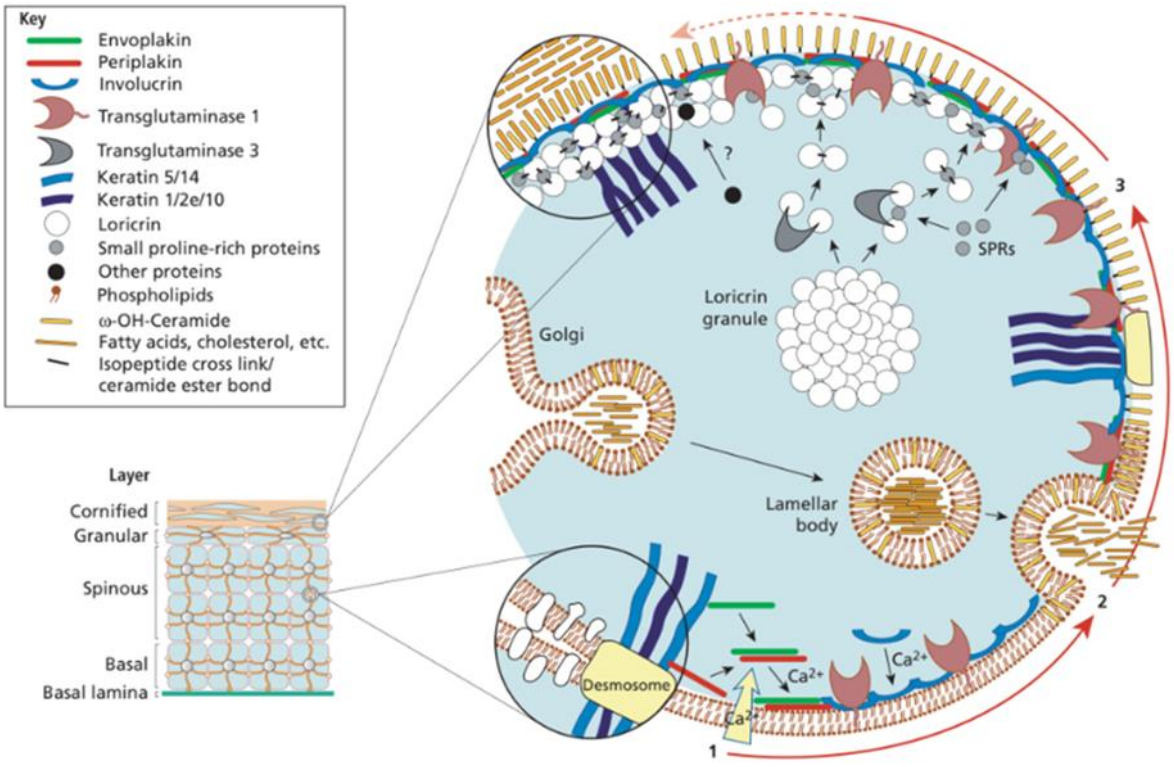

Figure 5 – Assembly of the epidermal cornified cell envelope *[18]*.

The SC, the tight junctions (TJs), the chemical, the immunological, and the microbial barrier are some of the components that work together to form the *in-vivo* skin barrier. A viable epidermis contributes to the

skin barrier by adherens junctions, desmosomes, and tight junctions (TJs). Desmosomes and adherens junctions are crucial for keratinocyte adhesion and differentiation, which are required for epidermal integrity but are not specifically linked to skin barrier function. On the other hand, TJs are cell-cell junctions that are essential for skin barrier function as they are directly involved in the inside-out barrier function. These proteins inhibit the paracellular pathway, preventing chemicals from moving freely through the intercellular space, and are involved in the differentiation, proliferation, cell polarity, and signal transduction processes of cells. They consist of transmembrane proteins of the claudin family, TJ-associated marvel proteins (e.g., occluding), and junctional adhesion molecules, as well as TJ plaque proteins, and are connected with the actin filament cytoskeleton. The chemical barrier is concerned with the skin's protection, inflammatory response, and wound-healing processes, and is mainly composed of antimicrobial peptides. In turn, the Langerhans and dermal dendritic cells, mast cells, basophils, T cells, and components of the humoral immune system including cytokines constitute the immunological barrier in the epidermis. Furthermore, a variety of microorganisms known as the microbiome colonize the native skin. These microorganisms create substances that are bactericidal and stop the growth of pathogenic microorganisms enhancing the host's innate immunity [19, 21].

As previously referenced, the small nature of NMs allows them to penetrate the skin and reach circulation, potentially leading to negative impacts on human health. The first contact of the NPs with the skin occurs in the epidermis layer, and only then do they advance to the dermis layer [15, 17].

In addition to ethical issues regarding the use of animal testing, according to the Humane Society International, 9 out of 10 drug candidates that appear safe and effective in animal studies fail when administered in humans, and in less than 10% of cases, real results cannot be predicted, reaffirming a strong need for cosmetic, pharmacological, and toxicological sciences to replace animal testing with reliable, reproducible, and high-yield alternative methods, developing *in-vitro* skin models capable of simulating common and critical skin diseases [22].

1.7 Microfluidic Organ-On-a-Chip

Microfluidics is a relatively newly emerged field based on the combined principles of physics, chemistry, biology, fluid dynamics, microelectronics, and material science [23]. It is the science and technology of systems that process or manipulate small (10^{-9} to 10^{-18} liters) amounts of fluids, using channels with dimensions of tens to hundreds of micrometers [24].

Such miniaturized microscale devices are useful instruments for carrying out operations like reactions, separations, or the detection of various compounds. Depending on their application and functional particularities, microfluidic devices can also be found in the literature as microreactors, lab-on-a-chip, or OoC. The potential for advances in the field of microfluidics increases abruptly, bringing new perspectives to both the academic and industrial sectors. Besides, this technology is promising for day-to-day applications, as several commercially available devices are already employed in pregnancy at-home-testing; human immunodeficiency virus (HIV), Coronavirus disease 19 (COVID-19), Herpes Simplex, and hepatitis A, B, and C rapid testing, and blood glucose monitoring [23].

OoC are microfluidic devices for culturing living cells in continuously perfused, micrometer-sized chambers to model the physiological functions of tissues and organs. The goal is not to build a whole living organ but rather to synthesize minimal functional units that recapitulate tissue- and organ-level functions. By recapitulating the multicellular architectures, tissue-tissue interfaces, physicochemical microenvironments, and vascular perfusion of the body, these devices produce levels of tissue and organ functionality not possible with conventional 2D or 3D culture systems. They also enable high-resolution, real-time imaging and *in-vitro* analysis of biochemical, genetic, and metabolic activities of living cells in a functional tissue and organ context [25].

Providing their destination use, microfluidic OoC can be manufactured from a broad range of materials, employing diverse fabrication methods. Essential properties that must be considered when choosing the material are durability, ease of fabrication, transparency, biocompatibility, chemical compatibility with the implied reagents, meeting the temperature and pressure conditions needed for the reaction, and the potential of surface functionalization. Typical substrates employed in microfluidic devices include glass, silicon, metals, polymers, and ceramics, but the diversity and quality of materials are continuously increasing. Each material has both advantages and limitations, depending on its destination use (**Table 1**) [23].

Table 1 – Some available materials for the fabrication of microfluidic devices and their features (adapted from *[23, 24, 25, 26, 27, 28, 29]*).

Materials	Advantages	Limitations
Silicon	- Ready availability - Chemical compatibility - Thermostability - Ease of fabrication - Design flexibility - Semiconducting properties - Possibility of surface modifications for cellular attachment and growth	- Opacity of silicon, which renders it incompatible for optical detection in the visible and ultraviolet regions - Incorporating active components is complicated due to the quite fragility of silicon and its high elastic modulus - Relatively expensive material

Glass	- Chemically inert - Thermostability - Electrically insulating - Rigid - Biologically compatible - Allows easy surface functionalization - Excellent optical transparency - Possibility of integrating active components	- Despite being cheap, glass is expensive to be manufactured into chips and requires time-consuming labor
Hydrogels	- Highly porous tridimensional networks of hydrophilic polymer chains that allow the diffusion of small molecules and bioparticles - Resemble the ECM, having intrinsic critical features to mimic natural mechanical and structural cues for cell adhesion, proliferation, and differentiation - Biocompatibility - Low cytotoxicity - Biodegradability - Controllable pore size - High permeability	- Maintaining the device integrity is quite challenging and can limit their use in the long term
Polymers	**a. Polydimethylsiloxane (PDMS)** - Cheap - Easy to mold - Good for prototyping - Optical transparency - Gas permeability - Biocompatibility - Low autofluorescence - Natural hydrophobicity - High elasticity **b. Polymethylmethacrylate (PMMA)** - Optical transparency - Good mechanical properties - Allows surface modification - Good for prototyping at a small scale of production - Amorphous thermoplastic with slightly better solvent compatibility than PDMS and no small-molecule adsorption **c. Polytetrafluoroethylene (PTFE)** - Thermo-processability - Chemical inertness - Compatibility with organic solvents - Excellent antifouling properties - Optical transparency - Moderate permeability to gases	- The porosity of PDMS makes it an adsorptive material, in which many molecules can diffuse. This renders the material incompatible with organic solvents as their molecules can be adsorbed into channel walls and swell the platforms - Water evaporation through channel walls, which leads to a change in the concentration of a solution - PMMA does not allow gas exchanges.

Epoxy resins	- Thermosetting material - Enhanced stability at high temperatures - Chemical resistance - Optical transparency - Very high resolution	- High cost

Fabrication methods must be adapted for the specific characteristics of the involved material and the finite product requirements. Fortunately, nowadays, many fabrication techniques have been described and adopted. One classification of these methods depends on how the microfluidic structure is created: by removing material (removing techniques) or by depositing material (depositing techniques). Another classification divides the fabrication methods depending on the nature of the processes involved – namely, chemical, mechanical, laser-based, and other processes [23, 29].

In order to understand and work with microfluidics, one must first understand the physical phenomena that lead at the microscale. Laminar flow, diffusion, fluidic resistance, surface area-to-volume ratio, and surface tension are the predominant effects [30].

The ratio of inertial to viscous forces in a fluid is expressed by the dimensionless Reynolds number (Re). The Re of a fluid flow can be calculated by **Equation 1** and describes its flow regime – laminar or turbulent.

$$Re = \frac{\rho \, v \, Dh}{\mu} \qquad \textbf{(Equation 1)}$$

where ρ is the fluid density, v is the characteristic velocity of the fluid, μ is the fluid viscosity, and Dh is the hydraulic diameter. The hydraulic diameter is a computed value that depends on the channel's cross-sectional geometry. If Re is inferior to 2300, normally indicates a laminar flow. As Re approaches 2300, the fluid begins to show signs of turbulence, and as Re becomes greater than 2300 the flow is considered to be turbulent. Because of the small size of OoC microchannels, flow is almost always laminar allowing for highly predictable fluid dynamics [30, 31].

Two or more streams flowing in contact with one another will not mix except by diffusion as a result of laminar flow. This can be described by the tendency of a concentrated group of particles to move to regions of lower concentrations due to Brownian motion, by **Equation 2**:

$$d^2 = 2Dt \qquad \textbf{(Equation 2)}$$

where d is the distance a particle moves in a time t, and D is the diffusion coefficient of the particle. Because distance varies with the square power, diffusion becomes more important on the microscale.

Inside the microchannels, the fluid is submitted to resistance. Hydraulic resistance dictates the flow rate within the channel, given by **Equation 3**:

$$Q = \frac{\Delta P}{R} \quad \textbf{(Equation 3)}$$

where Q is the flow rate, ΔP is the pressure drop across the channel, and R is the channel resistance. And by extension, the hydraulic resistance of a rectangular microchannel is given by **Equation 4**:

$$R = \frac{12\mu L}{wh^4} \quad \textbf{(Equation 4)}$$

where μ is the fluid viscosity, L is the channel length, w is the channel width, and h is the channel height. Moreover, compared to gravity, which is far more dominating on a macroscale, surface tension and capillary forces are dominant on a microscale [30, 31].

All the physical properties of the materials and microfluidic technology mentioned above can be taken advantage of and implemented to perform dynamic cell culture on a chip. It is not surprising that, since these appearances, microfluidic devices for OoC purposes have been gaining a lot of attention. This branched field seeks to replicate the function of *in-vivo* organs and pathologies in one device, integrating various components into a single platform, allowing for a closer view of the true scenario. Currently, available OoC examples are the brain, heart, lungs, liver, gut, pancreas, kidneys, skeletal muscle, adipose tissue, skin, cornea, cervix, amnion, placenta, blood vessels, and bone. Numerous of these models feature two perfusable channels that overlap and are separated by polymeric permeable membranes, allowing the growth of two or more cell types in fluidically independent chambers. [32, 33, 34].

One of the most promising OoC applications is the development of multi-organ-on-a-chip (multi-OoC) platforms to replicate the interactions between different organs. Some examples of multi-OoC include the co-culture of a liver and kidney model to investigate changes in metabolism for repeated dose multi-drug toxicity screening, and the co-culture of an intestine model with liver cells to investigate intestinal absorption and liver metabolism of drugs [35, 36]. Other groups are also exploring the connections between up to four organs with the goal of developing a body-on-a-chip [37, 38, 39].

Even though huge advances were already observed in the past decades, there is still a significant lack of using OoCs to understand key biological mechanisms related to NMs exposure and uptake, with most studies remaining in the proof-of-principle stage. OoC examples of skin, lung, and gut are being used to evaluate nanomaterial entrance; the liver and kidney are being utilized to test metabolism and clearance; and bone marrow, blood vessels, and spleen are being applied as toxicity-susceptible organs [34].

1.8 Skin-On-a-Chip Models

Skin-on-a-chip (SoC) are microfluidic devices that simulate skin complexity, making them an ideal tool for evaluating the toxicity of nanomaterials and for building *in-vitro* skin disease models (**Figure 6**) [22].

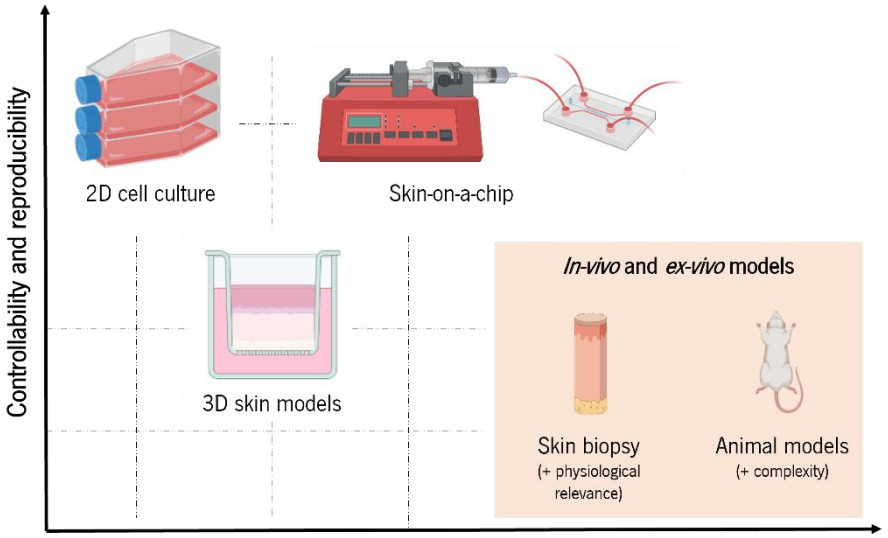

Figure 6 – Comparison of the controllability, reproducibility, physiological relevance, and complexity of the different methods. The figure emphasizes the potential value of OoC technology in providing a reproducible and physiologically relevant approach. Figure generated in BioRender (adapted from *[41]*).

Depending on the research and development phase and the fundamental question of the study (permeability, irritation, corrosion, toxicity, disease models, pharmacology, therapeutic approaches, pharmacokinetics, and formulation optimization), different factors should be considered when preparing optimal SoC platforms (**Figure 7**) [40, 41].

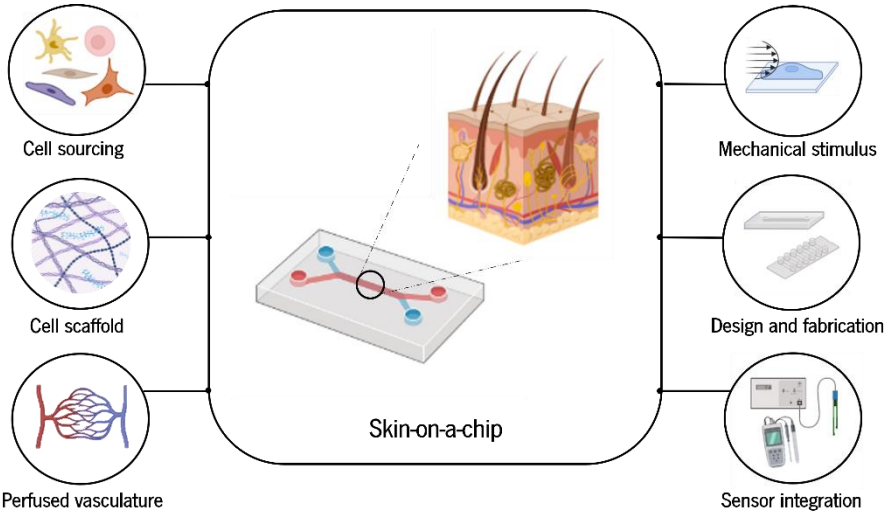

Figure 7 – Schematic drawing representing the main factors to be considered when developing physiologically relevant SoC models, including technical and biological factors. Figure generated in BioRender (adapted from *[41]*).

In the complexity order of the testing platforms, artificial membranes are the simplest elements. These membranes contain pores, have high compatibility with solvents, are chemically inert and commercially available [40].

One of the most determinant factors for developing a SoC device is cell selection and sourcing. When choosing the ideal cell types for integration in the SoC platform, the context of the application must be considered, and the key aspects and components needed for the function must be determined. Over the past decades, multiple *in-house* culture protocols have been developed and improved to incorporate different cell types and biological sources into human skin models [41].

Conventional FT-SoC is constructed using primary human skin cells (epidermal keratinocytes and dermal fibroblasts). These cells were obtained from ordinary surgical procedures performed on healthy human skin. Using primary cells from human donors has the clear advantage of capturing the *in-vivo* phenotype. However, one of the main concerns with using primary skin cells is that they undergo senescence and have a restricted proliferation and amplification capacity [41, 42].

To overcome the limitations of using primary cells, immortalized skin cell lines can be utilized. A cell line can become immortalized through a variety of processes, such as spontaneous immortalization, overexpression of telomerase, and/or telomerase reverse transcriptase (hTERT). The key benefits of immortalized cell lines include their reproducibility and the wide availability of reliable cell expansion protocols. Though, immortalized cell lines can deviate from the original phenotype and are only approximations of the primary cell function. In summary, different keratinocyte cells have been used for the epidermal component of a skin equivalent, including human papillomavirus type 16 (HPV-16) and human papillomavirus type 18 (HPV-18) immortalized keratinocytes, spontaneously transformed aneuploid immortal keratinocyte cell line from adult human skin (HaCaT), near-diploid spontaneous immortalized human keratinocytes (NIKS), hTERT immortalized keratinocytes, cyclin-dependent kinase 4 (CDK4) overexpression, and squamous cell carcinoma (SCC) [41, 42].

A promising alternative source of cells for tissue engineering is induced pluripotent stem cells (iPSC). These cells are derived from adult somatic cells via reprogramming with ectopic expression factors. When these factors are expressed, the genes involved in differentiation are suppressed, reverting the cells to their pluripotent state. Due to its limitless proliferation and capacity to differentiate into multiple cell types, iPSC offers a method to circumvent the constraints imposed by conventional FT-SoC. Additionally, developed cells from iPSC maintain the characteristics of the original donor, such as the phenotype, providing a novel source for simulating skin diseases [42].

Understanding the interactions between different cell types and how the ECM affects cellular function and architecture is also necessary for the correct development of an SoC device. To encourage the development of suitable tissue architecture and physiology, the ECM composition and 3D arrangement must be carefully engineered since they have effects on cell morphology, polarity, and survival. Conventional methods to develop the dermal compartment involve the use of natural hydrogels, typically animal-derived collagen, to create an environment conducive to cell adhesion and growth. However, the ECM tends to contract and degrade as fibroblasts proliferate, limiting their lifespan and application due to the lack of reproducibility. This generally causes the compartment to detach from the membrane, generating leaking problems. The biophysical properties of the skin should be specifically mimicked by alternative polymers or hydrogels. One interesting prospect is developing a fibroblast-derived matrix that stimulates fibroblasts to synthesize the different components of the *in-vivo* ECM. To produce good mechanical stability, this approach might be combined with the use of a scaffold [41].

In turn, the vasculature of the skin is located within the dermis and provides essential functions, supplying nutrients to the cells and removing undesirable metabolic waste. Additionally, it acts as a conduit for immune system components and contributes to thermoregulation. The cutaneous vasculature is also involved in the growth of tumors, metastasis of malignant melanoma, acute and chronic inflammatory conditions, wound healing, and other pathological diseases. Furthermore, it has been demonstrated that vasculature influences the transdermal penetration of substances, and how the body reacts to irritants. Therefore, to simulate physiological *in-vitro* skin conditions and pathological situations, cutaneous vasculature creation is crucial [41].

Culture mediums have been vascularized using a variety of techniques that can be categorized into the pump- or gravity-driven approaches. External pumps, such as a syringe pump or peristaltic pump, are the most popular ways to generate fluid flow. These systems deliver accurate, fine-tuned fluid flow but are typically time-consuming. Furthermore, tubing and connections can increase the risk of contamination [41].

In order to develop microfluidic devices for mimicking human skin, mainly two different approaches have been developed: the first one is the direct introduction of a skin fragment coming from a biopsy or artificially vascularized human skin equivalents (HSEs) in the chip – transferred SoC – and the second one is focused on the *in-situ* generation of the tissue directly on the chip – *in-situ* SoC. HSEs are bio-engineered skin tissues prepared using collagen ECM, human dermal fibroblasts (HDFs,) and human epidermal keratinocytes (HEKn) [43, 44].

Due to the presence of different skin layers which allows more realistic models, the ones containing a dermal compartment are more frequently used for transferred skin chips. Despite the use of these well-formed and mature tissue fragments, epidermal and dermo-epidermal models can also be found in the literature. The transferred SoC models have permitted the study of different factors affecting the maintenance of the equivalents and their use for clinical and testing purposes (molecules diffusion, multiorgan crosstalk, drug sensitivity, and toxicity) [43].

In-situ SoC focuses on the generation of the skin model directly on the chip. Two different groups can be also distinguished among the *in-situ* skin devices. The first system, which is built on an artificially vascularized dermis, is comparable to the transferred SoC: inside the device, tissue is manually generated in an open space. The primary distinction lies in the method by which culture medium or any other substances are supplied to the skin construct: while the transferred SoC are perfused through hollow channels passing across the dermal compartment, in these SoC devices, the circulation of the fluids is carried out through a microfluidic channel below the tissue construct The second *in-situ* approach and the ideal aim for SoC are the modeling of the organ directly inside the device, using the channels not only as a way of delivering nutrients but also as compartments for holding the tissue [43].

OoC technology can be used to constantly deliver cell culture medium and remove cell metabolites while also introducing mechanical stimulus that is similar to what organs and tissues experience *in-vivo*. A well-known phenomenon is cellular mechanotransduction, and numerous studies have described the cellular mechanisms by which mechanical stresses are transduced into biochemical signals. These responses play a crucial role in the cellular microenvironment, which controls a variety of processes in both healthy and unhealthy states. Relevant *in-vivo*-like biomechanical forces include shear stress and tensile and compressive forces. Shear stress is the term for the forces generated when an object is subject to a tangential force. This force can be imparted by fluid flowing over an object and is prevalent throughout the human body. Endothelial cells, which are sensitive to changes in fluid flow, are more affected by this effect [41].

Epidermal keratinocytes are sensitive to shear stress caused by microflow, as demonstrated by Agarwall et al. During the influence of shear stresses of magnitude 0.06 dyne/cm^2, these cells demonstrated mechanoresponsive structural reorganization and cellular damage under shear stresses of magnitude 6 dyne/cm^2. The team also demonstrated that shear stress enhanced the size of the cell colony and the expression of Zonula occludens-1 and E-cadherin at the cell-cell interface. These results suggest an improvement in the epithelial phenotype. Because cultivation at the air-liquid interface (ALI) is necessary

for skin differentiation, keratinocytes are not exposed to fluid flow-induced shear stress at the apical side except for the first 24 to 48 hours, and at the basal side, keratinocytes are typically protected from the effect of shear by a membrane or dermal compartment. The magnitude of the applied shear stress corresponding to the applied flow rate in the microfluidic devices under the laminar regime is calculated by **Equation 5**:

$$T = \frac{6\mu Q}{h^2 w} \qquad \textbf{(Equation 5)}$$

where T correspond to the shear stress, μ is the dynamic viscosity of the fluid (for medium, μ = 0.007 dynes/cm^2), Q is the applied flow rate, h is the height of the microchannel and w is the width of the microchannel [45].

In addition to the shear stress induced by perfusion, tissues in the body are continuously subjected to other forces, as well as tensile and compressive forces. Cyclic stretch is one of many mechanical stimuli that the human skin is subjected to. Tissue is stretched as a result of the tensile pressures applied to the cellular microenvironment. This is a result of environmental effects, growth, and various internal processes. In epidermal keratinocytes, stretch stimulation promoted cellular adhesiveness, proliferation, and protein synthesis. When exposed to these forces, dermal fibroblasts increase secretion of epidermal growth factor, promoting an asymmetric keratinocyte migration, and resulting in an accelerated wound repair [46].

Conventional analyses of tissue function mainly depend on endpoint assessment techniques. Due to the restricted light penetration and scattering effects, traditional microscopy techniques cannot be used for 3D cell culture employing scaffolds or membranes. By integrating microsensors for detecting relevant physical/chemical parameters *in-situ*, OoC devices can overcome this restriction.

The first attempts to integrate sensors into OoC systems have demonstrated the importance of real-time monitoring to capture changes in the characteristics of living cells in order to gather comprehensive information about what is happening inside the OoC. In the context of SoC platforms, the integration of sensors would be extremely relevant. An ideal future SoC platform should have electrochemical sensors for evaluating soluble protein biomarkers, physical sensors for monitoring important cell culture factors (such as pH, O2, and temperature), and transepithelial electrical resistance (TEER) sensors for assessing skin barrier function. By monitoring changes in the transcellular and paracellular permeability of epithelial/epidermal *in-vitro* cell cultures, this technique assesses the integrity of stratifying cultures. TEER values are calculated by **Equation 6**:

$$TEER = (R_{sample} - R_{blank})\, A \qquad \text{(Equation 6)}$$

where R_{sample} is the resistance value for the skin model, R_{blank} is the resistance value of an insert without cultured cells, and A the effective cultured area.

However, the literature has reported a wide range of TEER values for the same cell/tissue type. This great variability is thought to be caused by a combination of biological elements (such as the number of cell passages) and TEER-related mechanoelectronics. Air bubbles in microchannels and incomplete cell coverage are two additional potential sources of errors for TEER measurement taken on a chip. According to reports, a 0.4% gap in tissue coverage might cause the measured TEER values to fall by about 80% [41, 47, 48].

OoC devices for skin cultivation are still in their early stages. Ataç et al. published the first study in the field in 2013 [49]. Since then, a number of SoC platforms utilizing a variety of methodologies have been published [50, 51, 52, 53, 54, 55, 56, 57, 58, 59].

1.9 Epidermis-On-a-Chip Models Reported on the Literature

The available epidermis-on-a-chip (EoC) reported so far in the literature are summarized in this subchapter (**Table 2**). EoC are microfluidic devices that simulate the epidermis layer (keratinocytes layer) of the skin.

It is important to refer that none of the developed EoC models were established for the safety assessment of NMs.

Sasaki et al. developed a photolithography-free device to culture an HaCaT monolayer and perform permeation assays (**Figure 8**). In this work, the group created a basic platform without the use of complex microfabrication methods, which might pose a challenge to some researchers. With the use of a PDMS mortar, a porous membrane was sandwiched between branched microchannels. By adding fluorescein isothiocyanate-dextran (FITC-Dextran) solution to the top channel, the researchers analyzed how potassium dichromate affected the permeability of the cell monolayer [60, 61, 62].

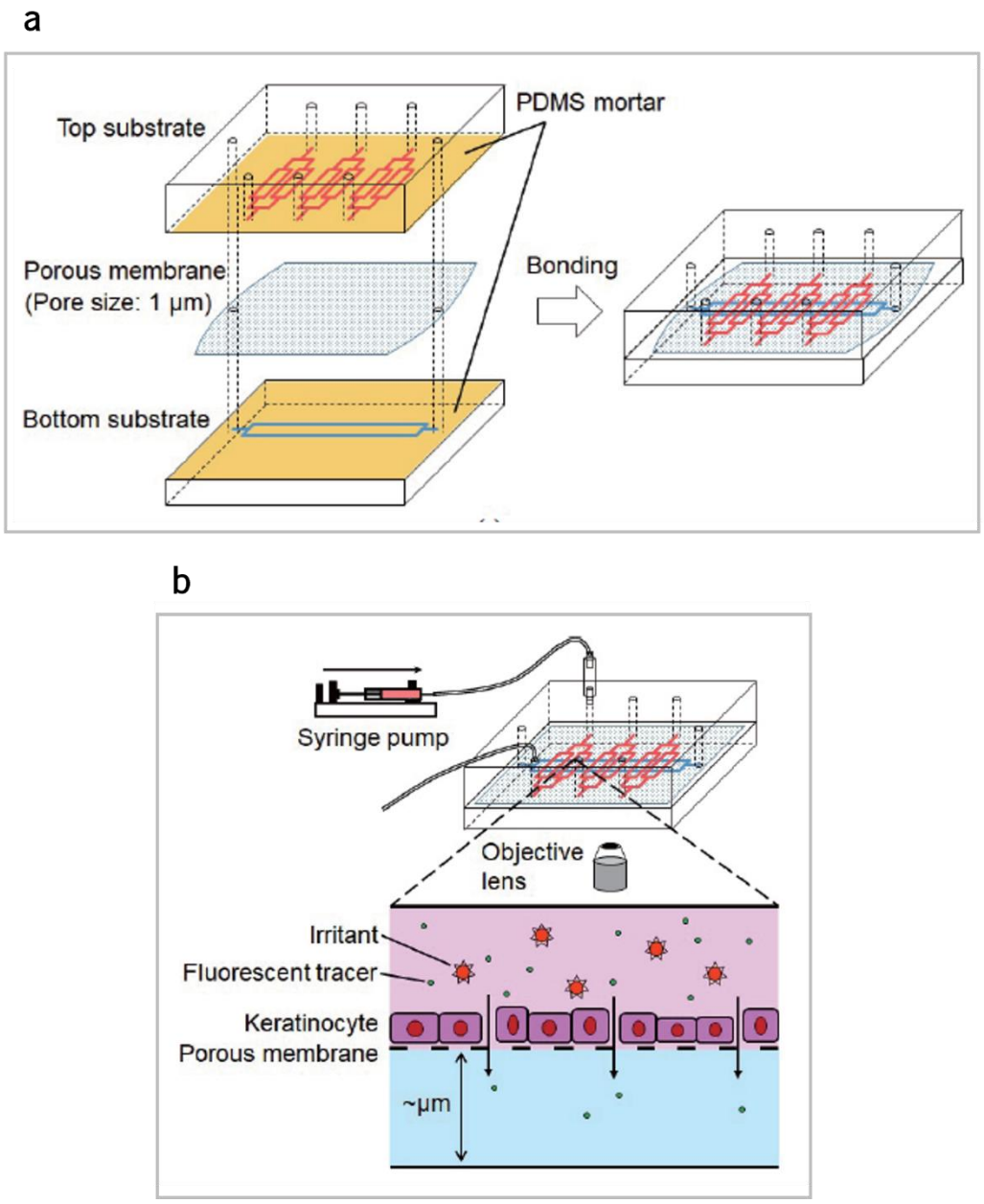

Figure 8 – Sasaki et al. EoC: (a) Schematic illustration of the fabrication of the microfluidic device; (b) Concept of the EoC technology (adapted from *[60]*).

Zhang et al. established an integrated epidermis-on-a-chip (iEoC) system which is designed to integrate bubble removal structures as well as TEER electrodes for barrier function detection *in-situ* (**Figure 9**). After 14 days of culture at the ALI, the group did histological and immunofluorescence analyses to observe the morphology and the keratin expression in the formed tissue, including keratin-10 (K10), keratin-14 (K14), loricrin, involucrin, and filaggrin, respectively. Additionally, the iEoC allowed distinguishing all the 10 known toxins and non-toxins in skin irritation measurement by (3-(4,5-dimethylthiazol-2-yl)-2,5-

diphenyltetrazolium bromide) tetrazolium reduction assay (MTT assay), that were consistent with animal testing according to the Organization for Economic Co-operation and Development (OECD) [63].

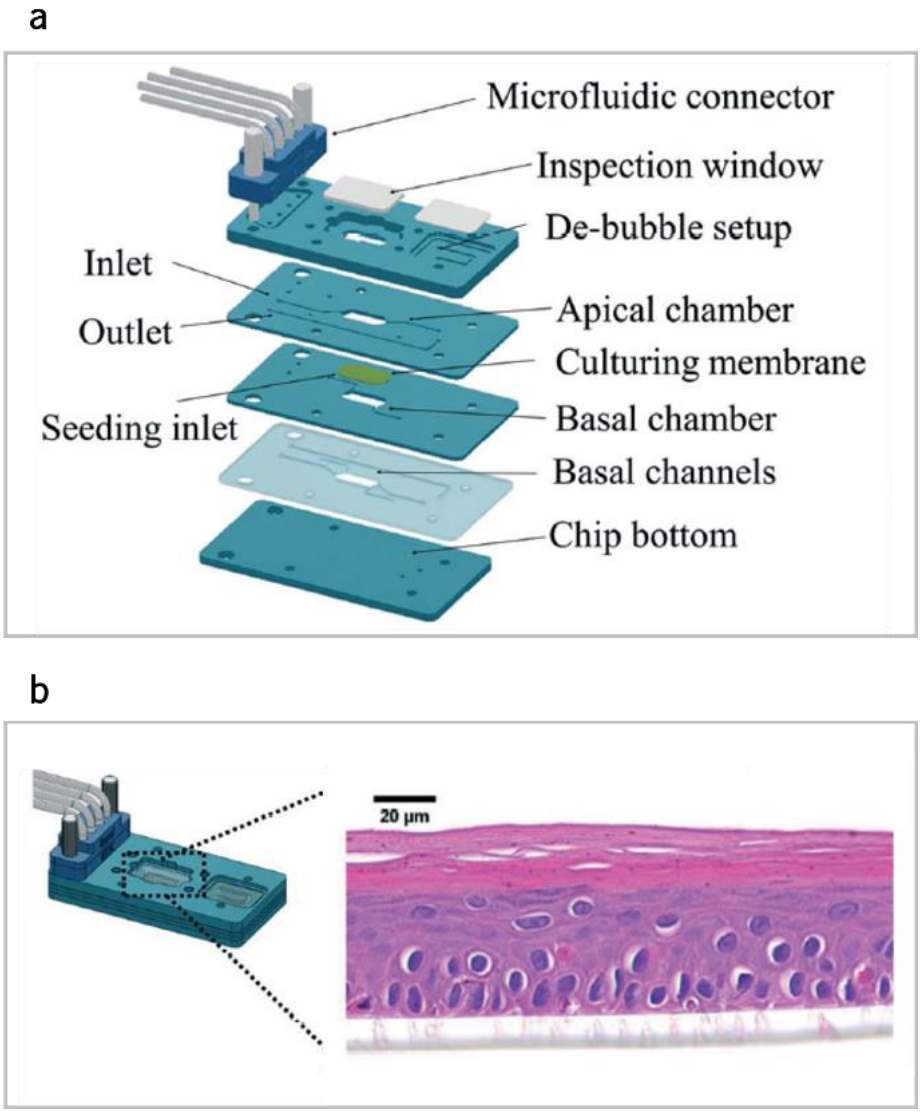

Figure 9 – Zhang et al. iEoC: (a) Schematic illustration of the fabrication of the microfluidic device; (b) H&E staining of the 3D epidermis equivalent constructed through the iEoC. Scale bar: 20 μm (adapted from *[63]*).

Table 2 – Main characteristics of the EoC reported in the literature.

Fabrication methods; Device materials	ECM coating	Cell type; Seeding density	Culture medium	Flow type; Velocity; Duration on-chip	Main features	References
- Soft lithography. - PDMS, and glass slide. - PET (0.4 µm and 1 µm pore size), and PCTE (0.1 µm pore size) membranes.	None	- HaCaT. - $3.6x10^6$ cells/mL.	DMEM supplemented with 10% FBS and 1% antibiotic antimycotic	- Syringe pumping. - 10 µL/min. - 15 days.	- Cell viability analysis (Live/Dead® assay). - Paracellular permeability analysis (FITC-Dextran). - Irritation testing (Potassium dichromate).	Sasaki et al.
- CNC micromilling. - PMMA. - PET (1 µm pore size).	Collagen IV	- NHKs. - $1x10^5$cells/mL.	DMEM and Ham's F12 (3:1) supplemented with 10% BPE, 10 ng/mL EGF, 0.4 µg/mL hydrocortisone, $1.8x10^{-4}$ M adenine, 5 µg/mL insulin, $2x10^{-9}$ M triiodothyronine, 5 µg/mL transferrin, and 1% pen-strep. The medium used in ALI is additionally supplemented with 1.2 mM calcium.	- Peristaltic pumping. - 1 µL/min. - 14 days.	- Quantitative analysis of mRNA expression (RT-PCR) - Histological and immunofluorescence analysis. - Confocal spectroscopy. - TEER measurements. - Paracellular permeability analysis (Cascade Blue™ and Texas Red dye). - Cytokine – IL-6 and TNF-α – detection (ELISA).	Zhang et al.

CHAPTER 2

MATERIALS AND METHODS

2.1 Nanoparticles

TiO_2 NPs, more specifically rutile NPs with a purity of 99.5%, were obtained from Skyspring Nanomaterials, Inc. (Ref. 7920DL). This material is a fine white powder composed of titanium oxide particles with a D50 ranging from 10 nm to 30 nm. It signifies the points in the size distribution, up to and including which, 50% of the total volume of material in the sample is contained.

2.1.1 Characterization of Rutile-TiO_2 Nanoparticles

This subtopic focuses mainly on a conceptual description of the basic principles of the techniques used for the characterization of TiO_2 NPs. The characterization techniques used were X-ray diffraction (XRD), Raman spectroscopy, and X-ray photoelectron spectroscopy (XPS).

XRD is a powerful nondestructive technique for characterizing the crystallographic structure of a material. It provides details information on structures, phases, optimum orientations for crystals (texture), and other characteristics like average grain size, crystallinity, strain, and crystal defects. X-ray diffraction peaks are generated by constructive interference of a monochromatic beam of X-rays scattered at specific angles from each set of lattice planes in a sample. The peak intensities are determined by the distribution of atoms within the lattice. Consequently, the XRD pattern is the fingerprint of periodic atomic arrangements in a given material [64, 65].

The patterns were recorded by the X'Pert Pro Panalytical diffractometer system with Cu K-α radiation (1.54184 Å, 45 kV, 20 mA). The system consists of one main console which inside includes the goniometer, the Cu X-ray tube, and all the accessories for different configurations for the incident and diffracted beams, such as monochromator, mirror, parallel plat collimator, triple-crystal/rocking curve prefix and crossed slits.

Raman spectroscopy is a non-destructive technique for chemical analysis that provides thorough details on crystallinity, chemical structure, phase and polymorphy, and molecular interactions. It is based on an intimate interplay between atomic positions in molecules, electron distribution, and intermolecular forces [66].

Since the observed wavenumbers scale with key molecular parameters like force constants or bond distances, Raman spectroscopy can reveal significant chemical properties like binding motives weak interactions (hydrogen bonding), lone-pair character, and others. As a result, Raman spectroscopy is one

of the most effective tools for obtaining information about the structure, and properties of molecules from their vibrational transitions. The effect was first discovered by Chandrasekhara Venkata Raman in 1928 [67].

Structural characterization of the TiO_2 NPs sample was performed by a WITec's Raman spectrophotometer supported by a sample holder for the backscattering geometry. A 50x objective was used, and radiation (532 nm) of an ion argon laser served as the excitation wavelength. A power of 0.5 mW and a grating of 600 gmm^{-1} was chosen for measurements.

XPS, also known as electron spectroscopy for chemical analysis, is the standard tool for surface material characterization because it can be used on a wide variety of materials and gives useful quantitative and chemical state information from the surface of the material being studied [68].

When a solid surface is exposed to an X-ray beam, the energies of the photoelectrons escaping the sample are calculated using a concentric hemispherical analyzer, and XPS spectra are obtained by measuring the kinetic energy (KE) of the electrons that are emitted from the top 1 to 10 nm of the sample, resulting in a series of photoelectron peaks. The photoelectron peaks' energies and intensities allow for the identification and measurement of all surface elements, except for hydrogen and helium. The binding energy (BE) of the peaks is characteristic of each element, and the composition of the surface of the material can be determined using the peak areas. The chemical state of the emitting atom can slightly change the form of each peak and of the BE. Consequently, XPS can provide chemical bonding information as well. The XPS technique is highly surface sensitive because only those electrons generated near the surface escape and are detected, hence ultrahigh vacuum conditions are required [68].

The ThermoScientific™ ESCALAB™ 250Xi was the tool used for the TiO_2 NPs sample surface analysis. The X-ray source used was monochromated Al Kα ($h\nu$ = 1486.68 eV) radiation, operated at 220 W, 14.6 kV, with a spot size of 650 µm. The XPS spectra were collected at pass energies of 100 eV and 40 eV for survey spectra and individual elements respectively. The energy step for individual elements was 0.1 eV.

The XPS spectra were peak fitted using Avantage data processing software. For peak fitting, the Shirley-type background subtraction was used. Quantification has been done using sensitivity factors provided by the Avantage library. The sample cleaning was performed with an Argon cluster ion gun operated at 4 keV cluster KE and cluster size 1000 atoms and was mounted on the sample holder 20 mm x 50 mm using double-sided adhesive carbon tape.

2.1.2 Dispersion of Rutile-TiO_2 Nanoparticles

This subtopic includes standard operating procedures (SOP) for the preparation of suspensions of the rutile-TiO_2 NPs as well as their characterization in terms of size (as measurand hydrodynamic diameter).

The aim of this dispersion is the complete deagglomeration of the particles. Thereby it becomes possible to have the same initial conditions for particle size measurement. For this, suspensions of powdered nanomaterials are produced by direct ultrasonic dispersion. To realize equal dispersion, ultrasonication is performed at an identical specific energy. This in turn requires calorimetric measurements to determine the delivered acoustic energy.

A pre-requisite for a meaningful test to determine the particle size of suspended particles is sample preparation. The problem with the dispersion of powdered materials is that each has different equipment to disperse. Thus, it is not possible just to specify a time, volume, and concentration for the dispersion. Decisive for the dispersion is the specific energy, also called energy density that is applied to the suspension. The specific energy E_{spec} (KJ /m^3) is a function of the delivered acoustic power P (W), the time t (s), and the sample volume V (m^3) and therefore independent of the used ultrasonic device. It is calculated using **Equation 7**:

$$E_{spec} = \frac{P\,t}{V} \qquad \textbf{(Equation 7)}$$

The acoustic delivered energy is the energy consumed for breaking the agglomerates, but also for thermal losses and chemical reactions. This energy can be obtained calorimetrically.

The necessary calorimetric measurement of the delivered acoustic power is relatively simple and fast. Using the calorimetric method, the temperature increased as a result of ultrasonication. The increase of the temperature in the liquid is recorded over time to calculate the delivered acoustic power P (W) by **Equation 8**:

$$P = \frac{\Delta T}{\Delta t}\, m\, c_p \qquad \textbf{(Equation 8)}$$

where T and t are temperature and time, m is the mass of the liquid, and c_p is the specific heat of the liquid at constant pressure. Due to the use of aqueous suspensions, the recording of the calorimetric curves is carried out with water as liquid. Therefore, the specific heat of water with 4.18 J g^{-1} K^{-1} was used.

Beakers were used with 300 mL of tri-distilled water (Milli-Q) and their mass was determined directly by weighing. Then, the water-filled beaker was placed under the sonicator, and the probe was immersed at

2.5 cm below the liquid surface. Different power levels of sonication (30, 50, and 70 %) were chosen and temperature records were done every 30 s for 5 min in continuous mode. The relative temperature increase in Kelvin for each measuring point was calculated and a T vs t diagram was created to determine the linear fit for the curve using the least square regression line. Finally, the delivered acoustic power was calculated according to Equation 8.

After the determination of the acoustic energy, it is feasible to perform the dispersion of the TiO_2 NPs on the basis of the specific energy. Studies on dispersion have shown that above a certain energy no more deagglomeration of the powder is possible. At this point, the smallest achievable dimension or smallest dispersible unit of the given powder is reached.

The strategy employed in this dissertation for rutile-TiO2 NPs dispersions in the biological medium had two basic procedures: (1) powder dispersion by sonication in Milli-Q, (2) dilution of stock suspension in cell culture medium using a stabilizing agent such as bovine serum albumin (BSA). The cumulative method in which the mean particle size and the polydispersity index (PDI) are calculated. Mean particle size and PDI were investigated by dynamic light scattering (DLS) using a ZetaSizer Nano ZS-100 (HORIBA Scientific). DLS measurements were executed at 25 °C using standard 10 mm disposable optical polystyrene cuvettes. Each run of DLS measurements was automatically determined by the instrument's software (Figure 10).

For the dispersion of nanoparticles, TiO_2 was diluted in Milli-Q water to obtain different concentration suspensions. Using Branson Ultrasonic Disintegrator Mod. 450, the tip (Ti 13 mm) was immersed 2 cm in the suspensions, dispersing the NPs by ultrasound at 25 °C for different times in pulsed mode (8 seconds on / 2 seconds off) and different specific energies ($1.15x10^4$ KJ/m^3, $1.89x10^4$ KJ/m^3, and $2.91x10^4$ KJ/m^3).

After achieving the best dispersion conditions in distilled water (30 % amplitude, 30 minutes of pulsed mode), tests with a culture medium were performed as follows. The dispersed rutile stock solution stabilized for 24 hours was diluted to a concentration of 1 mg/mL in the specific culture medium (Dulbecco's Modified Eagle Medium – DMEM – High glucose supplemented with 10 % of fetal bovine serum – FBS). As a stabilizing agent, BSA was used at a final concentration of 0.6 mg/mL and was added to the suspension before incubation in the culture medium. The size distribution was also determined by DLS.

Figure 10 – Schematic illustration of the stages of the rutile-TiO_2 NPs dispersion by probe sonication and their size measurements by DLS. Figure generated in BioRender.

2.2 Microfluidic Device

2.2.1 Design and Fabrication

The microfluidic device for simulating the epidermis was designed using CorelDRAW® Graphic Suites X8 software and AutoCAD 2022 (computer-aided design software) and was fabricated using a laser cutter and engraving (LCE) machine (**Figure 11**).

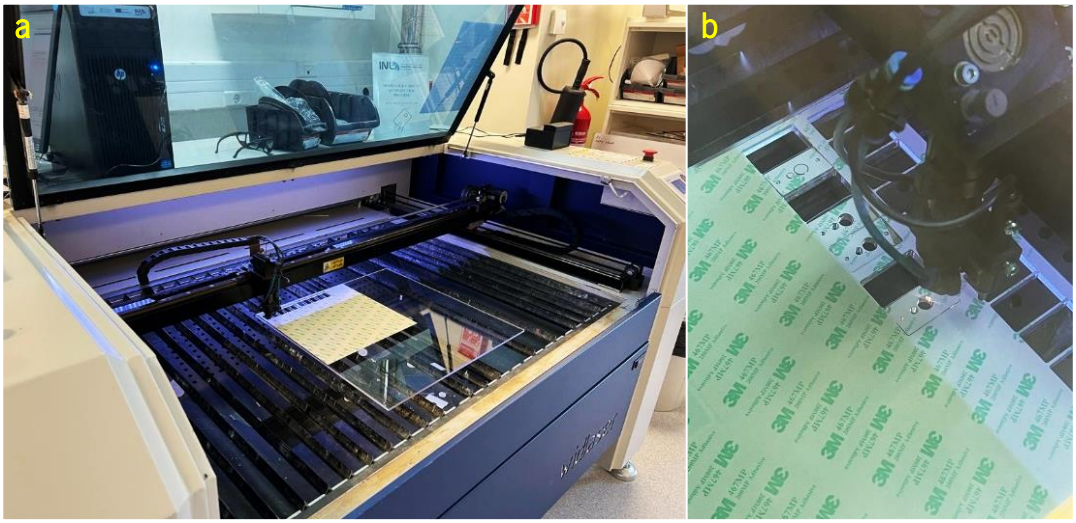

Figure 11 – Devices fabrication. (a) Laser cutter and engraving machine; (b) laser cut in 6 mm thick PMMA layer.

The LCE performance provides cutting on all surfaces and its capability is managed on a Windows XP operating system that includes a control board and control panel and supporting software.

The material used for the construction of the devices was PMMA layers with different thicknesses (0.5 mm, 1 mm, and 6 mm) obtained from Comercial Hospitalaria Grupo-3, and the parameters used on the laser cutter to cut PMMA sheets are shown in **Table 3**.

Table 3 – Laser cutter PMMA parameters.

PMMA thickness	Speed	Power
0.5 mm	40	25
1 mm	30	30
6 mm	10	80

In turn, polyethylene terephthalate (PET) membranes with 0.4 µm and 1 µm pore size were achieved from It4Ip, and 3M™ Adhesive Transfer Tapes tape was used to do de assembling of the PMMA layers.

2.2.2 Computational Study of the Microfluidic Device

A finite element modeling (FEM) study was done to understand the fluid flow effects on the EoC by COMSOL Multiphysics™ software.

In its simplest form, FEM is the dominant discretization technique in structural mechanics. The subdivision of the mathematical model into separate, non-overlapping, finite elements is the basic concept behind the physical interpretation of the FEM whose behavior can be described by relatively straightforward equations [69]

2.3 Keratinocytes Cell Culture

In-vitro spontaneously transformed keratinocytes from histologically normal skin HaCaT cell line was obtained from CLS Cell Lines Service (Ref. 300493). **Table 4** describes the origin and general characteristics. The cell line was cultured in DMEM High-glucose (ThermoFisher), supplemented with 10 % FBS (ThermoFisher) and 1 % penicillin/streptomycin (pen/strep, Sigma-Aldrich). FBS promotes rapid cell growth, and pen/strep antibiotic mixtures are added to cell culture media to eliminate a broad spectrum of bacteria. It significantly reduces both gram-positive and gram-negative bacteria contamination.

Table 4 – Origin and general characteristics of the HaCaT cell line.

Depositor	DKFZ, Heidelberg
Organism	Homo sapiens
Ethnicity	Caucasian
Age	62 years old

Gender	Male
Tissue	Skin
Cell type	Keratinocyte
Growth properties	Monolayer, adherent

HaCaT cells commercially obtained were thawed and routinely subcultured when reached a confluence of 80-90 %. The old cell medium was removed, and the cell monolayer was rinsed with Hank's Balanced Salt Solution (HBSS, ThermoFisher) to remove residues and dead cells. Afterward, the monolayer was submitted to Tryple™ Express Enzyme (ThermoFisher) and incubated for 12 min to dislodge and disperse cells from the T-flasks. Posteriorly, a complete growth maintenance medium was added, and the cell suspension was aspirated carefully into a 15 mL falcon tube and gently resuspended to avoid clumping promote cell separation and non-less importantly inhibit the Tryple™ action. To know cell concentration **Equation 9** and **Equation 10** were used. A sample volume of 10 µL was collected from the resuspended suspension and added to 10 µL of Trypan Blue 0.4 % solution (Sigma-Aldrich), obtaining a dilution with a suitable concentration for cell counting. Trypan Blue is one of several stains recommended for use in dye exclusion procedures for viable cell counting. This method is based on the principle that live (viable) cells do not take up certain dyes, whereas dead (non-viable) cells do. After 10 µL of the previously prepared dilution were carefully introduced into a Neubauer chamber (Hirschmann® EM Techcolor). Lastly, the Neubauer chamber was taken to the microscope, and cells were counted.

$$Cell\ concentration = overage\ cells\ counted\ x\ dilution\ factor\ (2)\ x\ volume\ of\ the\ chamber\ (10^4) \quad \textbf{(Equation 9)}$$

$$Nº\ of\ cells = cell\ concentration\ x\ volume\ of\ cell\ suspension \quad \textbf{(Equação 10)}$$

The remaining cell suspension was centrifuged, and the obtained cell pellet was resuspended in a fresh culture medium. Lastly, appropriate volumes of the cell suspension were added to new culture T-75 with fresh medium and incubated at 37 °C in a 5 % CO_2-humified incubator. The medium renewal was performed 2 to 3 times per week to maintain great cell growth conditions.

2.3.1 Morphology of Keratinocytes through Phase-contrast Microscopy

Living cells that are not stained hardly ever absorb light. Extremely small differences in the intensity distribution of the image are the result of poor light absorption. As a result, under a brightfield microscope, the cells are barely, or not at all, visible. Phase-contrast microscopy is an optical microscopy technique

that converts phase shifts in the light passing through a transparent specimen to brightness changes in the image. It was first described in 1934 by Dutch physicist Frits Zernike. When light passes through cells, small phase shifts occur, which are invisible to the human eye. These phase shifts are transformed into amplitude changes in a phase-contrast microscope, which can be seen as differences in image contrast. The phase-contrast microscope produces an image of high contrast and resolution. The image has a three-dimensional appearance wherein a rounded object appears dark on one side, and bright on the other with grey in between against a grey background [70].

2.3.2 Reconstructed Human Epidermis

Firstly, a solution for collagen IV coating was prepared. A frozen collagen IV solution (0.5 mg/mL) was thawed at room temperature (RT) and prepared at 0.03 mg/mL in DMEM without serum. For 1 mL of coating solution: 940 µL of serum-free DMEM + 60 µL of collagen IV solution were added. The medium showed a yellow color due to the change in the pH of the solution (**Figure 12**). The volume was made of the solution according to the number of EoC devices and Transwell® inserts and 60 µL and 40 µL of the solution were added to each, respectively. The devices and plates were gently tapped a few times to distribute the solution. Afterward, they were kept in the incubator at 37 °C and 5 % CO_2 for 1 to 2 hours, and the rest of the 0.03 mg/mL collagen IV solution left over was discarded.

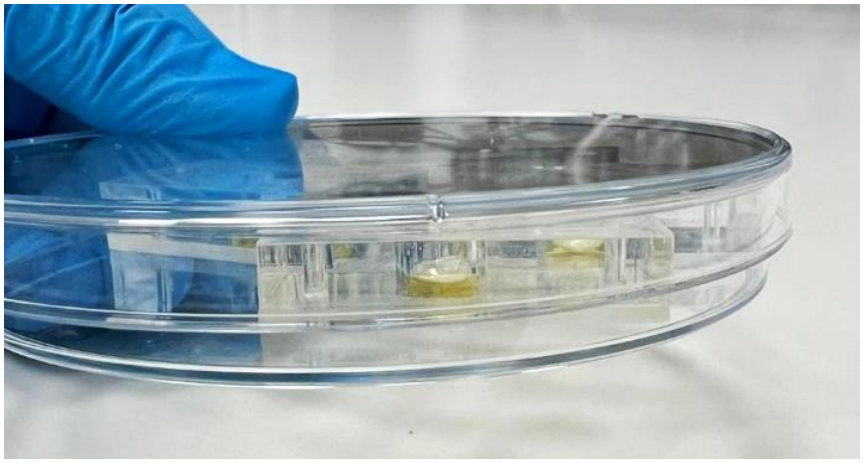

Figure 12 – Collagen IV coating on EoC microfluidic devices.

After 1 to 2 hours in the incubator, the inserts were washed with 200 to 500 µL of complete culture medium. The medium was added to all EoC and Transwell® inserts and was removed taking care not to touch the insert membrane. Cultured keratinocytes were trypsinized, the cells were counted, and the amount needed for the desired experiment was separated. The amount of 75 000 and 150 000 cells per

insert of 24 well plates, and 250 000 cells per EoC was considered. The total amount of cells were placed in falcon tubes and resuspended in the keratinocyte culture medium in the volume for the total number of inserts, considering that 100 µL of cell suspension was placed in each insert and 200 µL of the suspension in the case of the EoC devices (**Figure 13**). The culture medium was also added to the bottom of the inserts (500 µL) and to the EoC microchannels (200 µL). After cell seeding, they were kept in an incubator at 37 °C and 5 % CO_2 for 48 hours.

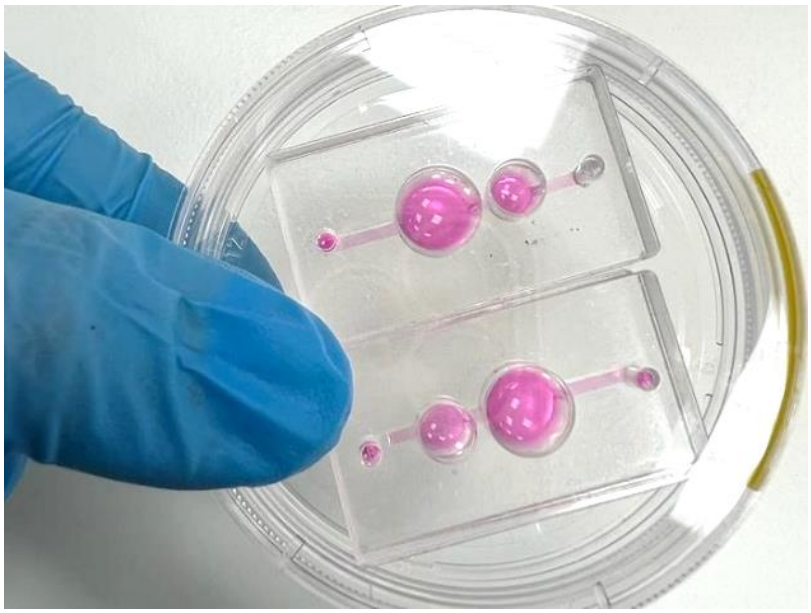

Figure 13 – Cell seeding on EoC microfluidic devices.

Finally, 2 days later the cells were exposed to ALI. The culture medium was removed avoiding touching the PET membranes. For Transwell® inserts, the medium was also removed from the lower compartment of the plates, and 500 µL of differentiation medium was added and changed every 2 days. In turn, for EoC microfluidic devices, the perfusion was started at this stage and maintained constantly for a keratinocyte differentiation period of 14 days. The perfusion system is composed of a syringe pump (NORLEQ), syringes (Terumo), cannulas (Fisnar®), tubing (Cole-Parmer®), and bubble traps (Darwin microfluidics).

Differentiation medium consists of DMEM:HAM-F12 medium (3:1), supplemented with 2 ng/mL cholera toxin (Sigma-Aldrich), 5 µg/mL apo-Transferrin (Sigma-Aldrich), 0.4 µg/mL hydrocortisone (Sigma-Aldrich), 1 ng/mL epidermal growth factor (EGF, Sigma-Aldrich), 2 ng/mL transforming growth factor beta (TGF-β, Invitrogen), 5 µg/mL insulin (Sigma-Aldrich), and 5% of fibroblast-cultured medium.

2.4 Characterization of Epidermis Viability

2.4.1 LIVE/DEAD® Assay

The LIVE/DEAD® Viability/Cytotoxicity Kit was acquired by ThermoFisher Scientific. It is a quick and easy two-color assay to determine the viability of cells in a population based on plasma membrane integrity and esterase activity. This assay quickly discriminates live from dead cells by simultaneously staining with green fluorescent calcein-AM to indicate intracellular esterase activity and red-fluorescent ethidium homodimer-1 to indicate loss of plasma membrane integrity.

The vials were thawed, and the Live Green vial was transferred to the Dead Red vial and mixed to create a 2X stock solution. The cells were washed with warm HBSS and an equal volume of the 2X stock solution was added to the cells. After an incubation at 37 °C and 5 % CO_2 for a period of 10 to 40 minutes, fluorescence microscopic observation was carried out and photographs were taken. The images were treated in ImageJ software.

2.4.2 PrestoBlue™ Assay

PrestoBlue™ cell viability reagent was obtained from ThermoFisher. It is a ready-to-use cell permeable resazurin-based solution that functions as a cell viability indicator by using the reducing power of living cells to quantitatively measure the proliferation of cells.

Resazurin is a non-toxic, cell-permeable compound that is blue in color and virtually non-fluorescent. Within cells, resazurin is reduced to resorufin, which produces a highly fluorescent red color. Viable cells continuously convert resazurin to resorufin, thereby generating a quantitative measure of viability and cytotoxicity.

A mother solution of PrestoBlue™ reagent with DMEM medium (1:10) was prepared and 300 µL was added to each insert and device and incubate at 37 °C and 5 % CO_2, protected from direct light. Four hours of incubation time to increase sensitivity was used and readings were taken in a 96-well plate at multiple time points (1h, 2h, 3h, and 4h). Using a microplate reader (BioTek Synergy H1), the fluorescence was read using a fluorescence excitation wavelength of 560 nm (excitation fluorescence is 540 to 570 nm) (**Figure 14**).

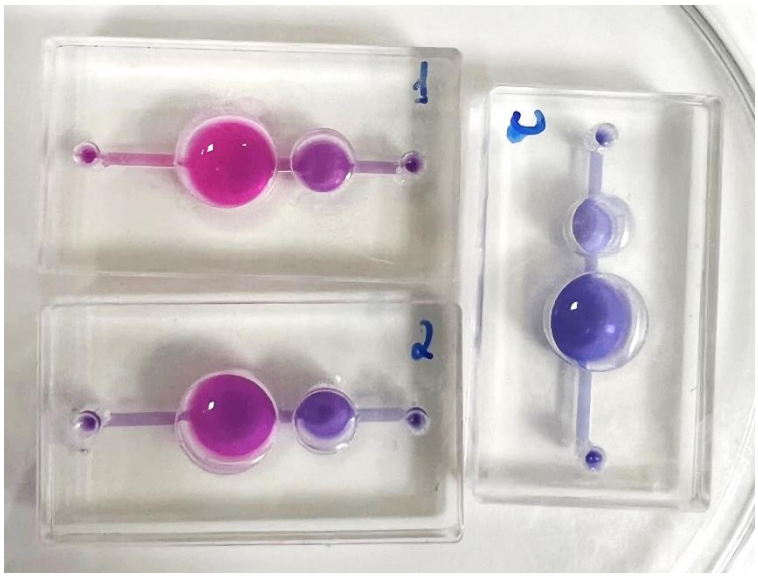

Figure 14 – PrestoBlue™ cell viability reagent added to EoC 1 and 2, and to EoC control after 2 hours of incubation.

The PrestoBlue™ cell viability reagent is a complete add-and-read, a non-toxic reagent that does not require cell lysis. Since no lysis is required the diluted PrestoBlue™ solution can be removed, then replaced with complete growth media or washed to posterior staining.

2.5 Epidermis Morphology, Organization, and Membrane Integrity

2.5.1 Trans-Epithelial Electrical Resistance (TEER)

The barrier integrity of the developed models was evaluated by TEER. Measurements were taken using an EVOM² Epithelial VoltOhmmeter (Merck) and were performed every 2 days from day 0 at ALI.

An increase in TEER detected with the electronic circuit of the EVOM² Epithelial VoltOhmmeter and its electrode is an indication of cell monolayer health and confluence. A silver/silver chloride (Ag/AgCl) pellet on each electrode tip measures voltage. The small size of the electrode enables the user to easily measure transepithelial voltage and the resistance of cells grown on microporous membranes.

Proper placement of the electrode in the cell is critical to making accurate measurements (**Figure 15**). The lengths of the electrode tips are unequal allowing the longer electrode tip to touch the bottom containing the external culture media while preventing the shorter one from reaching the tissue culture. This feature ensures proper positioning between the electrodes and the cell layer during the trans-

membrane measurement. In addition, by positioning the longer tip so that it touches the bottom each time, the reproducibility of the measurements is significantly improved. For disinfecting, the electrode tips were immersed in ethanol for 15 min. Just before use, they were rinsed with the culture medium and then used directly for the TEER measurements.

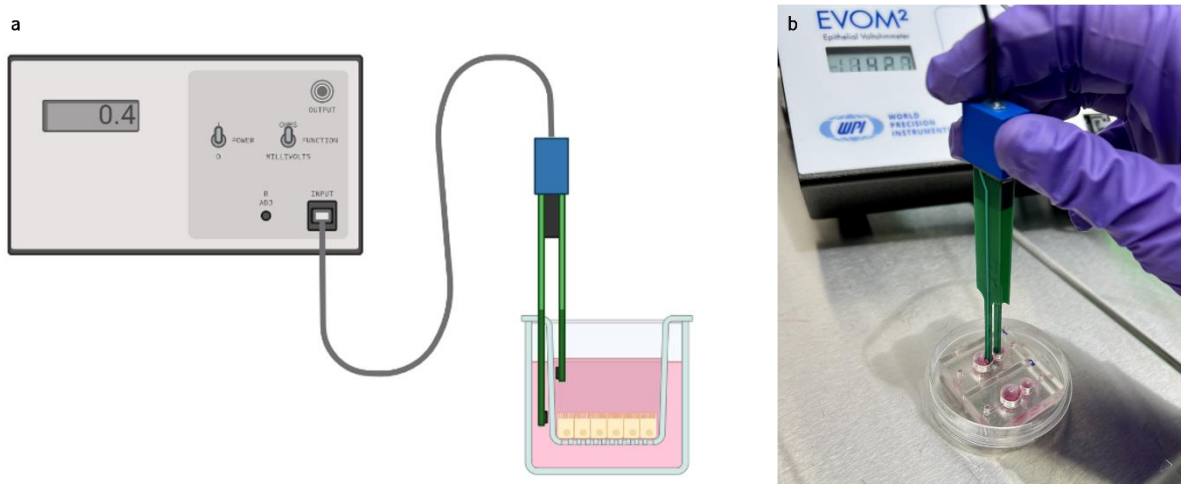

Figure 15 – (a) Schematic illustration of the correct position for the TEER measurements. Figure generated in BioRender; (b) TEER measurement on EoC.

Phase contrast microscopic images were also taken at the same days of the TEER measurements to provide an extra information about the tissue formation correlating TEER measurements with microscopic observation. Damaged tissues show lower TEER values. Thus, microscopic visualization is essential to understand what happens to tissue formation over time.

2.5.2 Histology Analysis

The reconstructed tissues were fixed immediately after being taken out of culture in 10% neutral buffered formalin (Sigma-Aldrich). The samples were embedded in paraffin to allow for transverse sectioning. Paraffin-embedded sections were de-paraffined and re-hydrated for morphological evaluation by staining with hematoxylin and eosin (H&E) through standard methods.

The hematoxylin and eosin (H&E) stain is the primary diagnostic stain performed on all formalin-fixed skin samples and provides a comprehensive picture of the microanatomy of organs and tissues.

Hematoxylin precisely stains nuclear components a purplish blue, while eosin stains cytoplasmic components including collagen and elastic fibers pink.

2.5.3 Immunocytochemistry Analysis

2.5.3.1 Fluorescence Microscopy

Fluorescence microscopy plays an important role in molecular and cell biology since fluorescent labels allow for the visualization of cell structures and sub-cellular components that a conventional optical microscope without fluorescence cannot capture [70].

Fluorescence is the ability of a substance to emit light when exposed to electromagnetic radiation. An atom absorbs energy, becomes excited, and transitions to a higher electronic state. It then loses energy and returns to the fundamental state, emitting a photon. The energy that is absorbed is always greater than the energy emitted, so the excitation wavelength is always shorter than the emission. This happens due to the loss of energy between excitation and emission – Stokes Shift [70, 71].

Fluorescence can also be defined as the radiative transition (the loss of energy is due to the emission of photons) in a molecule between electronic states of the same multiplicity, generally starting from the excited electronic state of lowest energy. Thus, fluorescence microscopy is based on the phenomenon in which a certain material emits energy, at a certain wavelength, greater than that of excitation. The material may emit self-fluorescence or require treatment with fluorophores [70, 71].

The most usual application of the phenomenon of fluorescence is excitation in the UV region of the electromagnetic spectrum, to obtain radiation emitted in the visible region, which gives fluorescent substances a distinct coloration that is visible when exposed to UV radiation. Fluorescence is distinguished from other types of photoluminescence by the fact that the excited molecule returns to the ground state immediately after excitation. Additionally, photobleaching can occur when fluorophores lose their ability to fluoresce because of cells' constant irradiation by excited electrons and subsequent damage might happen, limiting the time for sample observation [71].

Confocal microscopy is based on fluorescence microscopy. The main difference is that while confocal microscopy uses pinholes to define a sharp focus section, fluorescence microscopy uses light from several focal planes of the specimen. As a result, the image that is obtained is sharper and has better quality and resolution [72].

Furthermore, the modern scanning mechanisms implemented in confocal laser scanning microscopy, based on deflected mirrors that move the focus point in the XY plane, enable the reconstruction of an

image by information collected from each point, and moreover, if the focus point is also scanned in the Z-axis, a 3D image can be generated with high resolution [72, 73]

2.5.3.2 Tight Junctions, Cytoskeleton and Nuclei

Cell reconstructed tissues were carefully washed with warm phosphate-buffered saline (PBS, 1X) to eliminate medium residues. Cells were subsequently fixated with 4% paraformaldehyde (PFA, Sigma Aldrich) for 15 minutes at RT, rinsed with cold PBS (1X) thoroughly, and permeabilized with 0:2% Triton X-100 in PBS. Triton-X-100 is the most popular detergent for improving the penetration of the antibody. After washing three times with cold PBS, the fixed cells were incubated with a 2 % (w/v) BSA solution in PBS (blocking buffer solution) to minimize non-specific antibody bonding, for 30 minutes (it is ok to leave for longer periods of time, 2 to 3 hours). Subsequently, phalloidin conjugated to tetramethyl rhodamine isothiocyanate – TRITC (1:100) and Occludin Monoclonal Antibody – OC-3F10, Alexa Fluor™ 488 (1:100) solutions were added to the antibody-diluting buffer (dilution of the stock BSA solution in PBS to achieve 0.5 % BSA) and incubated overnight in the dark at 4 °C.

After extensive wash with PBS, cells were counterstained with 1 µg/mL 4′,6-diamidino-2-phenylindole (DAPI) solution for 10 min at RT. Laminas were mounted using a fluoromount and lamellas were sealed with nail polish to prevent drying and movement under a microscope. Images were acquired using a confocal microscope (Zeiss LSM780) equipped with 405 nm and 561 nm diode lasers and a 488 nm argon laser and were analyzed using Zen 2010 software and treated on ImageJ software.

2.5.3.3 Keratin-10, Keratin-14 and Nuclei

Immunocytochemistry analysis was also made to examine the distribution of K14 (basal cell layer), K10 (early differentiation), and loricrin (late differentiation) in the reconstructed human epidermis.

The first staining steps were the same as the ones mentioned above (*2.6.3.1*). After the incubation with a 2 % BSA solution for at least 30 minutes, the primary antibodies – Cytokeratin 14 Monoclonal Antibody (LL002, Invitrogen), Cytokeratin 10 Monoclonal Antibody (RKSE60, Invitrogen), and Loricrin Polyclonal Antibody (PA5-30583, Invitrogen) – in antibody-diluting buffer (1:500) were incubated overnight in the dark at 4 °C.

The solutions were removed, and the cells were washed with PBS. Then, the respective secondary antibodies – Goat anti-Mouse IgG (H+L), Superclonal™ Recombinant Secondary Antibody, Alexa Fluor 488 (A28175, Invitrogen), Donkey anti-Rabbit IgG (H+L), Alexa Fluor 594 (21207, Invitrogen), and Goat anti-Mouse IgG (H+L), Alexa Fluor™ 635 – in 0.5 % BSA (1:500, 1:100, and 1:1000, respectively) were incubated for 1 h at RT in the dark. Lastly, after washing with PBS, cells were also counterstained with 1 µg/mL DAPI solution for 10 min at RT.

2.6 Rutile-TiO_2 Nanoparticles Exposure to Epidermis-On-a-Chip

EoC established on day 14 at ALI was incubated with rutile-TiO_2 NPs at 100 µg/mL concentration for 48 h (**Figure 16**). This concentration and time point were chosen based on the previous experience of the Sanches et al. group [74]. Then, the cell viability was assessed by PrestoBlue™ assay.

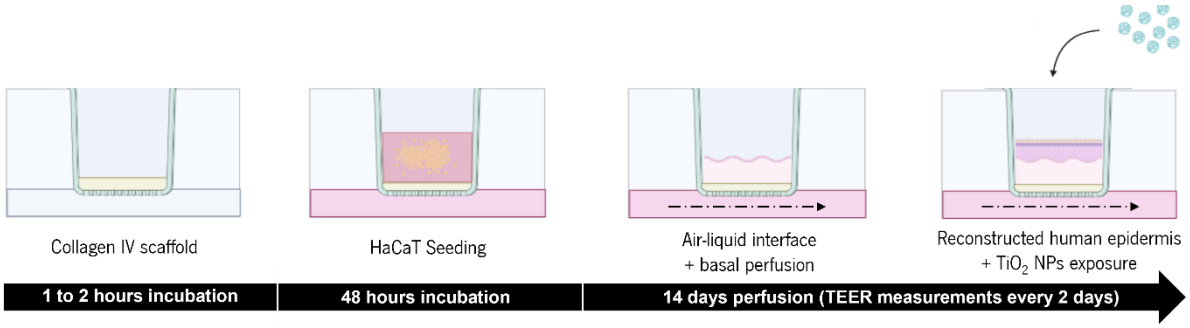

Figure 16 – Schematic representation of the developed methodology for reconstructed human epidermis generation on microfluidic EoC devices. Figure generated in BioRender.

CHAPTER 3

RESULTS AND DISCUSSION

3.1 Rutile-TiO_2 Nanoparticles

TiO_2 is a semiconductor material with several applications such as pigments, optical filters, antireflection coatings, chemical sensors, catalysts, and sterilization materials that belongs to the family of transition metal oxides. Nanoparticulate TiO_2 can be used in sunscreens to prevent UV-A and UV-B irradiation. The size, shape, and crystallographic phase of the TiO_2 NPs affect how well they backscatter UV radiation. From the literature it is known that there are three polymorphs of TiO_2 that can be found in nature: rutile, anatase, and brookite. Rutile TiO_2 has 6 atoms per unit cell and a tetragonal structure. Is stable at most temperatures and pressures up to 60 kbar and becomes the thermodynamically favourable phase [75, 76]. The properties of the TiO_2 NPs sample obtained commercially are shown in **Table 5**.

Table 5 – Properties of the TiO_2 NPs obtained commercially.

Commercial name	Nature of the surface	Surface area	Density	Particle size
Titanium oxide nanopowder	99.5% rutile	50 m^2/g	4.23 g/cm^3	10-30 nm

To confirm NPs identity, a physicochemical characterization of commercially available NPs was performed by XRD, XPS, Raman spectroscopy, and DLS.

3.1.1 Physicochemical Characterization of Rutile-TiO_2 Nanoparticles

The physicochemical characterization of rutile NPs is presented in **Figure 17**.

The rutile crystal structure was confirmed by XRD (see spectra (a)). All of the diffraction peaks were identified as characteristic of the XRD pattern of rutile-TiO_2. The presence of diffraction peaks at (110), (101), (200), (111), (210), (211), (220), (002), (310), (301), (311) and (202) lattice planes, respectively, indexing to a pure and highly crystalline rutile-TiO^2 phase. This spectrum is in good agreement with the spectra of Thamaphat et al. [77]. No additional peaks corresponding to impurities and other structural phases were detected, which indicates the high crystallinity and purity of the rutile-TiO^2 phase.

Spectra (b) is related to Raman spectroscopy and exhibited major peaks at 401 and 638 cm^{-1} with a minor peak at 247 cm^{-1} verifying the rutile phase of the NPs. This spectrum is in good agreement with the spectra of Balanchandran and Eror [78]. To determine the composition and identify the chemical states of rutile TiO^2 nanocrystals, XPS analysis was carried out.

In turn, (c) shows Ti 2p and O 1s regions of the high-resolution XPS spectra of rutile TiO_2 NPs. The two strong peaks from the rutile at around 459.5 eV with symmetry can be attributed to Ti 2p1/2 and Ti 2p3/2. The peak positions and 5.8 eV peak separation of the Ti 2p doublet agree well with the energy reported for TiO_2 NPs. O 1s peaks is located at about 529.09 eV, and Ti 2p, O1s peaks positions, and the line shapes are characteristic of stoichiometric TiO_2 [79]. The carbon source is probably surface contamination with adventitious hydrocarbons. Resuming the physicochemical characterization performed on the commercially available NPs confirms that they are TiO_2 NPs with a rutile crystal structure.

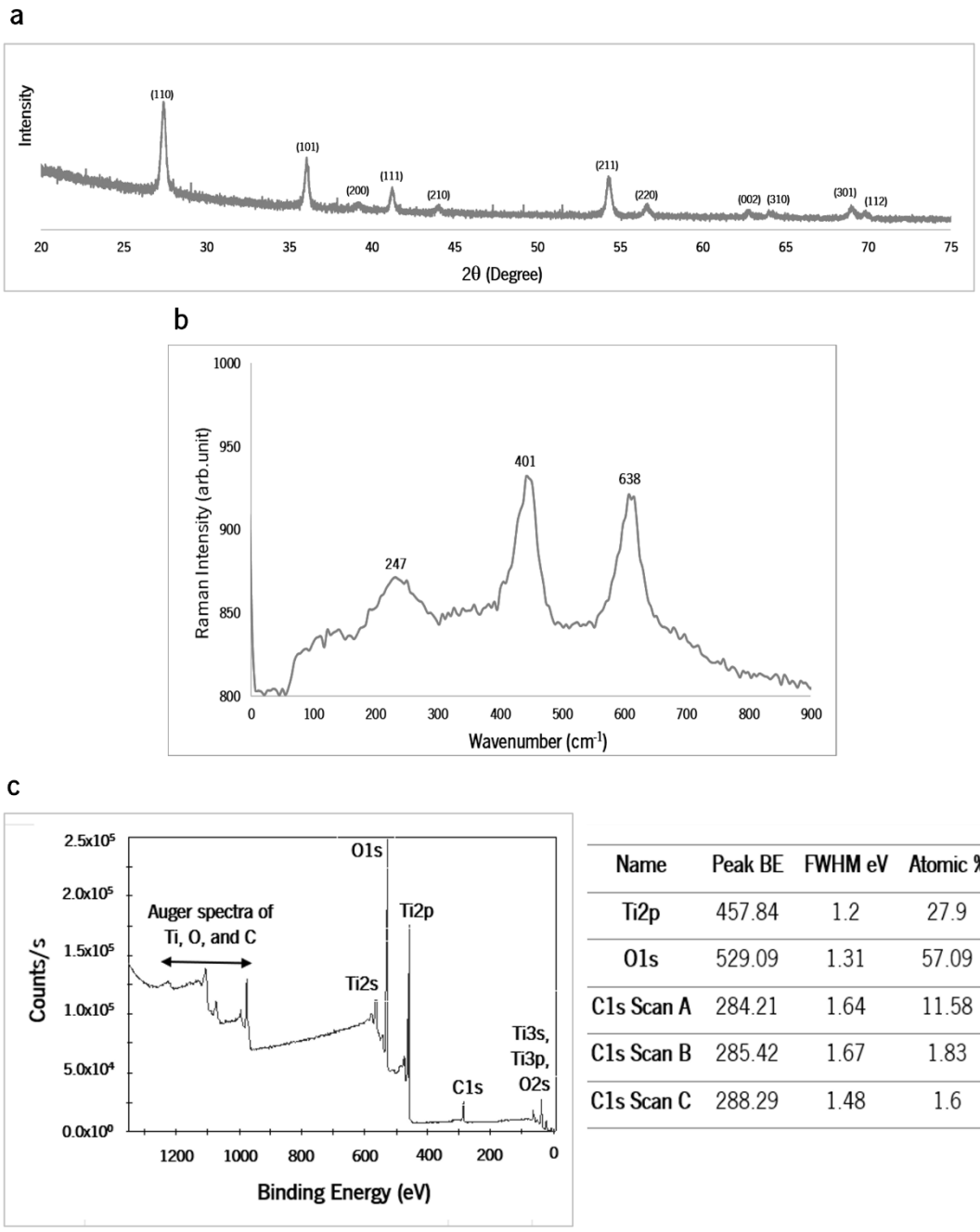

Name	Peak BE	FWHM eV	Atomic %
Ti2p	457.84	1.2	27.9
O1s	529.09	1.31	57.09
C1s Scan A	284.21	1.64	11.58
C1s Scan B	285.42	1.67	1.83
C1s Scan C	288.29	1.48	1.6

Figure 17 – Physicochemical characterization of rutile NPs: (a) XRD of TiO_2 powder; (b) Raman spectra; (c) XPS spectra and table with the atomic percentage of each element.

3.1.2 Dispersion of Rutile-TiO_2 Nanoparticles

Sonication is the application of sound energy at frequencies over 20 kHz, which are largely inaudible to the human ear, and facilitate the disruption of particle agglomerates. Compared to other conventional dispersion techniques, ultrasound disruption is more energy-efficient and can achieve a higher degree of powder fragmentation at constant specific energy. Sonication is a practical, relatively inexpensive, and easy-to-use to maintain equipment. Consequently, sonication has found extensive application in toxicological and environmental studies, where it is used to break down powders or re-disperse stock suspensions to their nanoscale constituents and enable the study of the characteristics and behavior of the dispersed NPs in relevant systems. However, the variability in observed results has probably been influenced by the variable use of ultrasonic equipment between laboratories and between individual operators, as well as by the absence of a widely accepted standardization process [80].

Sound waves that are typically in the 20–40 kHz range travel through the liquid medium during the ultrasonic disruption process in cycles of alternating high and low pressure. Cavitation, a phenomenon that occurs during the low-pressure cycle (rarefaction), is the formation of small vapor bubbles. Then, during the high-pressure cycle (compression), the bubbles collapse, causing a localized shock wave that releases a significant amount of mechanical and thermal energy. Ultrasonic waves can be generated in a liquid suspension either by immersing an ultrasound probe (transducer horn) into the suspension (direct sonication) or by introducing the sample container into a liquid that is propagating ultrasonic waves (indirect sonication). In all cases, the ultrasonic device transforms electrical power into vibrational energy. The amplitude of oscillation per unit of time determines the pressure difference between cavitational rarefaction and compression cycles. Larger oscillation amplitudes yield larger high-low pressure gradients and consequently greater energy outputs. [80]. In this work, direct sonication was used to reduce the physical barriers to wave propagation and therefore deliver a higher effective energy output into the TiO_2 NPs suspension.

The efficiency of the energy transformation from the electrical source to the acoustic power actually received by the sonicated suspension depends heavily on the instrument. Therefore, simply reporting the sonicator's power setting value (e.g., 50 %) does not provide an accurate indication of the effective acoustic power delivered to the sonicated suspension and is as such reporting parameters that do not allow for transferable or reproducible results. Taurozzi et al. propose the calorimetric method as a simple procedure to establish a standardized, instrument-independent, transferable and reproducible method for the measurement and reporting of sonication power [80].

3.1.2.1 Calorimetric Determination of the Delivered Acoustic Energy

Three different beakers containing 300 µL of Milli-Q water were weighed and temperature measurements were taken every 30 s over 5 minutes of direct probe sonication with different amplitudes (30, 50, and 70 %) allowing for the construction of a T vs t diagram to determine the linear fit for the curve using the least square regression line (**Figure 18**). In turn, **Equation 8** (*2.1.2*) was used to calculate the delivered acoustic power for each amplitude, and the respective specific energy was calculated by **Equation 7** (*2.1.2*).

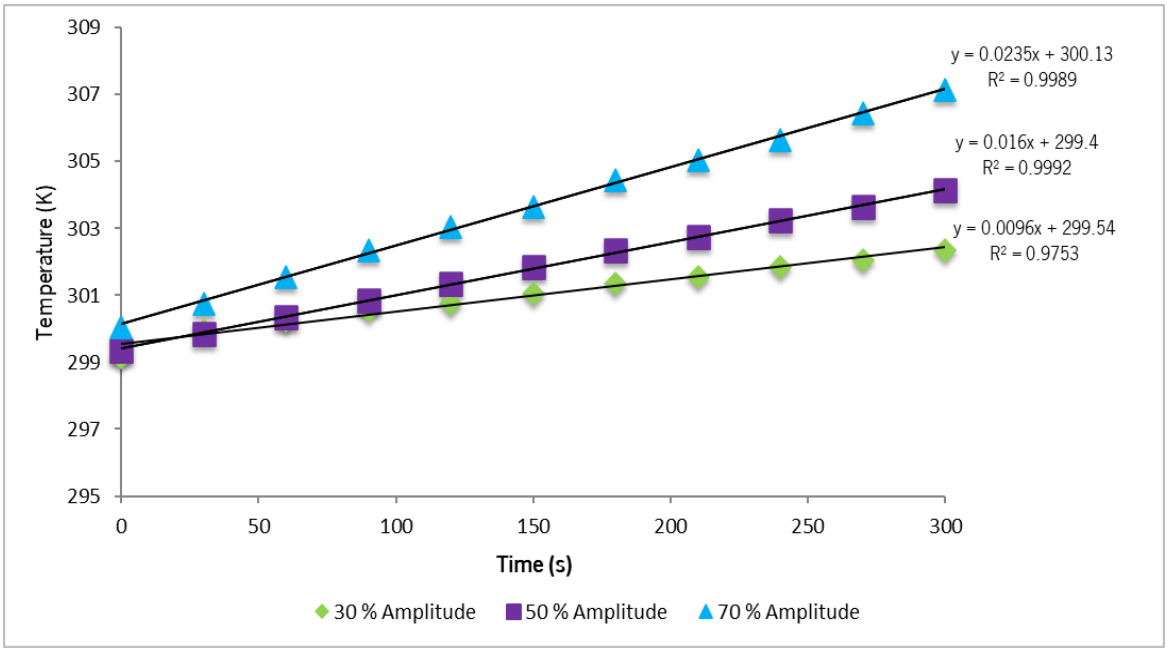

Figure 18 – T vs t diagram with respective linear fits for each amplitude measured.

The delivered acoustic power determined for the amplitudes of 30, 50, and 70 % are 11.500 J/s, 18.886 J/s, and 29.105 J/s, respectively. Consequently, the specific energies for each power ranges measured are 1.15×10^4 KJ/m³ to 30 % amplitude, 1.89×10^4 KJ/m³ to 50 % amplitude, and 2.91×10^4 KJ/m³ to 70 % amplitude.

3.1.2.2 Assessment of the Z-Average of Rutile-TiO_2 Nanoparticles in Water and Culture Medium

Dry powders are composed of fine particles that are bound together into macroscopic structures by both weak physical Van der Waals forces and stronger chemical bonds including particle fusion. These powders often comprise micrometer- and submicrometer-scale aggregates, which are then physically bound together to constitute larger agglomerates (**Figure 19**). The nominally weaker Van der Waals forces can

be very strong for powders consisting of nanoscale particles and aggregates, which means they have substantial interfacial contact areas per unit volume. This makes it necessary to use methods such as sonication to effectively break down or disrupt powder agglomerates [80, 81].

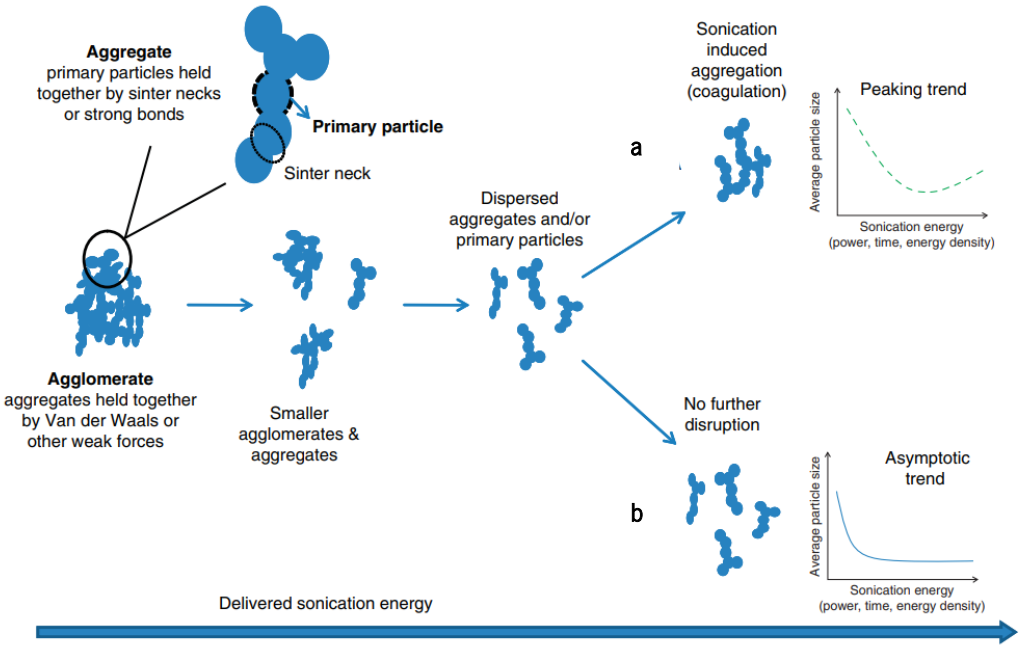

Figure 19 – Schematic representation of the particle agglomeration and aggregation, and Illustration of the typical effects of sonication on particle size as a function of supplied sonication energy: (a) asymptotic behavior – solid line; (b) peaking behavior – dashed line *[80]*.

DLS analysis reveal that rutile-TiO_2 NPs in water were agglomerating presenting a Z-average size of 13649 nm. When NPs came into contact with aqueous media, they tended to agglomerate in micrometre-sized structures. Thus, a suitable dispersion protocol of rutile NPs in water was developed. Sonication parameter optimization studies were performed by preparing stock solutions with different concentrations (2 mg/mL, 1mg/mL, 0.5 mg/mL, and 0.2 mg/mL) of rutile-TiO_2 aqueous suspensions and testing them with different energies and times of sonication.

The acquired hydrodynamic size results of Rutile-TiO_2 NPs dispersions with concentrations of 2 mg/mL and 1 mg/mL at three different amplitudes, 30 %, 50 %, and 70 % are shown in **Table 6**. As can be observed increasing the concentration of nanoparticles there was an increase in the mean diameter. Probe sonication can not only break agglomerates locally but also promote re-agglomeration due to enhanced particle-particle interactions [81]. This is consistent with the observations made after 24 hours of stabilized sonicated suspensions where we verified a complete sedimentation of the NPs (**Figure 20**). Consequently, for a higher concentration of NPs, with increasing sonication energies, the dispersion hydrodynamic size decreased initially and then increased.

Table 6 – DLS values for rutile-TiO_2NPs suspensions with 2 mg/mL and 1 mg/mL concentrations.

	2 mg/mL		1 mg/mL	
	Z-Average (nm)	PDI	Z-Average (nm)	PDI
30 %	15361	0.251	21716	7.302
50 %	15905	5.174	11328	1.402
70 %	19206	9.251	6642	2.311

Figure 20 – NPs sedimentation in 2 mg/mL sonicated suspension after 24 h of stabilization.

NPs concentration and sonication have a great influence on TiO_2 NPs hydrodynamic diameter. Therefore, the same energies and time conditions were tested for suspensions with lower final concentrations of 0.5 mg/mL and 0.2 mg/mL. Three replicates were performed, and Z-Average and PDI obtained by DLS for a specific energy of $1.15x10^4$ KJ/m^3 (corresponding to 30 % amplitude) and a sonication time of 15 min (in pulsed mode) showed favorable values presented in **Figure 21**. The polydispersity index (PDI) is a measure of the heterogeneity of a sample based on size, which value less than 0.1 implies monodisperse particles and values more than 0.1 may imply polydisperse particle size distributions [82].

For 0.5 mg/mL, at time 0, the suspensions showed a Z-average of 316 nm and a PDI of 0.330, and 48 h after sonication, they showed values of 328 nm and 0.277, respectively. In turn, for 0.2 mg/mL, a Z-average of 276 nm and PDI of 0.342 was obtained at time 0, and after 48 h stabilization, the values are a Z-Average of 499 nm and a PDI of 0.354. This reduction in size can be explained by the increase in electrophoretic mobility, which increases the electrical double-layer repulsive forces between NPs and, consequently, prevents particles from aggregating [83].

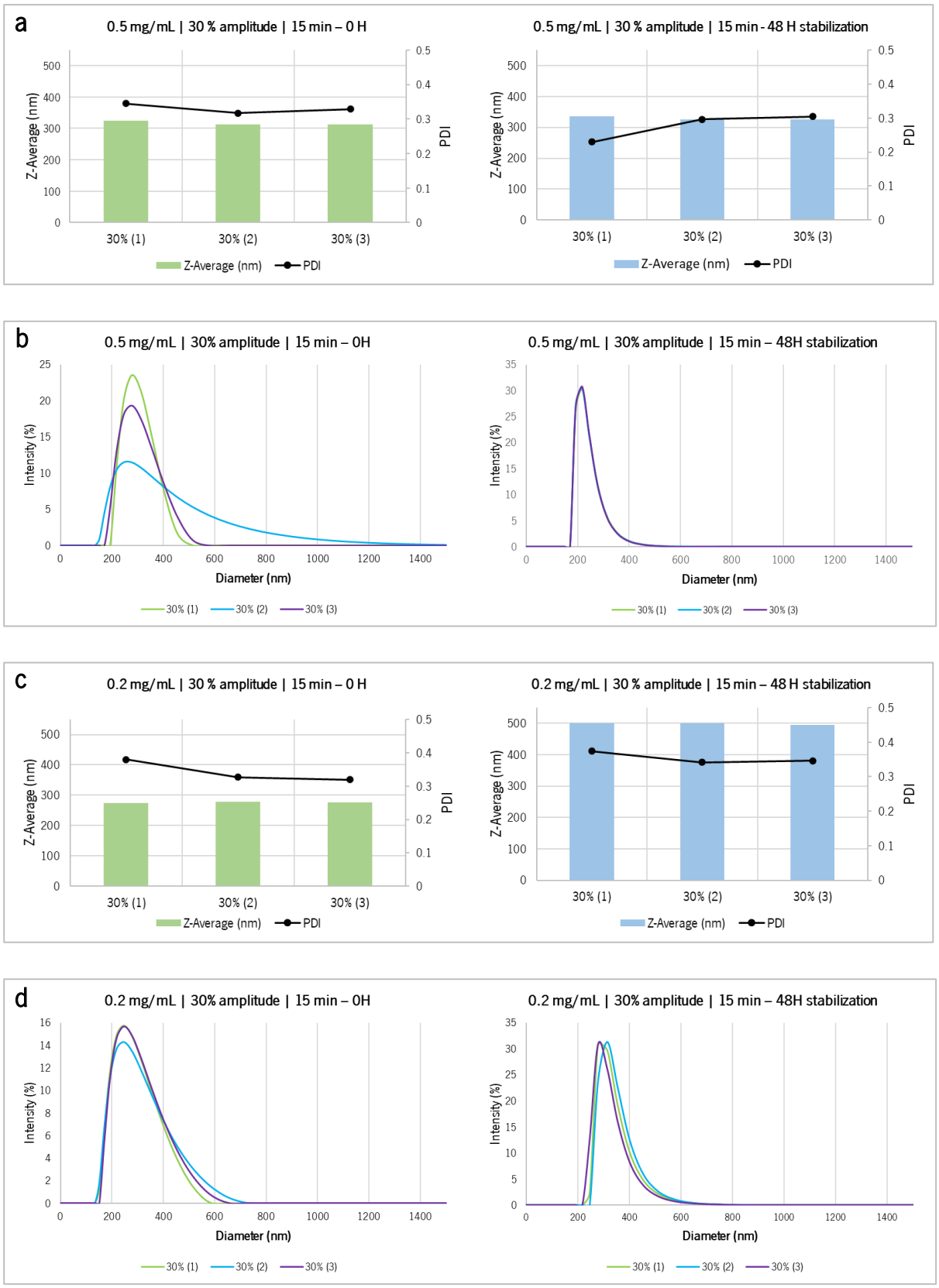

Figure 21 – DLS analysis. (a) and (c): Z-average and corresponding PDI for 0.5 mg/mL and 0.2 mg/mL final concentration at time 0 and 48 hours after stabilization, respectively; (b) and (d): diameter versus intensity plots for each measurements revealing their sizes (nm).

As the concentration of 0.5 mg/mL seems to be more stable different times of sonication in pulsed mode (15, 20, 25, and 30 min) were tested. Z-Average and PDI results obtained by DLS showed promising values for 30 min of pulsed mode sonication. **Figure 22** exhibited the Z-Average and corresponding PDI achieved for each replicate at time 0 and after 24 and 48 h stabilization, such as the diameter versus intensity plots obtained by DLS analysis.

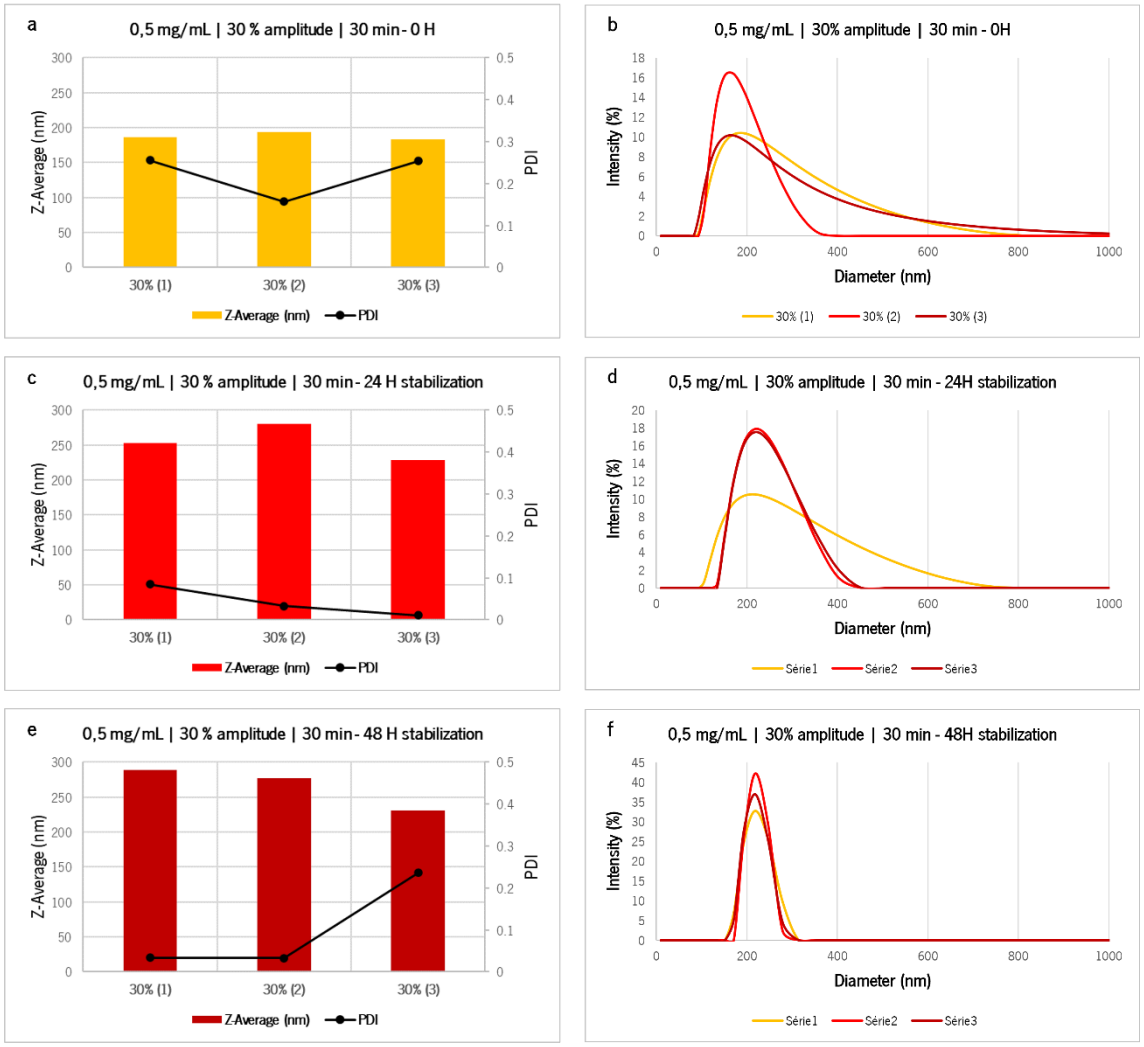

Figure 22 – DLS analysis. (a), (c), and (e) Z-average and corresponding PDI for 30 min of sonication of a 0.5 mg/mL final concentration suspension with $1.15x10^4$ KJ/m^3 specific energy at time 0, and 24 and 48 hours after stabilization, respectively; (b), (d) and (f) diameter versus intensity plots for each measurements revealing their sizes (nm).

As it can be seen increasing time of dispersion the average size was lower compared with 15 min of dispersion. Besides that, increasing stabilization periods, it was possible to observe a reduction in PDI confirming the presence of a more stable and monodisperse dispersion of TiO_2 NPs.

Upon establishment of the best TiO_2 NPs dispersion condition in water (30 % amplitude, 30 minutes of pulsed mode), they were incubated in medium culture normally used to cultivate keratinocytes. Resuming, the dispersed rutile stock solution stabilized for 24 hours and was diluted to a concentration of 1 mg/mL

in the specific culture media (DMEM High glucose 10% FBS). As it can be observed there was an increase in the hydrodynamic size (**Figure 23.a**) upon incubation of TiO_2 NPs in medium culture. The media is rich in ionic species that can affect the surface charge of NPs, leading to a reduction in the electrostatic repulsive forces and causing the observed agglomeration. Besides, that culture media is also rich in different proteins present in serum that are known to adsorb onto rutile NPs, contributing to the noted agglomeration [74].

Different dispersants have been already applied to NPs, namely natural surfactants, phospholipids, organic solvents, and serum or albumin. Bovine serum albumin (BSA) is often used as a stabilizing agent, since it is a multifunctional protein present in plasma, and it is used in many media for toxicological studies. Ji et al. used BSA as a protein-rich supplement to improve TiO_2 NP dispersion in mammalian, bacterial, and yeast cell culture media [84]. Based on previous results of the Sanches et al. group, BSA at a final concentration of 0.6 mg/mL was added to the suspension before incubation in DMEM and a reduction in rutile hydrodynamic size was observed [74]. DLS analysis showed that, at a constant rutile concentration, BSA was effective in reducing agglomeration where a hydrodynamic size of 226 nm was obtained (**Figure 23.b**). The adsorption of BSA on rutile NP surfaces may possibly occur through electrostatic, hydrophobic, or specific chemical interaction. This agrees with the literature, where BSA is largely used as a stabilizing agent preventing NP agglomeration [83, 74]

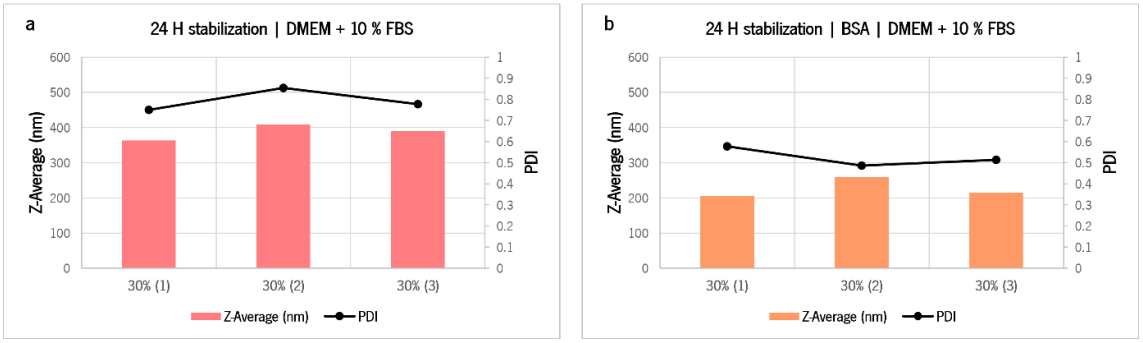

Figure 23 – DLS analysis. (a) Z-average and corresponding PDI for dispersed rutile stock solution stabilized for 24 h diluted in DMEM + 10 % FBS; (b) Z-average and corresponding PDI for dispersed rutile stock solution stabilized for 24 h in DMEM + 10 % FBS with previous addition of BSA as a stabilizing agent.

Resuming, before exposing TiO_2 NPs to the EoC, NPs should be dispersed at the concentration of 0.5 mg/mL with an energy of $1.15x10^4$ KJ/m^3 for 30 min in pulsed mode. Upon 24h stabilization, NPs should be incubated with 0.6 mg/mL BSA and then complete medium culture. It is important to stress that each NPs requires a protocol of dispersion and changing the cell culture medium may require a new dispersion as well as stabilization.

3.2 Design and Fabrication of the Epidermis-On-a-Chip

The basic structure of the epidermis-on-a-chip consists of three PMMA layers assembled, molding a 2 cm wide and 3.5 cm long microfluidic device. **Figure 24** shows the design (a) with the respective dimensions of the device fabricated as well as a schematic structure (b) and photographs (c) of the same. The apical layer included a central cavity designed to accept the cell culture layer and a smaller cavity that allow TEER measurements as well as facilitate the seeding of an additional cell under PET membrane.

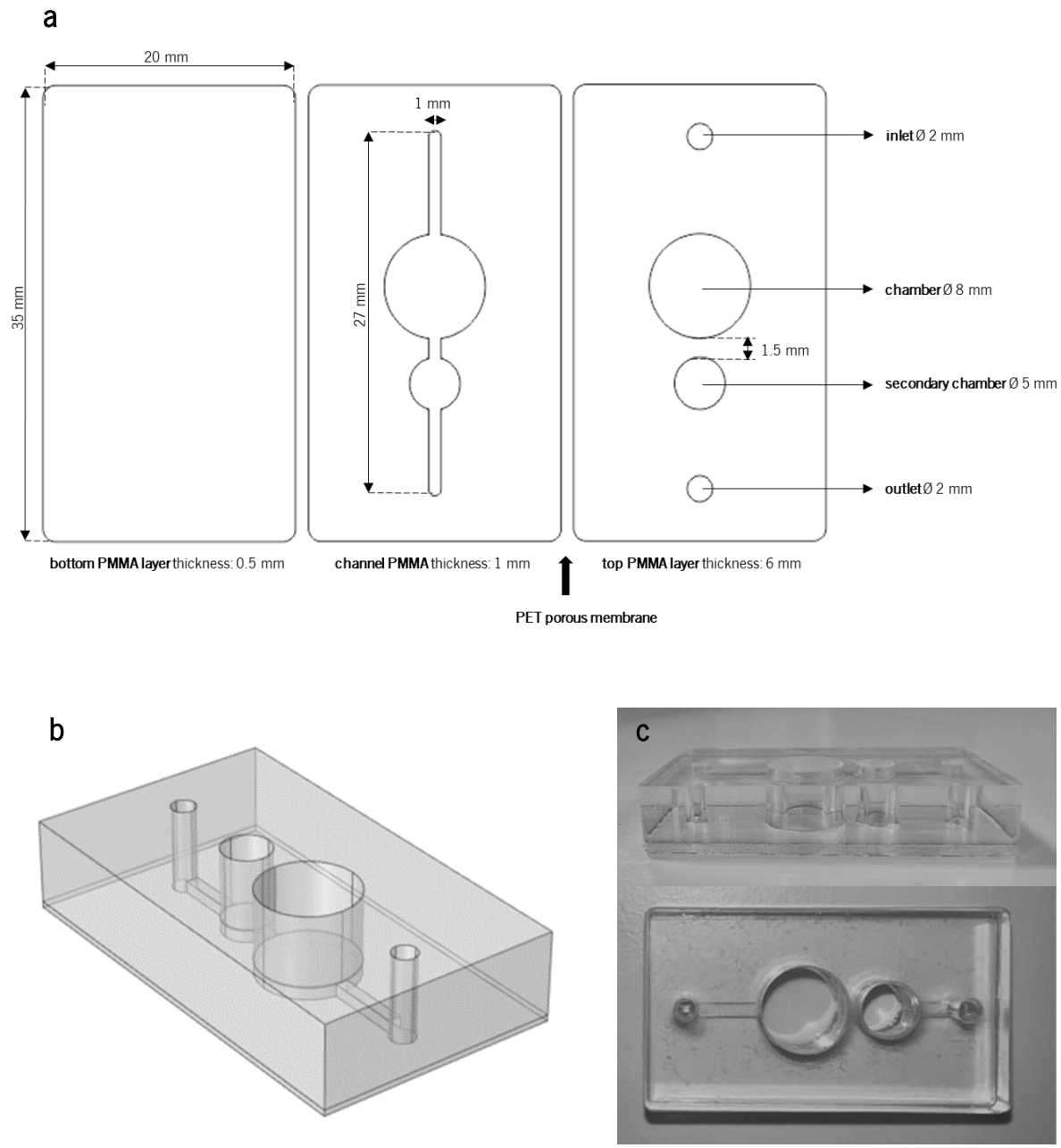

Figure 24 – Epidermis-on-a-chip: (a) Design with respective dimensions; (b) schematic structure; (c) real photographs.

Firstly, the PMMA sheets were previously laminated with double-sided tape (3M) and then cut on the laser cutter. The upper layer has a thickness of 6 mm and comprises the cell culture chamber and a secondary chamber with a diameter of 8 mm and 5 mm, respectively. In turn, the middle PMMA layer consists of the microfluidic channel having a length of 27 cm, and a width and height of 1 mm. Furthermore, a PET porous membrane was sandwiched between the top and the mid-PMMA layers to separate the cell culture chamber of the microfluidic channel and support the collagen IV matrix. To seal the microfluidic channel, a lower PMMA sheet with a thickness of 0.5 mm was used. Lastly, the fluidic inlet and outlet have a diameter of 2 mm. The inlet was connected to culture media through a set of PTFE tubing with an inner diameter of 0.5 mm, consecutively connected to a syringe by Tygon® tubing, and the outlet was connected to a reservoir flask.

The stability of the proposed epidermis-on-a-chip microfluidic device fabricated was tested. Primarily, some tests were done with water on two devices without cells using a syringe pump with two syringes. The amount of water that enters the channel must be equal to the amount that leaves the channel. With a flow rate of 1000 µL/h, approximately 2 mL of water should come out in 2 h, and there should be approximately 2 more grams in the weight of the empty flasks, as proved in **Table 7**.

Table 7 – Weight of the flask before and after water perfusion.

	Weight of empty flasks	Weight of the flasks 2 h later	Difference
Flask 1	18.594 ± 0.001 g	20.546 ± 0.001 g	**+ 1.952** ± 0.001 g
Flask 2	18.891 ± 0.001 g	20.889 ± 0.001 g	**+ 1.998** ± 0.001 g

These results confirm the stability and tightness of the chip, where no water loss was observed.

3.2.1 Computational Study of the Epidermis-On-a-Chip

The epidermis-on-a-chip device fabricated is composed of a simple round cell chamber with one inlet and one outlet, and the bottom surface of the cell culture chamber is a membrane with a cell layer. Every model needs to make certain assumptions or approximations about details we might not fully know such as the surface of the cell layer being smooth and flat and non-slip, but in reality, there is always some roughness, and as such shear force can be higher in some spots and lower in others. However, the average shear rate is correct, and knowing the velocity of the flow in the chamber, we can compute his profile at the bottom of the chamber.

The culture media perfusion was done with a 1 µL/min flow rate and goes along the cell layer. **Figure 25** demonstrates the results of the FEM study. First, the flow profile was calculated using the laminar model, and images (a) and (b) indicate that the flow rate is high close to the inlet and outlet but spreads out then quickly to the chamber. The flow resistance of the cell chamber is 1.6×10^{8} Pa.s/m^{3}. Image (c) shows the distribution in the chamber, where near to the inlet and outlet is saturated. In turn, images (d) and (e) show that the shear force along the channel axis is highest close to the inlet/outlet: 16×10^{-5} Pa, and in the center, it is much lower, below 1.72×10^{-5} Pa, and in the perpendicular direction, the shear force is the highest in the center, and in the edge, it is the lowest at 1×10^{-6} Pa.

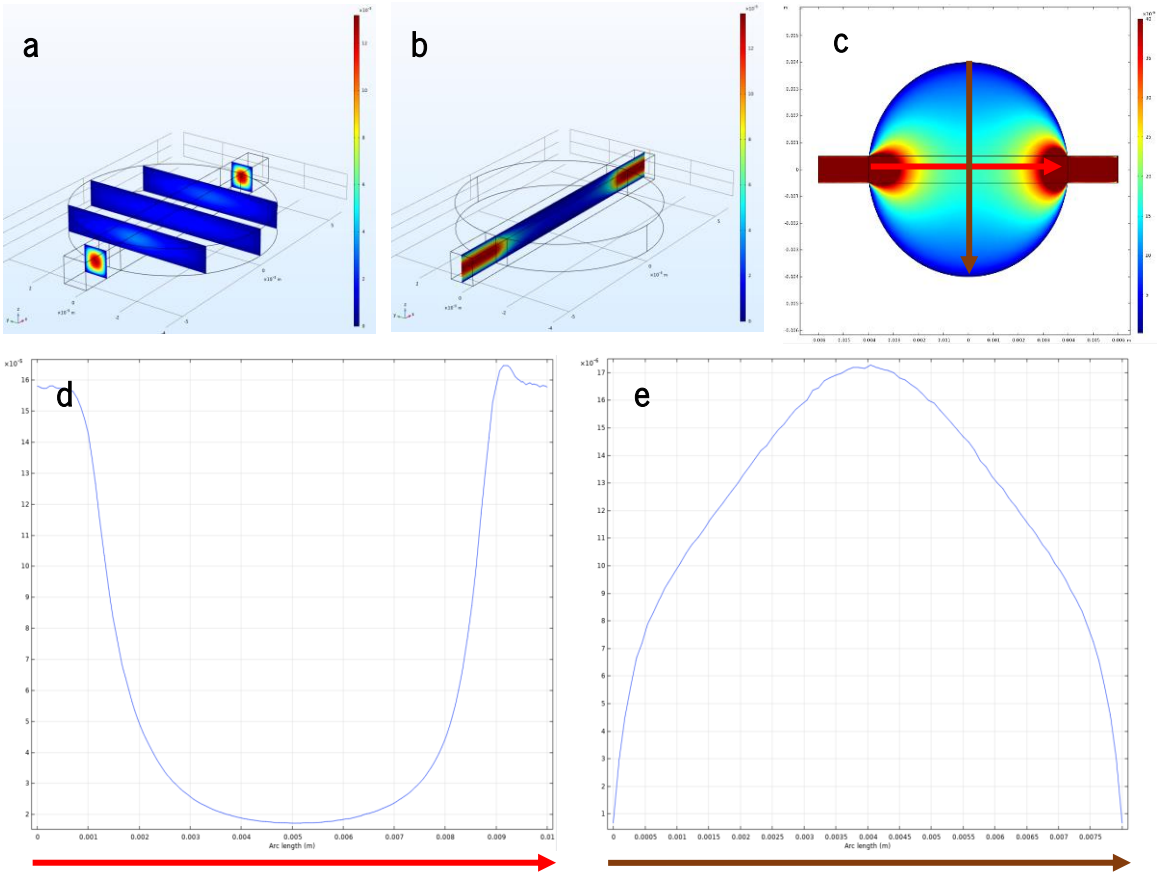

Figure 25 – Computational simulation: (a) and (b) flow profile using the laminar model; (b) shear rate profile on the bottom of the chamber; (d) shear force profile along the channel axis; (e) shear force profile in the perpendicular direction.

As reported, the application of shear stress to skin tissue results in improved barrier function, improved epidermal differentiation, and increased density in skin tissue. The magnitude of shear stress exposure on keratinocytes influences cell viability, and it has been demonstrated that high shear stress (6 dyne/cm^{2} = 0.6 Pa) results in cellular disruption [41, 85]. Hence, low shear during cell culturing should be considered necessary to improve skin models. Concluding, at a 1 µL/min flow rate in the designed EoC microfluidic device, no shear stress forces will impair good cell growth and differentiation.

3.2.2 Preliminary Experiment with Caco-2 Cell Line

The stability of the device and ability to support cell growth was evaluated using a Caco-2 cell line model since keratinocytes were not available in the laboratory.

In order to avoid any contamination in the device, the chip was cleaned with 10% bleach since this was a common routine in INL labs. However, bleach chip sterilization is not supported in the literature. Taking that into consideration and with afraid that residuals of bleach could stay in the system and kill cells, an alternative method was employed in the next experiments. The devices were cleaned with ethanol with subsequent sterilization with UV radiation for 30 min [86, 87, 88].

For this preliminary experiment, Caco-2, an immortalized cell line of human colorectal adenocarcinoma cells, was used as a model of the intestinal epithelial barrier, due to a lack of keratinocyte cells. Caco-2 cells were trypsinized and seeded at a cell density of $1x10^5$ cells/cm^2. Twenty-four hours later, a steady flow of DMEM culture media supplemented with 10% FBS and antibiotics was driven by the syringe pump at a flow rate of 120 µL/h and stopped 14 days after. Every three days the culture media of the upper chamber was modified. The microfluidic system was maintained at 37 °C in a humidified incubator with 5% CO_2.

On days 6, 10, and 13, TEER measurements were done (**Figure 26**) and demonstrate an increase in values that indicates an increase in electrical resistance and, consequently, greater integrity and permeability of the monolayer over time.

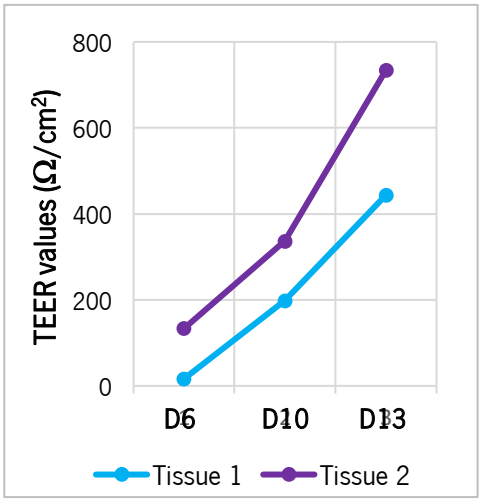

Figure 26 – Preliminary experiment TEER measurements on day 6, 10 and 13.

To conclude, an immunocytochemistry study was realized. The confocal microscopy images obtained are shown in **Figure 27**.

The actin filaments are marked in red, the tight junctions in green, and in blue the nucleus of the cells. Results demonstrated an improved confluence of the cells, demonstrating that the fluidic conditions improved their growth and the establishment of tight junctions that has the goal of sealing intercellular space, giving rise to a paracellular barrier as well as a selective transport pathway.

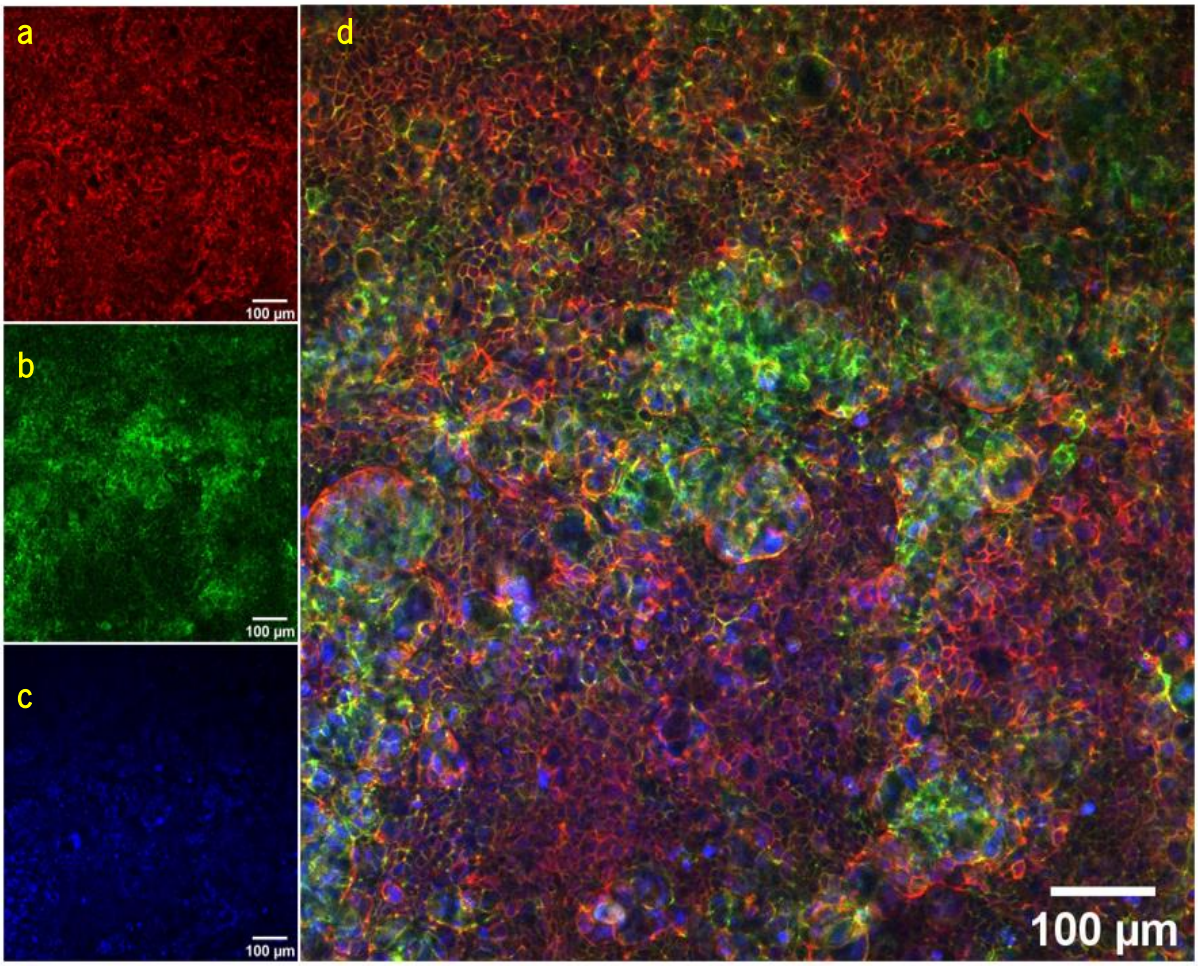

Figure 27 – Confocal images 100 X magnification of Caco-2 cell growth on the microfluidic device. (a) actin filaments (phalloidin-TRITC); (b) TJs (occludin monoclonal antibody AlexaFluor™ 488); (c) nucleus (DAPI); (d) images merge. Scale bars: 100 µm.

Based on these results it was verified that 14 days post-seeding are expected to establish a stable and confluent Caco-2 cell monolayer as reported in the literature [89, 90]. Furthermore, the stability and biocompatibility of the device constructed were proved.

3.3 Keratinocytes Cell Culture

3.3.1 HaCaT Cell Line

HaCaT is a nontumorigenic monoclonal immortalized keratinocytes cell line that have been widely employed to study epidermal homeostasis and pathophysiology. They are an immortal human keratinocyte line frequently used for skin keratinocytes *in-vitro* studies because of their highly preserved differentiation capacity. Schoop et al. demonstrate that HaCaT cells under improved organotypic culture conditions can reconstitute a normally structured squamous epithelium [91]. HaCaT is a cell model alternative to primary cells (that present high variability among donors) qualified for pharmacotoxicology as well nanotoxicology studies.

The HaCaT cell lines were maintained in high-glucose DMEM supplemented with 10% FSB and 1% pen-strep solution and were routinely subcultured when reached a confluence of 80-90%, showing a doubling time of 28 hours. As shown in **Figure 28** microscope images reveal the common morphology of keratinocytes that have a partially to fully differentiated phenotype due to the high calcium content of both standard medium and FBS. Phase contrast images showed the chronology of morphological changes of HaCaT cells that displayed a phenotype of polygonal cells and spread-out during culture.

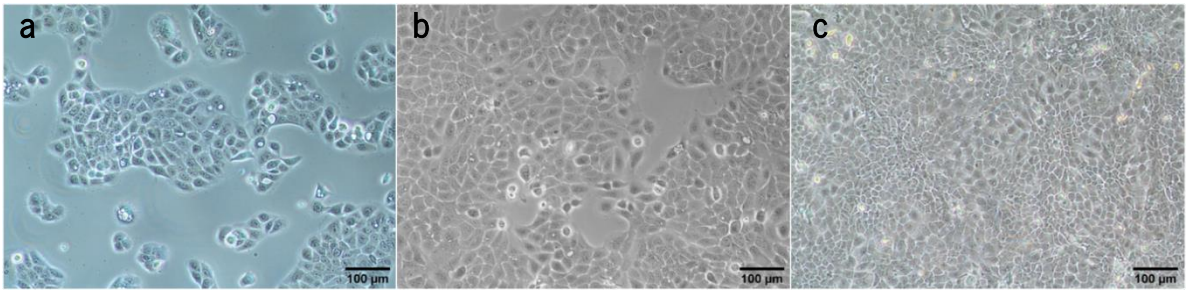

Figure 28 - Phase contrast images showing differentiation and proliferation after thawing HaCaT passage 32 on (a) day 2, (b) day 3, and (c) day 7 (10 X). Scale bars: 100 µm.

Presto Blue and Live and Dead assays reveal that cells are viable with a good morphology to proceed to 3D cultures (**Figure 29**). Sodium Dodecyl Sulfate (SDS) 5 % was used as a positive control. SDS is an anion surfactant with moderate toxicity toward keratinocytes *in-vitro*. It is recommended by the OECD and ICCVAM to be used as the reference (control) cytotoxic substance for *in-vitro* tests to assess the toxic effects of substances on skin and the reproducibility of the quantitative response of test systems, based on healthy human keratinocytes, to toxic exposure (test system validation) [92]. The viability of the cells was measured for 3h consecutively to understand what was the suitable time for this assay in this cell

culture type. No significant differences were observed among the monolayers for the same different time points and 5 % SDS demonstrated to be a good positive control.

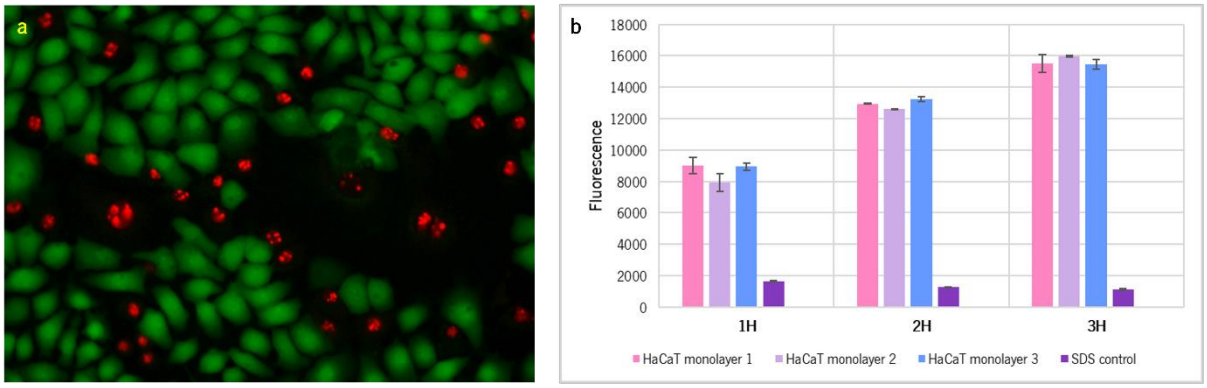

Figure 29 – (a) Fluorescence microscopic image of Live and Dead assay (20 X); (b) PrestoBlue cell viability plot.

3.3.2 Establishment of an Epidermis-On-a-Chip

HaCaT cell line from passage 36 was seeded at a cellular density of 4.46×10^5 cells/cm^2 into the chip with a 1 µm PET porous membrane previously coated with collagen IV. The flow rate of 1428 µL/h inducing a shear stress of 0.06 dyne/cm^2 was induced 48 h post-seeding. **Figure 30** represents the set-up that was created to grow the EoC. All the conditions were defined following literature in the field [93].

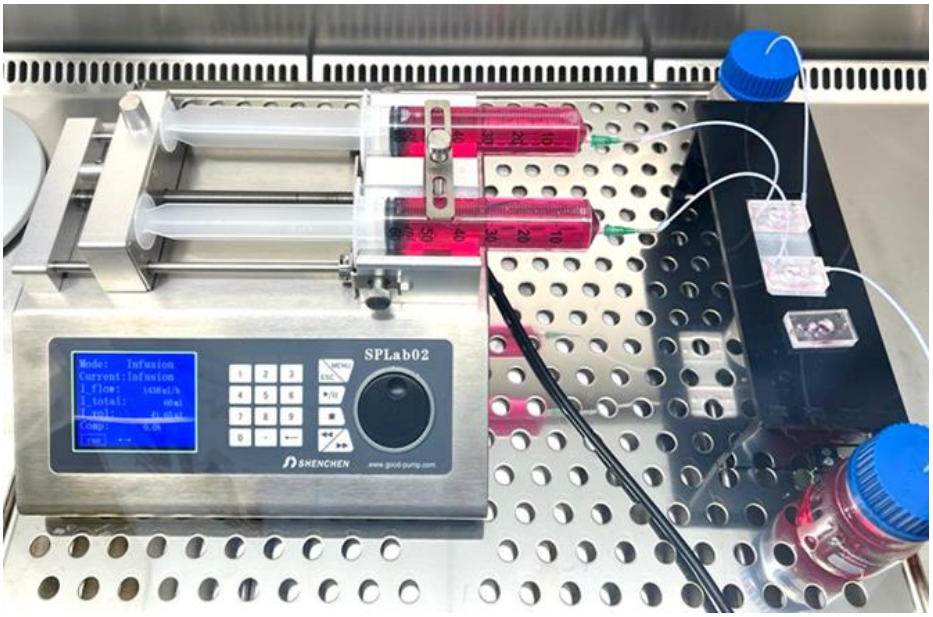

Figure 30 – Syringe pump-driven EoC set-up.

As can be seen, TEER values are low for this cell type (**Figure 31**), a result already confirmed by the literature [94]. TEER fluctuations were observed and related to the formation of bubbles in the system.

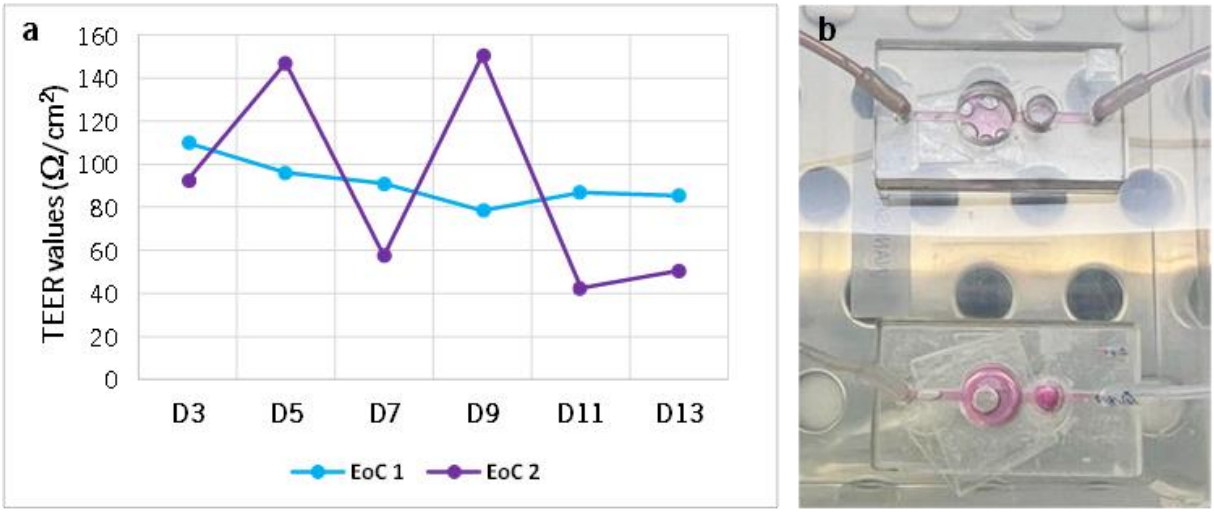

Figure 31 – (a) TEER measurements plot; (b) Bubbles in the EoC.

Although water could be successfully infused into the microchip as revealed by previous experiments, air bubbles were sometimes introduced into the chip when introducing the culture medium. Air bubbles can severely damage cells and are harmful to them. The presence of a single bubble can negatively increase the wall shear stress in a liquid-perfused microchannel, affecting the biological function and viability of the cells and is full elimination was particularly challenging [89]. To avoid this problem, a bubble trap (Darwin microfluidics) approach was implemented in the devices, and the medium used was previously degassed in Nalgene™ vacuum chamber (Thermo Scientific) in the following experiments.

Vacuum degassing can remove more than 95% of the dissolved gas. In turn, the principle of the bubble trap is based on the interaction of two forces, which are exerted on the air bubbles. These two forces are the hydrodynamic force induced by the fluid flow and the surface tension force induced by the trap walls. When fluid steam with gas bubbles flows through the trap, the bubbles are expelled through the hydrophobic air-permeable membrane, while it keeps the aqueous liquid inside the flow chamber without any leak [95].

Viability results from the PrestoBlue™ assay confirm that cells were viable, however, the low signal indicates that few cells were in the chip (**Figure 32.a**). Histological observations confirm that bubble formation limits the formation of a continuous barrier layer (**Figure 32.b**).

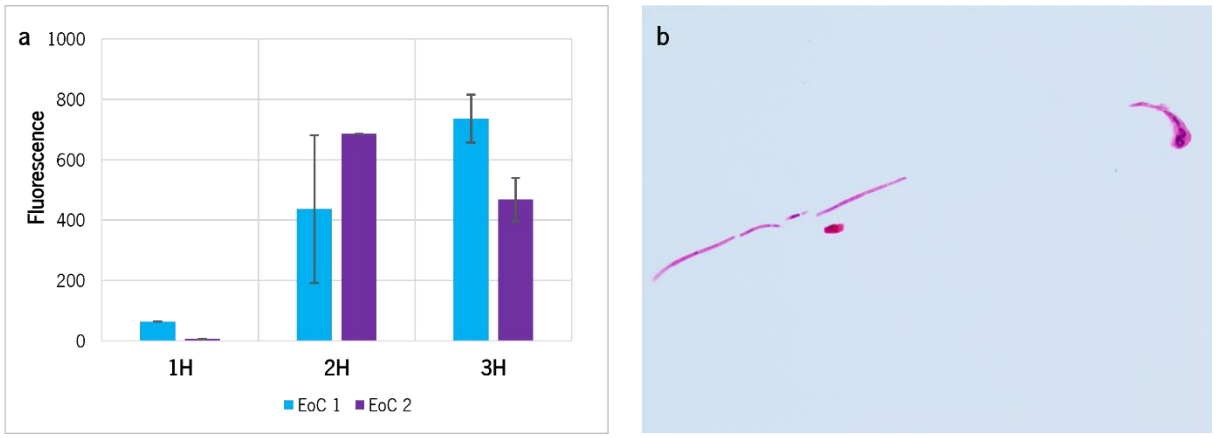

Figure 32 - (a) PrestoBlue™ cell viability plot; (b) Histology of the EoC 1.

Besides the formation of the bubbles, the handling of the system in the incubator was quite difficult, which request the development of support to hold several chips simultaneously. **Figure 33** illustrates his design. The support holds 6 microfluidic devices and the top is detachable to allow for microscopic visualization. The support was also fabricated by laser cutting.[3]

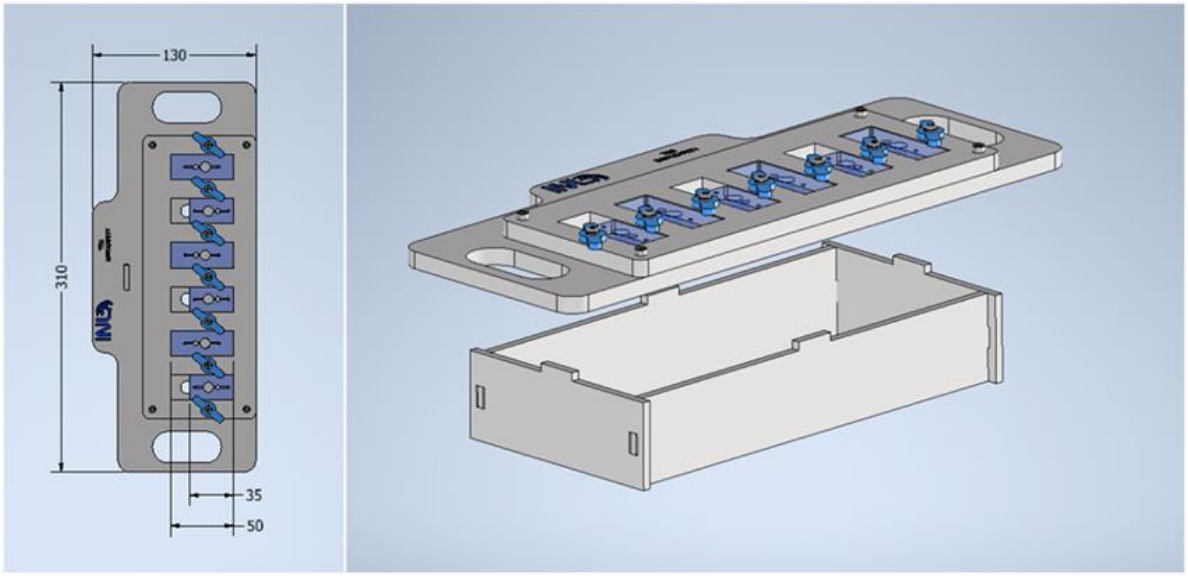

Figure 33 – Design of the support for EoC devices.

Always as a control, the epidermis was reconstructed in Transwell® inserts that are considered as static mode. HaCaT cell line from passage 36 was seeded at a cellular density of 4.46x105 cells/cm^2 into Transwell® culture inserts after reaching a confluency of approximately 80% and lifted to the air-liquid interface 3 days post-seeding. The ALI step is crucial for the development of a stratified epidermal model as it allows terminal differentiation of the keratinocytes. The Transwell® inserts have a PET porous

[3] Collaboration with Marco Martins and Duarte Mota, Technology Engineering Group.

membrane of 1 µm. The tissue barrier integrity was further evaluated by measuring TEER every two days from day 3 and optical microscopy images were taken on days 1, 3, and 12 (**Figure 34**). As can be seen in the optical microscope images a confluent cell monolayer was obtained during the time.

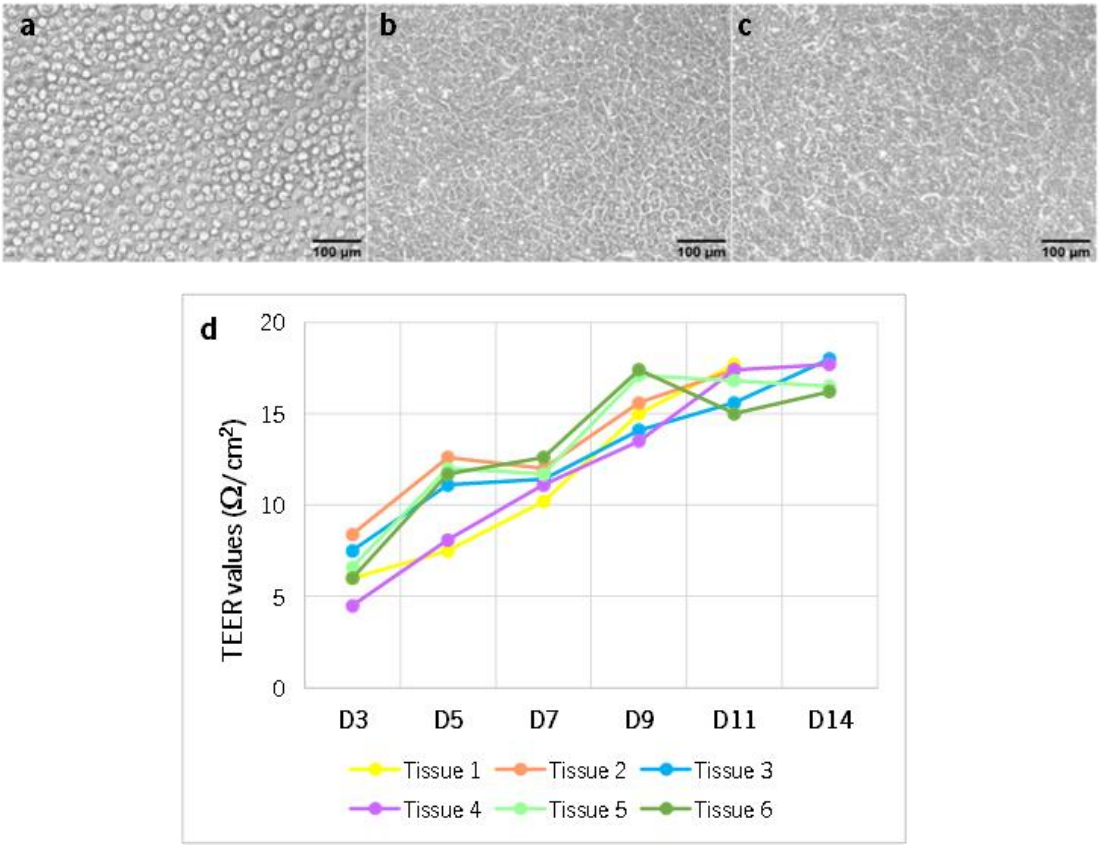

Figure 34 – Phase contrast images showing differentiation and proliferation on (a) day 1, (b) day 3, and (c) day 12. (10 X). Scale bars: 100 µm; (d) TEER measurements plot.

TEER measurements show a slight increase in values over time confirming that HaCaT cells were growing and forming a barrier as observed by phase contrast micrographs and as reported in the literature [94]. PrestoBlue™ cell viability assay confirms that cells are viable in the inserts, and the histological analysis shows an epidermis with around 3 layers of cells (**Figure 35**). No significant different variability was observed among the different tissues. From the inside to the outside, the epidermal layers start from the viable epidermis, i.e., the SB, the SS, and the SG, to the non-viable uppermost layer, i.e., the SC. The morphology of the epidermis was analyzed using H&E staining where a slight cornification process was observed.

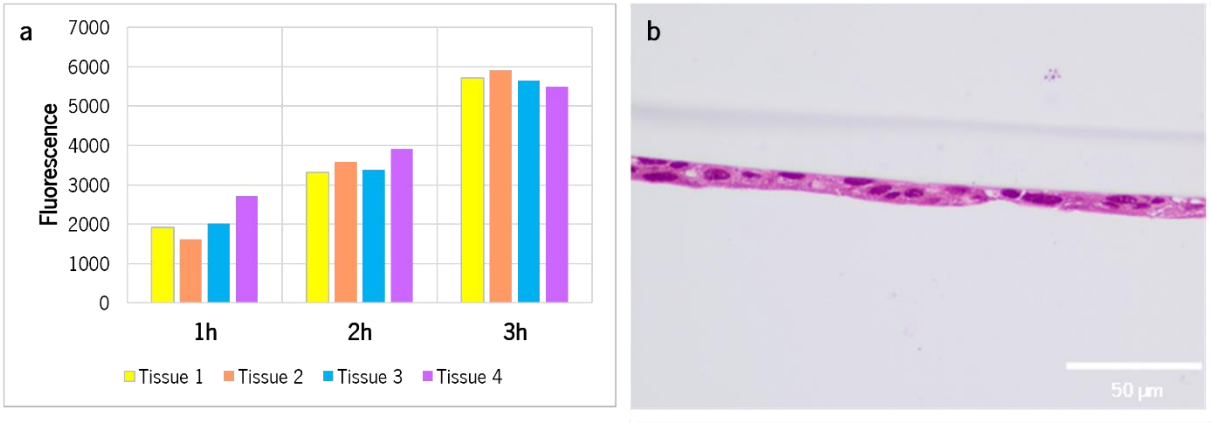

Figure 35 – a) PrestoBlue™ cell viability plot; (b) Histology of the tissue 3.

From the literature, it is known that in the SB layer, the cells have a columnar shape. From the second layer on towards the upper layers of the model, keratinocytes differentiate changing their cell morphology. They pass from a columnar shape in the SB layer, towards a spinous shape in the SS layer. In the SG layer, the cells have a more flattened shape and display keratohyalin granules that are represented as purple dots in the cytoplasm [96].

To visualize the TJs, the actin filaments and the nucleus of the cells, as well as the expression of K10 and K14, immunocytochemistry analyses were done (**Figure 36**).

Well-organized and well-distributed cytoskeletal structures were observed with HaCaT exhibiting a greater amount of condensed actin bundles, and the actin fibers tended to accumulate at the peripheral side near the plasma membrane as already demonstrated in the literature [97].

Confocal microscopy verified the key proteins' expression and distribution in accordance with the immunofluorescence staining. Agreeing with the images, occludin monoclonal antibody AlexaFluor™ 488 did not mark the TJs, which may be related to errors in the staining procedure. On the other hand, cytokeratin 10 and 14 were significantly expressed in the tissues. Physiologically, the expression of K14 is restricted to the epidermal basal layer, while the presence of K10 and involucrin indicates a more differentiated phenotype [98]. Basal K14 and differentiation related K10 staining characterized the presence of basal and spinous layers, respectively [99].

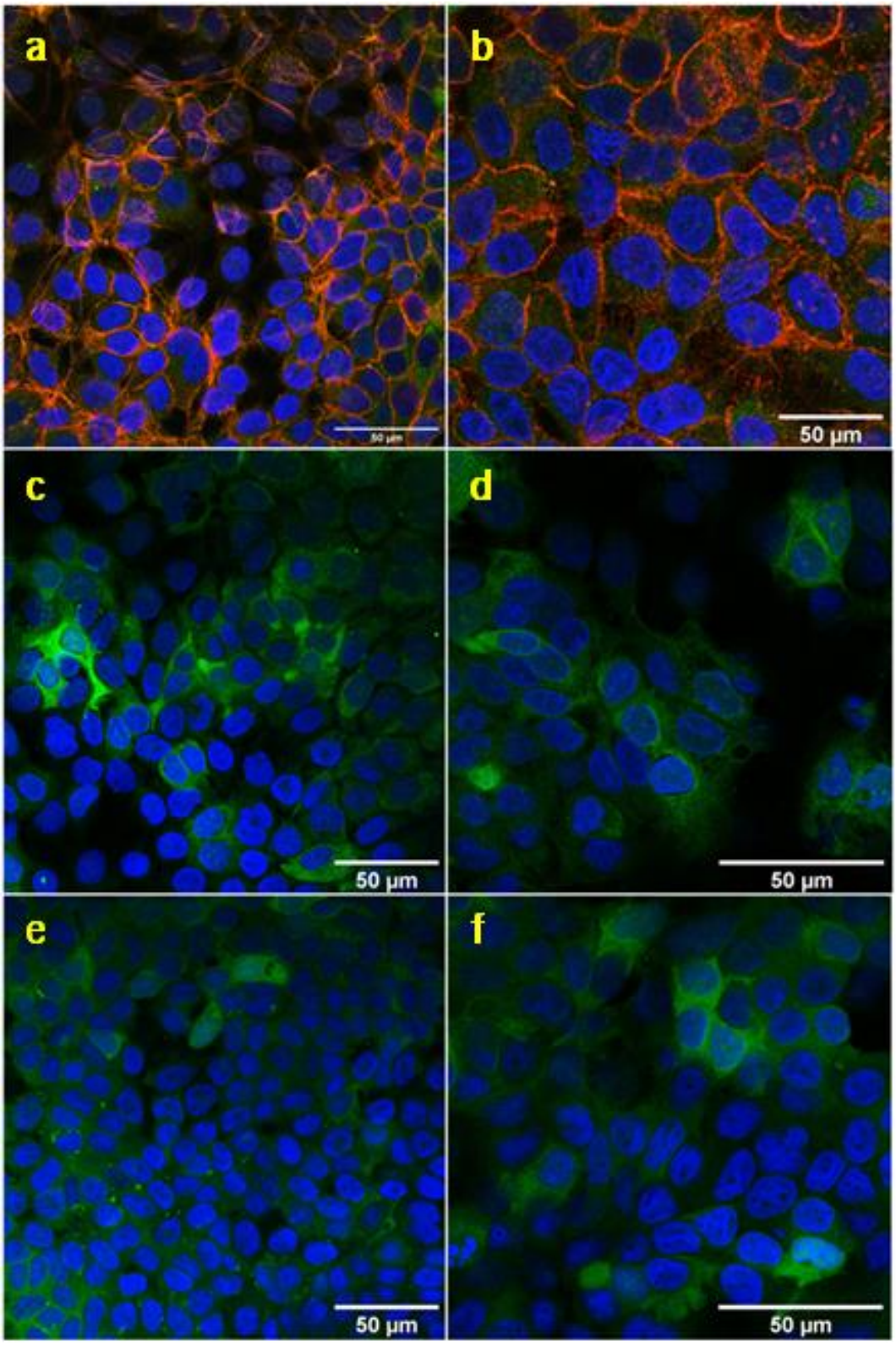

Figure 36 - Confocal images. (a) and (b) actin filaments, TJs and nucleus staining; (c) and (d) cytokeratin 10 and nucleus; (e) and (f) cytokeratin 14 and nucleus (400 X and 630 X magnification, respectively, for each set). Scale bars: 50 µm.

3.3.3 Establishing Cell Number and Pore Size for Epidermis-On-a-Chip Construction

As the first EoC results were not promising and, in some inserts, there was the observation of medium culture in the apical side, a new set of experiments testing the pore size of the membrane and cell density was performed. Two different seeding concentrations were tested, and the integrity and viability was compared. HaCaT cell line from passage 42 was seeded at two different cellular densities, $2.23x10^5$ cells/cm^2 and $4.46x10^5$ cells/cm^2, on Transwell® inserts with different PET porous membrane porosity, 0.4 µm and 1 µm.

Optical microscopy images and TEER measurements were done every 2 days after starting the air exposure (**Figure 37-40**). Two cellular densities were chosen since Dijkhoff et al. have demonstrated a sufficient cell number is needed to ensure that the medium from the basolateral compartment does not diffuse to the apical compartment. An insufficient seeding density (i.e., < 2.5x105 cells/cm2) can result in an inability to form a proper barrier, which is indicated by the diffusion of medium from the basolateral to the apical compartment, resulting in submerged instead of ALI culture conditions [96].

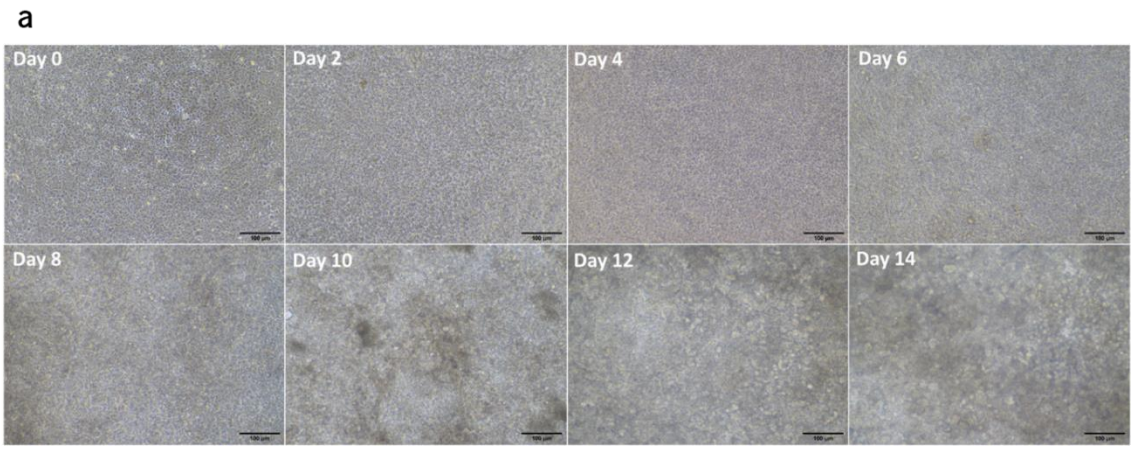

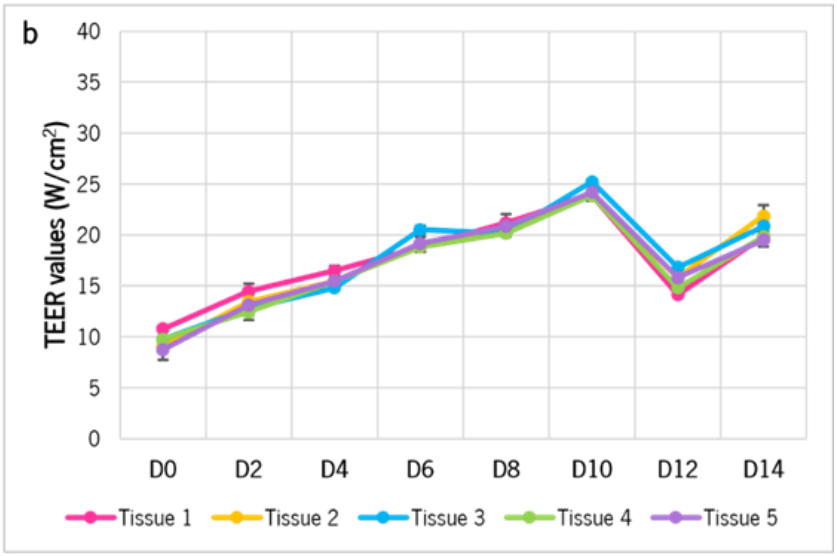

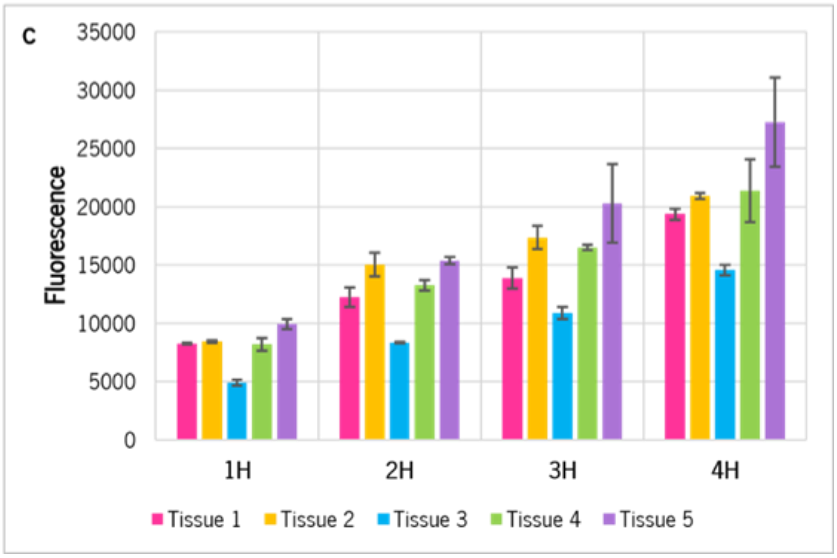

Figure 37 – PET membrane with 0.4 µm pore size, and cell density of 2.23x10^5 cells/cm^2 results. (a) Phase contrast images from day 0 to 14; (b) TEER measurements plot; (c) PrestoBlue™ cell viability plot.

It is possible to observe that this cell line has low values of TEER for all the conditions tested a result confirmed by the literature [94]. However, over time, it is possible to observe a slight increase in TEER values demonstrating that a barrier layer is forming. Results that once again corroborate with morphological analysis.

The results of the TEER measurements are similar for the different cell densities and pore sizes, showing an increase from day 0 to 10, and after a decline. This decline in TEER may be related to the reduction of humidity in the incubator from that day onward. Reduction of humidity was employed since the literature demonstrated that a decrease in the humidity on the incubator for the last three days of tissue formation promote the differentiation as well as improves subcutaneous hydration and tissue permeability properties [100].

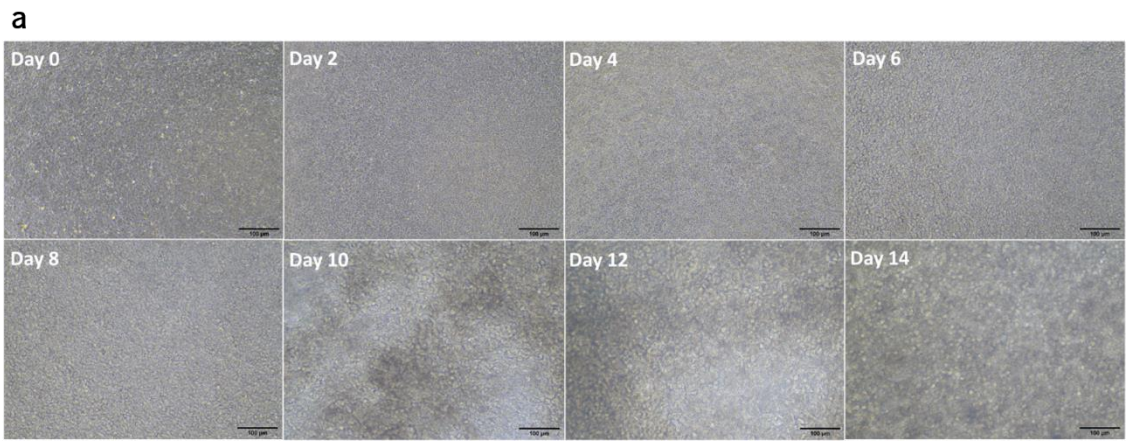

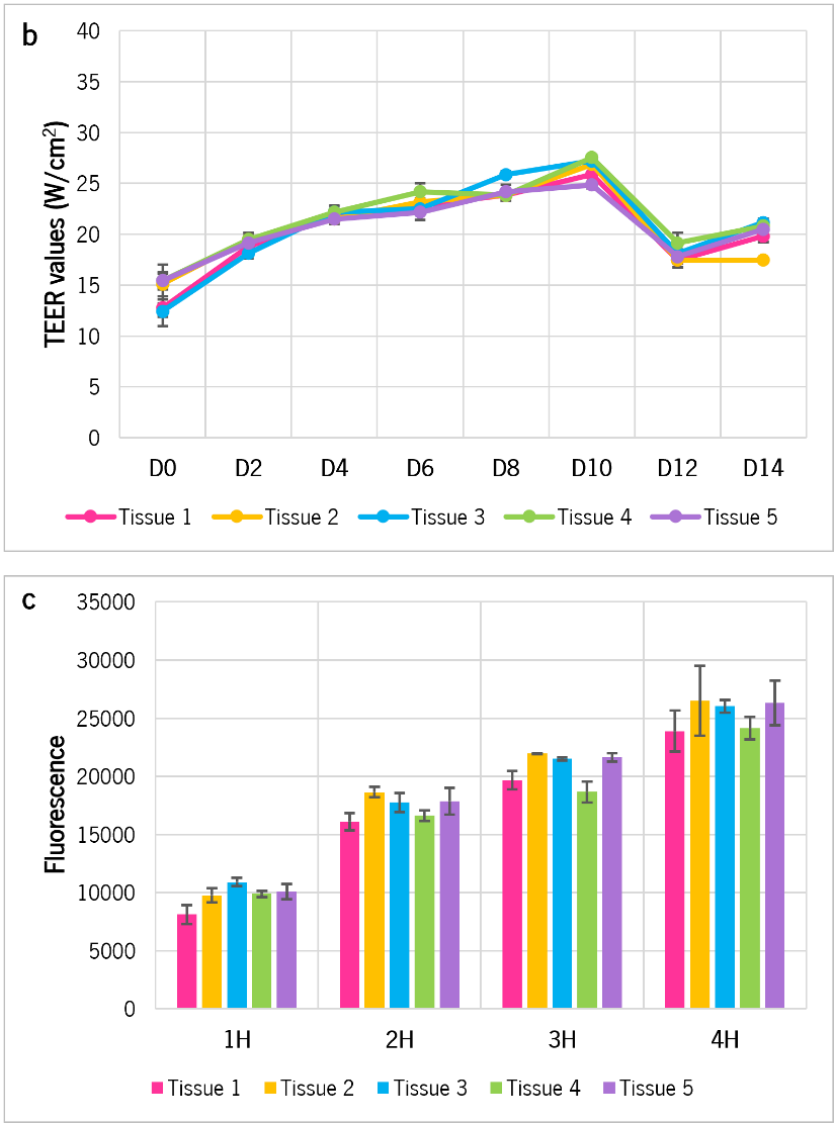

Figure 38 – PET membrane with 0.4 µm pore size, and cell density of 4.46x10^{5} cells/cm^{2} results. (a) Phase contrast images from day 0 to 14; (b) TEER measurements plot; (c) PrestoBlue™ cell viability plot.

Comparing Transwell® pore size diameter, it was possible to observe by contrast images analysis that a more robust epidermis was obtained for higher cell concentration.

In some 1 µm PET membrane porosity Transwell®, the medium was observed in the apical compartment upon establishment of ALI for tissues with lower cell numbers, confirming that this pore size is not sufficient to establish a proper barrier with this cell number.

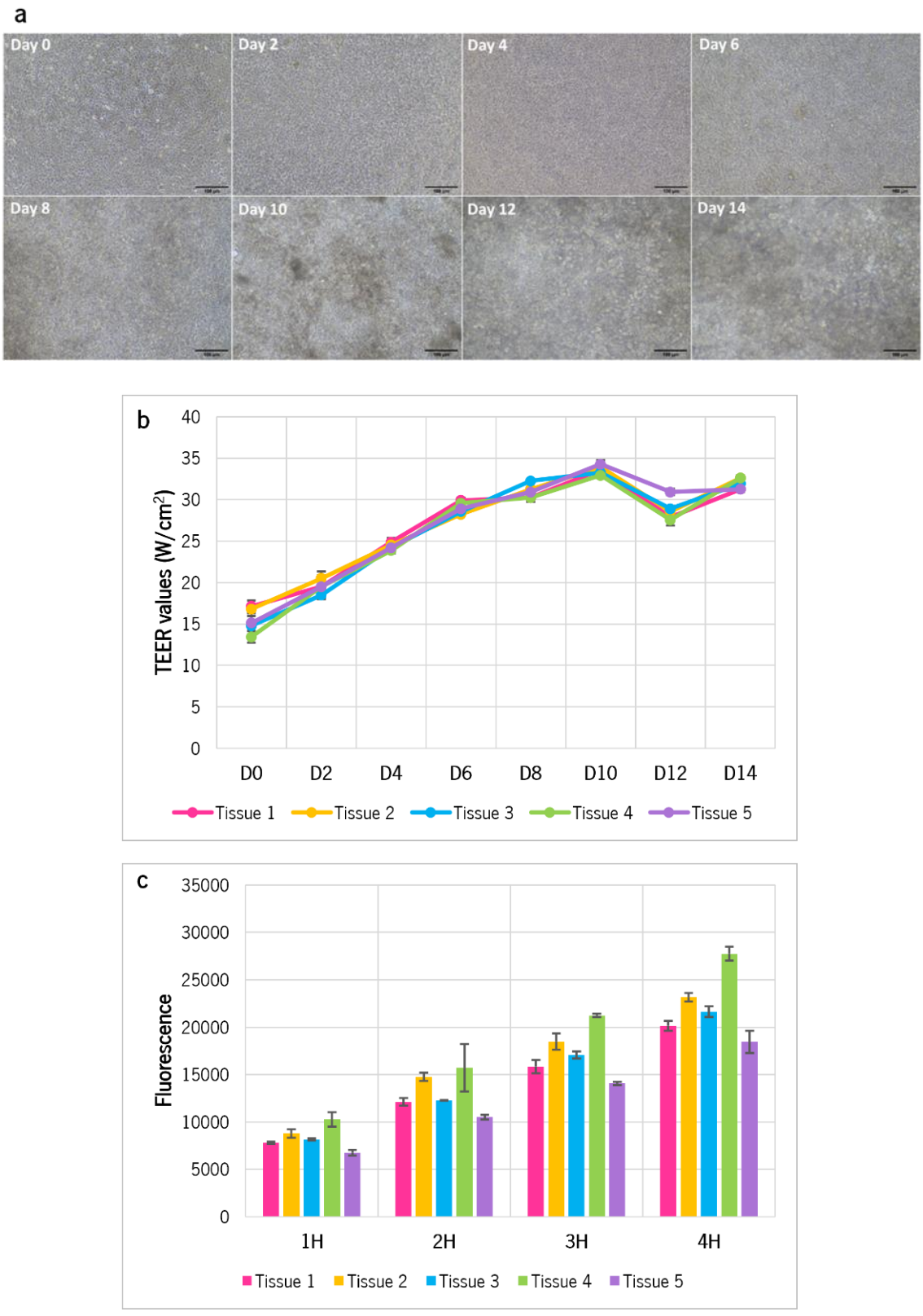

Figure 39 – PET membrane with 1 µm pore size, and cell density of 2.23x10^5 cells/cm^2 results. (a) Phase contrast images from day 0 to 14; (b) TEER measurements plot; (c) PrestoBlue™ cell viability plot.

No significant differences were observed in tissue viability however it is important to stress that during manipulation and even in some TEER measurements tissues disintegrate. Taking that in consideration in

the following experiments just in two chips and transwell TEER measurements were performed in order to avoid disturbance in the growth of the epidermis.

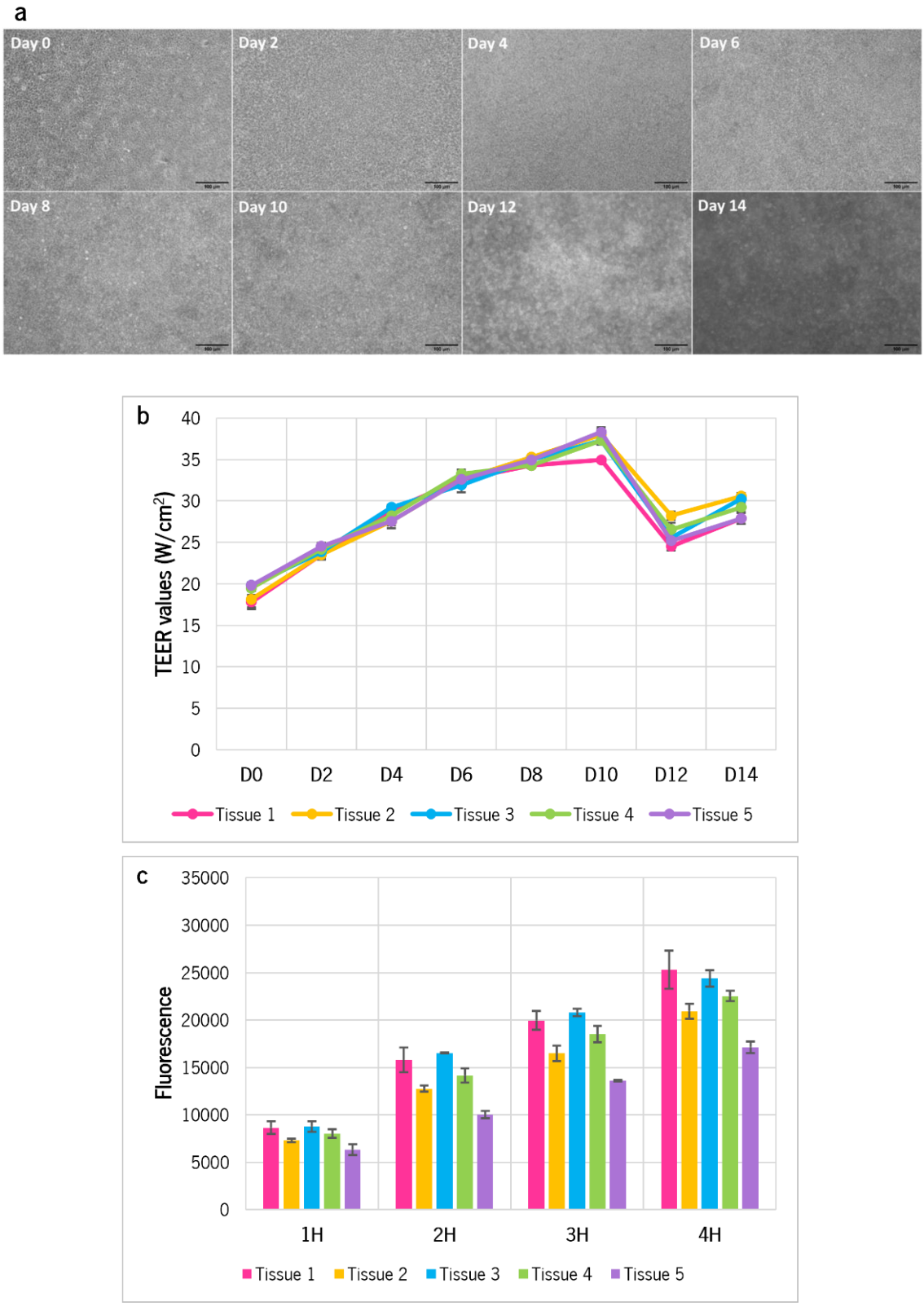

Figure 40 – PET membrane with 1 µm pore size, and cell density of 4.46x10^5 cells/cm^{2}results. (a) Phase contrast images from day 0 to 14; (b) TEER measurements plot; (c) PrestoBlue™ cell viability plot.

Resuming, results demonstrate that epidermis formation in Transwell® occurs better for the 0.4 μm size of the PET porous membrane and higher cell density. Taking that into consideration in the next experiments this pore size and cell density were maintained.

Also, some papers have presented 3D models performed with HaCaT cells and demonstrated their suitability for constituting epidermal tissue. However, this cell line is not commonly employed in 3D cultures due to its deficiency in generating a proper corneum layer, lacking an ordered structure and regular keratinization. Nonetheless, this deficiency is not permanent, and differential functions can be rescued by cultivation with specific growth factors. Taking that into consideration a new medium was selected to cultivate HaCaT – DMEM:HAM-F12 medium (3:1), supplemented with cholera toxin 2 ng/mL, apo-Transferrin 5 μg/mL, hydrocortisone 0.4 μg/mL, EgF 1 ng/mL, TGF 2 ng/mL, insulin 5 μg/mL, and 5% of fibroblast (Hs27 cell line)-cultured medium [99].

Font et al. showed that DMEM:HAM-F12 medium use on cell culture provides better cell differentiation, revealing a simplified reconstructed epidermis whose architecture is similar to the *in-vivo* epidermis [101]. Cholera toxin further enhances the growth of cells. The cells grew more rapidly and achieved higher saturation densities [102, 103]. Apo-transferrin and insulin stimulate cell multiplication, TGF-β play important roles in the growth and development of cell culture, and EGF promotes proliferation and decreases cellular apoptosis [104, 105]. In turn, hydrocortisone is a potent stimulator for the formation of barrier properties [106]. Fibroblasts in cultured medium secrete growth factors and extracellular matrices (in soluble form) molecules, which serve as natural, efficacious healing ingredients that enhance the keratinocyte expansion [107].

3.3.4 Effect of Differentiation Culture Medium and Membrane Pore Size on the Epidermis-On-a-Chip

In order to test the effect of the differentiation culture medium and membrane pore size on the EoC, a new set of experiments was made. The developed support and the bubble traps were also implemented in these experiments. HaCaT cell line from passages 46 to 51 was seeded at 4.46×10^5 cells/cm^2 into the chip with a 0.4 μm PET porous membrane previously coated with collagen IV. The differentiation culture medium was prepared and degasified. Then, a flow rate of 60 μL/h was induced 48 h post-seeding. **Figure 41** represents the set-up that was created to grow the EoC, and the set of results from three independent experiments is presented below.

Figure 41 – Syringe pump-driven EoC set-up including bubble traps and the new support developed.

Optical microscopy images and TEER measurements were made every 2 days after starting the air exposure. From the phase contrast images taken, it is possible to observe the formation of a thicker tissue from day 4 onwards, compared to the test without the use of a differentiation medium, which only occurred from day 10 (**Figure 42.a**). Furthermore, it is possible to visualize the formation of the tissue on the chip with the naked eye from day 10 (**Figure 42.b**).

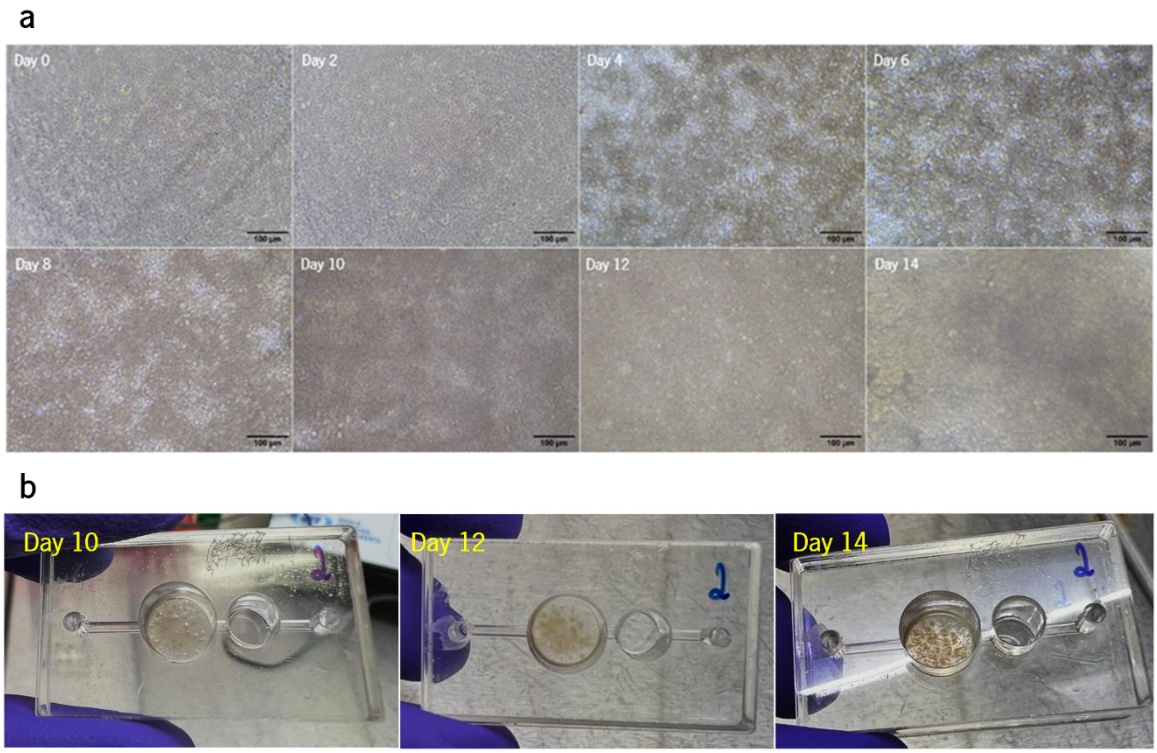

Figure 42 – Effect of the differentiation culture medium on the EoC. (a) Phase contrast images from day 0 to 14; (b) Tissue formation.

TEER measurements exhibit an increase in values over time, recording values between 438 and 536 Ω/cm^2, confirming that HaCaT cells were growing and forming a barrier (**Figure 43.a**). As reported, the OECD test guideline 430 requires TEER values over 500 Ω/cm^2 of skin models for use in permeation studies of chemical compounds [108].

The difference in TEER values between the Transwell inserts and the EoC can be explained by the conductance in the microfluidic channels. An equal current density over the entire membrane is normally required to conduct Transwell TEER experiments properly. In any case, the bulk liquid in Transwell devices ensures an approximately uniform potential drop throughout the entire membrane due to the conductivity of the culture medium. This is clearly not always the case in microfluidic chips because the conductivity in microfluidic channels is often many orders of magnitude less than in the bulk. As a result, only part of the membrane is conducting current, therefore the apparent TEER in these chip systems will be higher than in a Transwell system with the same membrane area [109].

In addition, it was observed that the application of bubble traps prevented the formation of bubbles in the system, improving tissue formation (**Figure 43**).

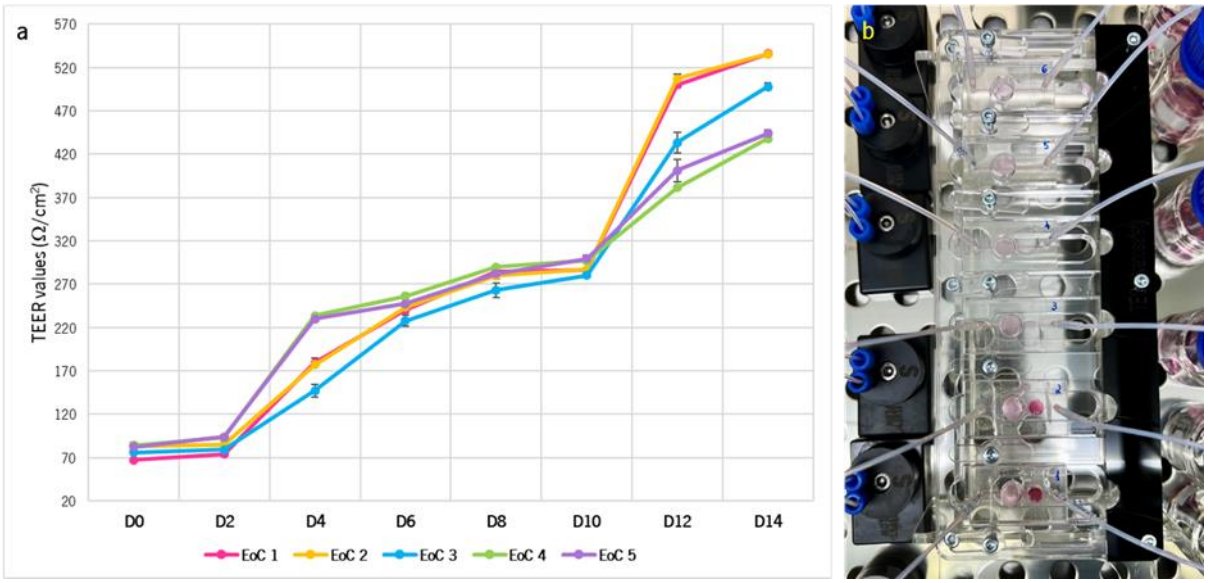

Figure 43 – Effect of the differentiation culture medium on the EoC. (a) TEER measurements plot; (b) Incorporation of bubble traps preventing the formation of bubbles in the EoC.

Viability results from the PrestoBlue™ assay confirm that cells were viable (**Figure 44**). No considerable variability was observed among the different tissues.

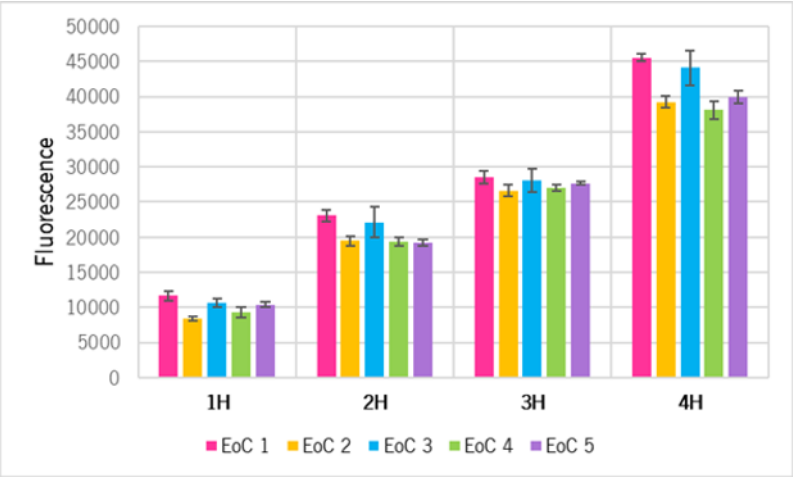

Figure 44 – Effect of the differentiation culture medium on the EoC: PrestoBlue™ cell viability plot.

Moreover, the differentiation and maturation of epidermal cells into a stratified epithelium were confirmed by cell morphology and biomarkers expression (**Figure 45**). The histological evaluation of EoC – H&E – clearly showed epidermal stratification, i.e. basal, spinous and corneum layers, indicating proper tissue growth and differentiation. The presence of the basal and spinous layers was demonstrated by the expression of K14 and K10, respectively. Also, we observed the presence of the stratum corneum indicated by the presence of brown-stained loricrin, respectively. Loricrin is a terminally differentiating structural protein comprising more than 70% of the cornified envelope. It contributes to the protective barrier function of the stratum corneum [110].

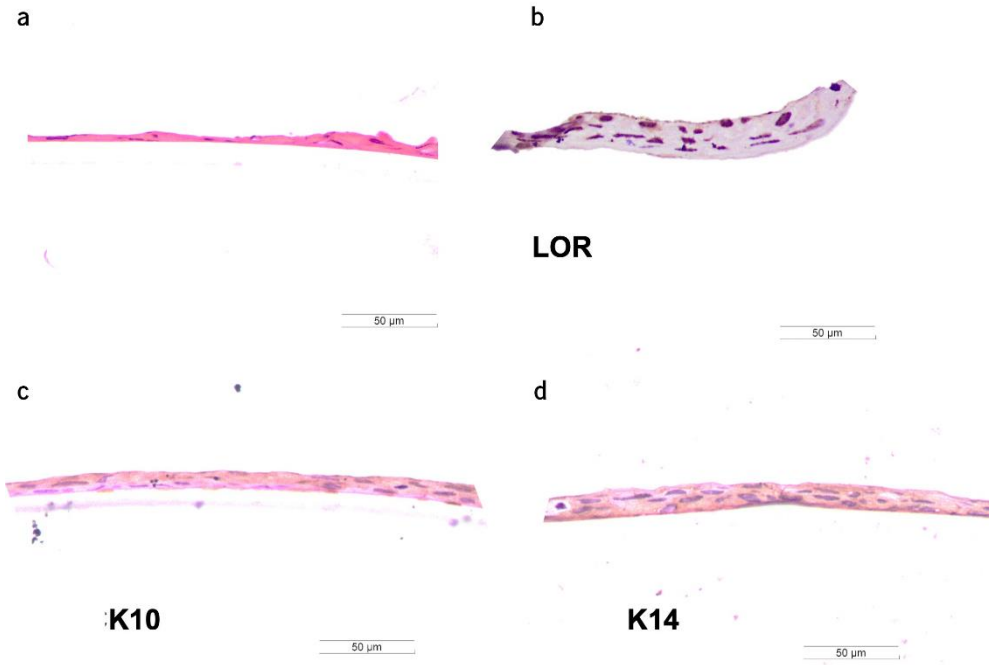

Figure 45 – Cell morphology and biomarkers expression: (a) H&E staining; (b), (c) and (d) Loricrin, keratin 10, and keratin 14 expression, respectively. Scale bars: 50 µm.

The detection of K14 and K10 characterized the presence of basal and spinous layers, respectively. These data are in contrast to the work from Boelsma et al. that showed the incapacity of HaCaT cells to differentiate [111].

In turn, cytoskeletal structures were observed by immunocytochemistry (**Figure 46**). The images exhibit a greater amount of condensed actin bundles at the peripheral side near the plasma membrane. By observation in the confocal microscope, it was also possible to verify the formation of tissue with an increased thickness compared with previous experiements.

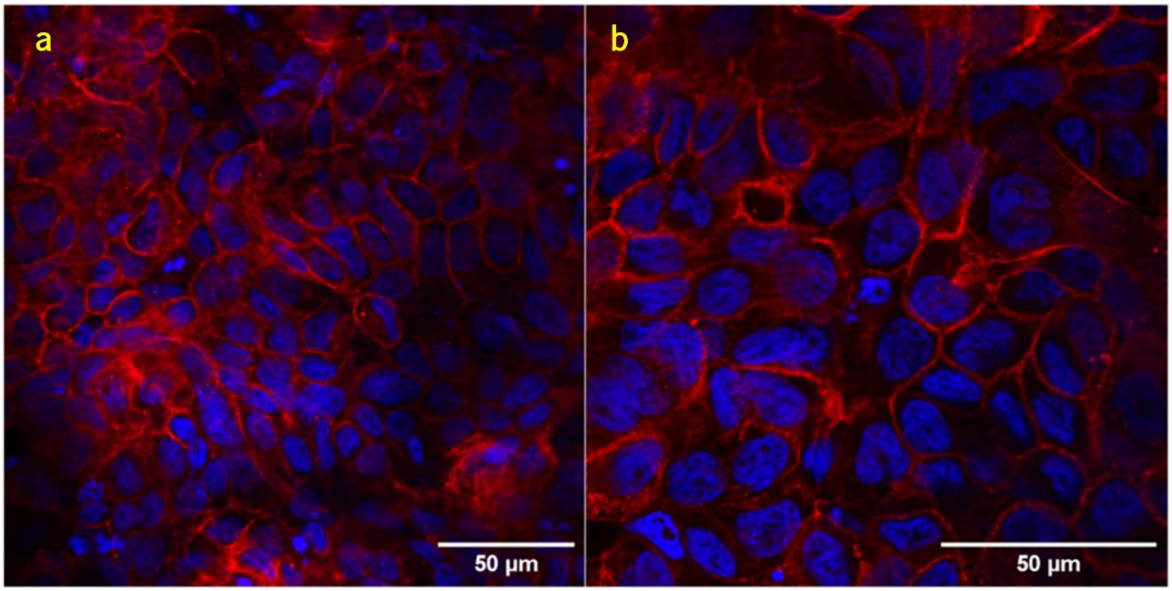

Figure 46 – Confocal images: actin filaments and nucleus staining. (a) 400 X magnification; (b) 630 X magnification. Scale bars: 50 µm.

As a control, the epidermis was reconstructed in parallel in Transwell® inserts. **Figure 47** shows the TEER measurements and optical microscopy images taken every two days from day 0 at ALI.

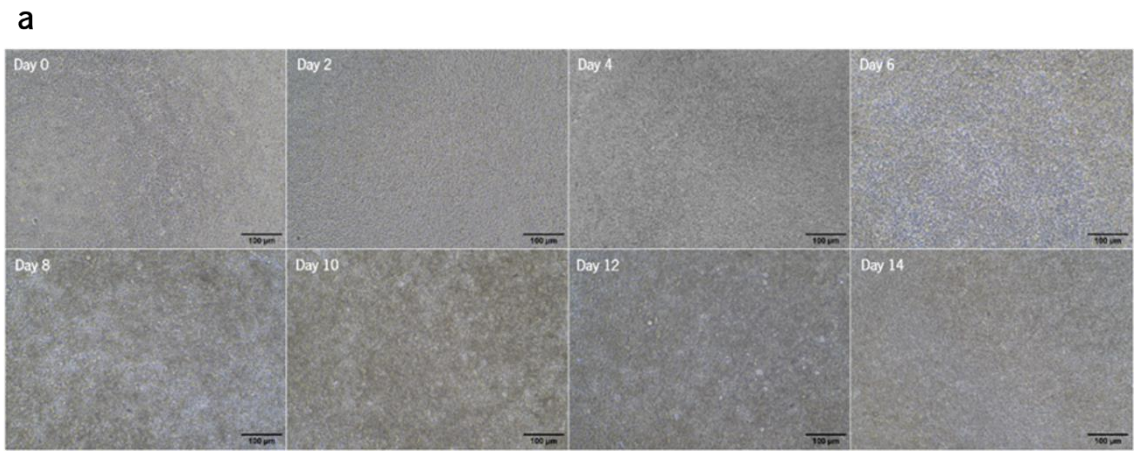

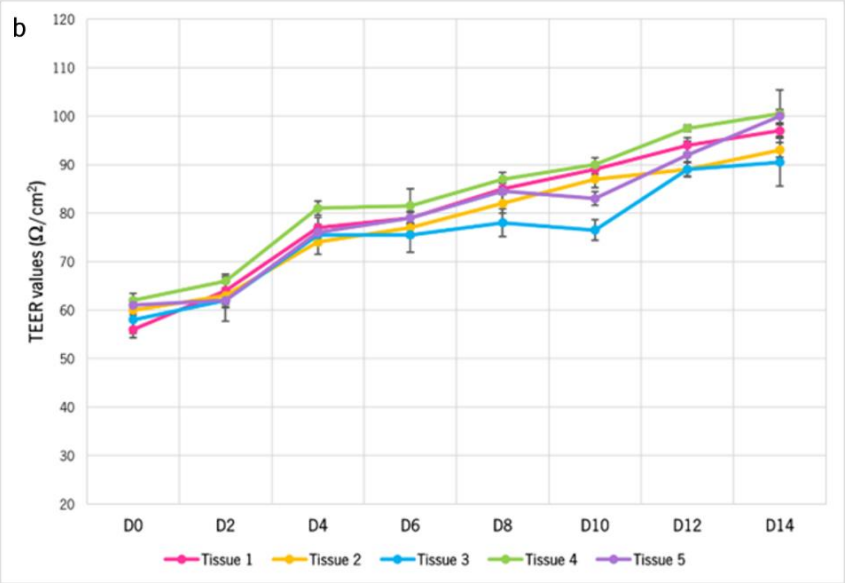

Figure 47 - Effect of the differentiation culture medium on the Transwell inserts. (a) Phase contrast images from day 0 to 14; (b) TEER measurements plot.

Microscopic observations demonstrate that tissue forms more slowly than in EoC, with day 8 probably corresponding to day 4 on the chip. This faster growth is already known to be related to fluid flow that is known to improve the nutrition supply, cellular crosstalk as well as provide physical stimuli to the cells [112]. Furthermore, TEER measurements reveal an increase in values over time greater than in Transwell inserts without differentiation culture medium proving that the use of this differentiation culture medium improves the HaCaT cells' growi and formation of a barrier.

Additionally, the PrestoBlue™ cell viability assay confirms that cells are viable in the inserts (**Figure 48**). No significant differences were observed among the inserts for the same different time points measured.

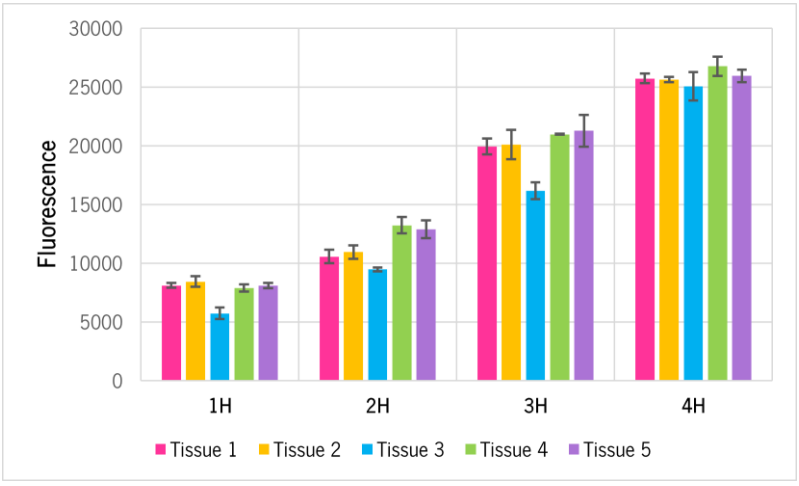

Figure 48 – Effect of the differentiation culture medium on the Transwell inserts: PrestoBlue™ cell viability plot.

Histological results (**Figure 49**) confirmed the presence of a brown stain for K14 confirming the presence of the epidermis basal layer. Cytokeratin 10 was not observed and loricrin was sightly marked revealing that a cornified layer was not observed in some points of the tissue. New histological experiments are underway to confirm these results and improve histological images.

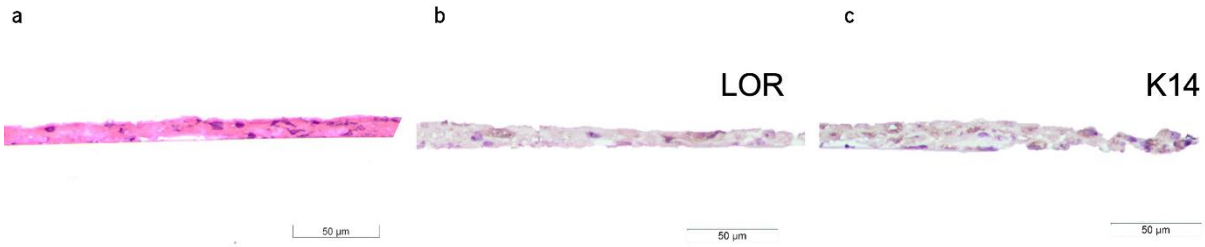

Figure 49 – Cell morphology and biomarkers expression: (a) H&E staining; (b) and (c) Loricrin and keratin 14 expression, respectively. Scale bars: 50 µm.

3.3.5 Effect of TiO_2 Nanoparticles on Epidermis-On-a-Chip Viability

At the end of the EoC formation, the tissues can be exposed to various stressors such as NMs to induce for example oxidative stress or inflammation. During the exposure, tissues are usually maintained in submerged medium starting from ALI D14.

To test the effect of TiO_2 NPs on EoC viability, rutile-TiO_2 NPs were dispersed in Milli-Q water at the concentration of 0.5 mg/mL with an energy of 1.15x104 KJ/m3 for 30 min in pulsed mode. Upon 24h stabilization, 100 µg/mL of the dispersed stock solution was incubated with 0.6 mg/mL BSA and then complete medium culture. A 24 h exposure was carried out and the PrestoBlue™ viability assay was performed.

Figure 50.a demonstrate a slight decrease in viability on EoC with rutile-TiO_2 NPs exposure compared to an EoC without NPs exposure. However, it is not statistically significant. As a control, the same conditions were tested on the static inserts, and the same results were observed (**Figure 50.b**). Further studies must be carried out to investigate more realistically the effects of the exposure of rutile-TiO_2 NPs in the epidermis.

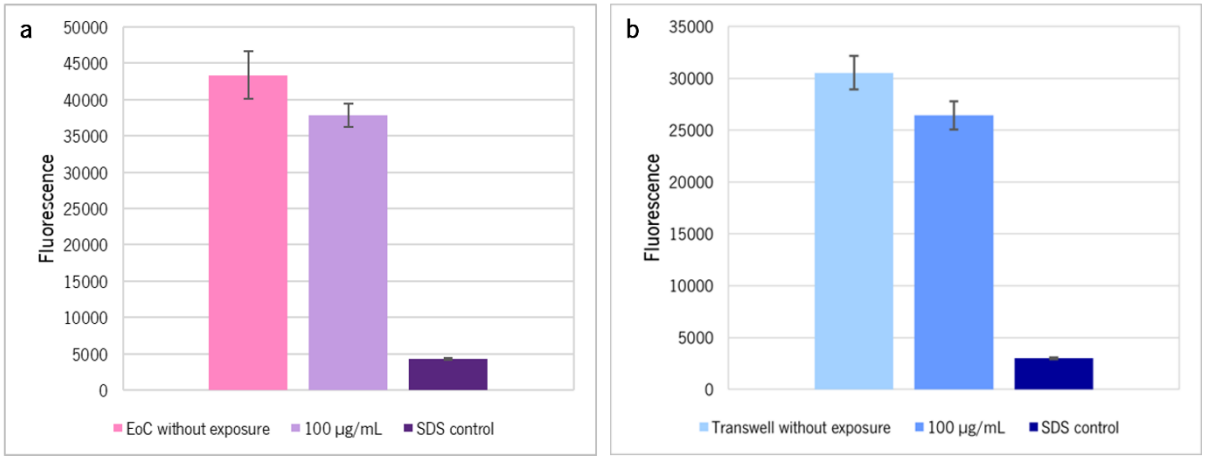

Figure 50 – Effect of TiO_2 NPs exposure on cells viability: (a) and (b) EoC and Transwell inserts, respectively.

CHAPTER 4

CONCLUSION AND FUTURE PERSPECTIVES

4.1 Conclusion

The main aim of this work was to develop and optimize the EoC system that recapitulates the *in-vivo* features of the epidermis.

Fluid dynamics reveal that in the constructed model the shear stress-induced is 0.06 dyne/cm^2, a value that is known to not affect keratinocytes viability. Medium degasification as well as bubble traps were employed in the EoC since air bubbles were impairing tissue formation. Keratinocytes were successfully introduced in the EoC and were able to grow and expand forming an epidermis layer.

TEER measurements, viability, histological and immunocytochemistry analysis demonstrate that a cell seeding of $4.46x10^5$ cells/cm^2 in the devices with a PET membrane of 0.4 µm pore size are the best conditions to establish a reliable epidermis-on-a-chip. The epidermis formed on EoC has TEER values according to the ones requested by OECD test guideline 430 and demonstrated the presence of an epidermal stratification indicating proper tissue growth and differentiation. The growth of the epidermis on the chip was faster compared to the transwell system possibly due to the perfusion of medium culture in the chip.

The exposure of rutile-TiO_2 NPs to the EoC reveals a slight reduction in epidermis viability however new experiments should be performed to confirm these results as well as understand if NPs were able to internalize the model.

4.2 Future Perspectives

To conclude, besides testing the toxicity of NPs, future work may entail the internalization of NPs on the model and observing its effect on cytokines production. Furthermore, understand and characterize the permeability of the EoC is necessary. The implementation of a fluidic microchannel on the top of the EoC for the exposure of NPs could also be employed for a more realistic dynamic of the system.

Ambitiously, a complex device must be constructed with the addition of fibroblast cells to mimic the dermal layer and create a full-thickness SoC model. Further developments in *in-vitro* skin substitutes should also include addition of skin appendages. The integration of sweat glands or hair follicles will help to mimic a more accurate *in-vivo* situation, offering a more correct experimental set-up.The development of biomimetic materials recapitulating the *in-vivo*-like ECM enhances the physiologically relevance of the

developed tissues. Finally, the creation of vascular networks could be possible with the emergence of new technologies such as OoC technology and bioprinting. Building the next generation of skin constructs by including various skin components and patient-specific cells, while optimizing miniaturization methods, could revolutionize the early stages of nanotoxicology studies and offer advanced tools for modelling skin diseases.

CHAPTER 5

REFERENCES

[1] R. A. Baan, "Carcinogenic Hazards from Inhaled Carbon Black, Titanium Dioxide, and Talc not Containing Asbestos or Asbestiform Fibers: Recent Evaluations by an IARC Monographs Working Group," *Inhalation Toxicology,* vol. 19, no. 1, pp. 213-228, 2007.

[2] P. L. Sanches, L. R. O. Geaquinto, R. Cruz, D. C. Schuck, M. Lourencini, J. M. Granjeiro and A. R. L. Ribeiro, "Toxicity Evaluation of TiO2 Nanoparticles on the 3D Skin Model: A Systematic Review," *Frontiers in Bioengineering and Biotechnology,* 2020.

[3] F. L. Filon , D. Bello, J. W. Cherrie, A. Sleeuwenkoek, S. Spaan and D. H. Brouwer, "Occupational dermal exposure to nanoparticles and nano-enabled products: Part I - Factors affecting skin absorption," *International Journal of Hygiene and Environmental Health,* vol. 219, no. 6, pp. 536-544, 2016.

[4] P. Erkekoglu, B. K. Giray and N. Basaran, "3R Principle and Alternative Toxicity Testing Methods," *Journal of Pharmaceutical Sciences,* vol. 36, pp. 101-117, 2011.

[5] J. Nriagu, Encyclopedia of Environmental Health, Elsevier, 2019.

[6] P. K. Nigam, "Adverse reactions to cosmetics and methods of testing," *Indian J Dermatol Venerol Leprol,* vol. 75, no. 1, pp. 10-19, 2009.

[7] S. F. Bezerra, B. S. Rodrigues, A. C. G. Silva, R. I. Ávila, H. R. G. Brito, E. R. Cintra, D. F. M. C. Veloso, E. M. Lima and M. C. Valadares, "Application of the adverse outcome pathway framework for investigating skin sensitization potential of nanomaterials using new approach methods," *Contact Dermatitis,* vol. 84, no. 2, pp. 67-74, 2020.

[8] T. A. Robertson, W. Y. Sanchez and M. S. Roberts, "Are Commercially Available Nanoparticles Safe When Applied to the Skin?," *Journal of Biomedical Nanotechnology,* vol. 6, no. 5, pp. 452-468, 2010.

[9] T. G. Smijs and S. Pavel, "Titanium dioxide and zinc oxide nanoparticles in sunscreens: focus on their safety and effectiveness," *Nanotechnology, Science and Applications,* vol. 4, pp. 95-112, 2011.

[10] H. Shi, R. Magaye, V. Castranova and J. Zhao, "Titanium dioxide nanoparticles: a review of current toxicological data," *Particle and Fibre Toxicology,* 2013.

[11] K. Schilling, B. Bradford, D. Castelli, E. Dufour, J. F. Nash, W. Pape, S. Schulte, I. Tooley, J. Van den Bosch and F. Schellauf, "Human safety review of “nano” titanium dioxide and zinc oxide," *Photochemical & Photobiological Sciences,* vol. 9, pp. 495-509, 2009.

[12] F. Knorr, A. Patzelt, M. C. Meinke, A. Vogt, U. Blume-Peytavi, E. Rühl and J. Lademann, "Chapter 13 - Interactions of Nanoparticles with Skin," in *Biological Responses to Nanoscale Particles*, Spinger, 2019, pp. 329-339.

[13] M. P. Vinardell and M. Mitjans, "Alternative Methods to Animal Testing for the Safety Evaluation of Cosmetic Ingredients: An Overview," *Cosmetics,* 2017.

[14] O. Díez-Sales, A. Nácher, M. Merino and V. Merino, "Chapter 17 - Alternative Methods to Animal Testing in Safety Evaluation of Cosmetic Products," in *Analysis of Cosmetics Products*, Elsevier, 2018, pp. 551-584.

[15] P. A. J. Kolarsick, M. A. Kolarsick and C. Goodwin, "Chapter 1 - Anatomy and Physiology of the Skin," in *Skin Cancer*, 2011, pp. 1-12.

[16] M. J. Randall, A. Jüngel, M. Rimann and K. Wuertz-Kozak, "Advances in the Biofabrication of 3D Skin in vitro: Healthy and Pathological Models," *Frontiers in Bioengineering and Biotechnology,* 2018.

[17] J. Kanitakis, "Anatomy, histology and immunohistochemistry of normal human skin," *European Journal of Dermatology,* vol. 12, no. 4, 2002.

[18] J. A. McGrath, R. A. J. Eady and F. M. Pope, "Chapter 3 - Anatomy and Organization of Human Skin," in *Rook's Textbook of Dermatology*, Blackwell, 2004.

[19] P. A. A. Zoio, *Full-thickness skin-o-a-chip model for in vitro drug testing,* Universidade Nova de Lisboa: Ph.D dissertation, November 2021.

[20] K. Pfisterer, L. E. Shaw, D. Symmank and W. Weninger, "The Extracellular Matrix in Skin Inflammation and Infection," *Frontiers in Cell and Developmental Biology,* 2021.

[21] H. Niehues, J. A. Bouwstra, A. Ghalbzouri, J. M. Brandner, P. L. J. M. Zeeuwen and E. H. van der Bogaard, "3D skin models for 3R research: The potential of 3D reconstructed skin models to study skin barrier function," *Experimental Dermatology,* vol. 27, no. 5, pp. 501-511, 2018.

[22] M. Wufuer, G. Lee, W. Hur, B. Jeon, B. J. Kim, T. H. Choi and S. Lee, "Skin-on-a-chip model simulating inflammation, edema and drug-based treatment," *Scientif Reports,* vol. 6, no. 37471, 2016.

[23] A. G. Niculescu, C. Chircov, A. C. Bîrcã and A. M. Grumezesco, "Fabrication and Applications of Microfluidic Devices: A Review," *International Journal of Molecular Sciences,* 2021.

[24] G. M. Whitesides, "The origins and the future of microfluidics," *Nature,* vol. 442, pp. 368-373, 2006.

[25] S. N. Bhatia and D. E. Ingber, "Microfluidic organs-on-chips," *Nature Biotechnology,* pp. 760-772, 2014.

[26] K. Ren, J. Zhou and K. Wu, "Materials for Microfluidic Chip Fabrication," *Accounts of Chemical Research,* vol. 46, no. 11, pp. 2396-2406, 2013.

[27] Q. Wu, J. Liu, X. Wang, L. Feng, J. Wu, X. Zhu, W. Wen and X. Gong, "Organ-on-a-chip: recent breakthroughs and future prospects," *BioMedical Engineering Online,* vol. 19, no. 9, 2020.

[28] J. D. Caplin, N. G. Granados, M. R. James, R. Montazami and N. Hashemi, "Microfluidic Organ-on-a-Chip Technology for Advancement of Drug Development and Toxicology," *Advanced Healthcare Materials,* 2015.

[29] J. Wu and M. Gu, "Microfluidic sensing: state of the art fabrication and detection techniques," *Journal of Biomedical Optics,* 2011.

[30] D. J. Beebe, G. A. Mensing and G. M. Walker, "Physics and Applications of Microfluidics in Biology," *Annual Review of Biomedical Engineering,* vol. 4, pp. 261-286, 2002.

[31] E. K. Sackmann, A. L. Fulton and D. J. Beebe, "The present and future role of microfluidics in biomedical research," *Nature,* vol. 507, pp. 181-189, 2014.

[32] Q. Wu, J. Liu, X. Wang, L. Feng, J. Wu, X. Zhu, W. Wen and X. Gong, "Organ-on-a-chip: recent breakthroughs and future prospects," *BioMedical Engineering OnLine,* vol. 19, no. 9, 2020.

[33] H. Avci, F. Dogan Güzel, S. Erol and A. Akpek, "Recent advances in organ-on-a-chip technologies and future challenges: a review," *Turkish Journal of Chemistry,* vol. 42, pp. 587-610, 2018.

[34] F. Lebre, N. Chatterjee, S. Costa, E. Fernández-de-Gortari, C. Lopes, J. Meneses, L. Ortiz, A. R. Ribeiro, V. Vilas-Boas and E. Alfaro-Moreno, "Nanosafety: An evolving Concept to Bring the safest Possible Nanomaterials to Society and Environment," *Nanomaterials,* vol. 12, no. 1810, 2022.

[35] N. Lin, X. Zhou, X. Geng, C. Drewell, J. Hübner, Z. Li, Y. Zhang, M. Xue, U. Marx and B. Li , "Repeated dose multi-drug testing using a microfluidic chip-based coculture of human liver and kidney proximal tubules equivalents," *Scientific Reports,* vol. 10, no. 8879, 2020.

[36] V. De Gregorio, M. Telesco, B. Corrado, V. Rosiello, F. Urciuolo, P. A. Netti and G. Imparato, "Intestine-Liver Axis On-Chip Reveals the Intestinal Protective Role on Hepatic Damage by Emulating Ethanol First-Pass Metabolism," *Frontiers in Bioengineering and Biotechnology,* vol. 8, no. 163, 2020.

[37] J. H. Sung, Y. I. Wang, N. N. Sriram, M. Jackson, C. Long, J. J. Hickman and M. L. Shuler, "Recent Advances in Body-on-a-Chip Systems," *Analytical Chemistry,* vol. 91, no. 1, pp. 330-351, 2019.

[38] N. Picollet-D'hahan, A. Zuchowska, I. Lemeunier and S. Le Gac, "Multiorgan-on-a-Chip: A Systemic Approach To Model and Decipher Inter-Organ Communication," *Trends in Biotechnology,* vol. 39, no. 8, pp. 788-810, 2021.

[39] C. Oleaga, C. Berbabini, A. S. T. Smith, B. Srinivasan, M. Jackson, W. McLamb, V. Platt, R. Bridges, Y. Cai, N. Santhanam, B. Berry, S. Najjar, N. Akanda, X. Guo, C. Martin, G. Ekman, M. B. Esch, J. Langer, G. Ouedraogo, J. Cotovio, L. Breton, M. L. Shuler and J. J. Hickman, "Multi-

Organ toxicity demonstration in a functional human in vitro system composed of four organs," *Scientific Reports,* vol. 6, no. 20030, 2016.

[40] J. Ponmozhi, S. Dhinakaran, Z. Varga-Medveczky, K. Fónagy, L. A. Bors, K. Iván and F. Erdõ, "Development of Skin-On-A-Chip Platforms for Different Utilizations: Factors to Be Considered," *Micromachines,* 2021.

[41] P. Zoio and A. Oliva, "Skin-on-a-Chip Technology: Microengineering Physiologically Relevant In Vitro Skin Models," *Pharmaceutics,* 2022.

[42] L. J. Van der Brock, L. I. J. C. Bergers, C. M. A. Reijnders and S. Gibbs, "Progress and Future Prospectives in Skin-on-Chip Development with Emphasis on the use of Different Cell Types and Technical Challenges," *Stem Cell Reviews and Reports,* vol. 13, pp. 418-429, 2017.

[43] I. Risueño, L. Valencia, J. L. Jorcano and D. Velasco, "Skin-on-a-chip models: General overview and future perspectives," *APL Bioengineering,* vol. 5, no. 3, 2021.

[44] Z. Zhang and B. B. Michniak-Kohn, "Tissue Engineered Human Skin Equivalents," *Pharmaceutics,* vol. 4, no. 1, pp. 26-41, 2012.

[45] T. Agarwal, G. H. Narayana and I. Banerjee, "Keratinocytes are mechanoresponsive to the microflow-induced shear stress," *Cytoskeleton,* vol. 76, no. 2, pp. 209-218, 2019.

[46] E. Tokuyama, Y. Nagai, K. Takahashi, Y. Kimata and K. Naruse, "Mechanical Stretch on Human Skin Equivalents Increases the Epidermal Thickness and Develops the Basement Membrane," *PLOS ONE,* 2015.

[47] B. Srinivasan, A. R. Kolli, M. B. Esch, H. E. Abaci, M. L. Shuler and J. J. Hickman, "TEER Measurement Techniques for In Vitro Barrier Model Systems," *Journal of Laboratory Automation,* vol. 20, no. 2, pp. 107-126, 2015.

[48] M. Odijk, A. D. Van der Meer, D. Levner, H. J. Kim, M. W. Van der Helm, L. I. Segerink, J.-P. Frimat, G. A. Hamilton, D. E. Ingber and A. Van der Berg, "Measuring direct current trans-epithelial electrical resistance in organ-on-a-chip microsystems," *Lab on a Chip,* vol. 15, no. 745, 2015.

[49] B. Ataç, I. Wagner, R. Horland, R. Lauster, U. Marx, A. G. Tonevitsky, R. P. Azar and G. Lindner, "Skin and hair on-a-chip: in vitro skin models versus ex vivo tissue maintenance with dynamic perfusion," *Lab on a Chip,* vol. 19, pp. 3555-3561, 2013.

[50] Q. Ramadan and F. C. W. Ting, "In vitro micro-physiological immune-competent model of the human skin," *Lab on a Chip,* vol. 16, pp. 1899-1908, 2015.

[51] M. Wufuer, G. Lee, W. Hur, B. Jeon, B. J. Kim, T. H. Choi and S. H. Lee, "Skin-on-a-chip model simulating inflammation, edema and drug-based treatment," *Scientific Reports ,* vol. 6, no. 37471, 2016.

[52] S. Lee, S.-P. Jin, Y. K. Kim, G. Y. Sung, J. H. Chung and J. H. Sung, "Construction of 3D multicellular microfluidic chip for an in vitro skin model," *Biomedical Microdevices ,* vol. 19, no. 22, 2017.

[53] H. J. Song, H. J. Lim, W. Chun, K. C. Choi, J. H. Sung and G. Y. Sung, "Fabrication of a pumpless, microfluidic skin chip from different collagen sources," *Journal of Industrial and Engineering Chemistry,* vol. 56, no. 25, pp. 375-381, 2017.

[54] H. J. Song, H. Y. Lim, W. Chun, K. C. Choi, T. Lee, J. H. Sung and C. Y. Sung, "Development of 3D skin-equivalent in a pump-less microfluidic chip," *Journal of Industrial and Engineering Chemistry,* vol. 60, pp. 355-359, 2018.

[55] G. Sriram, M. Alberti, Y. Dancik, B. Wu, R. Wu, Z. Feng, S. Ramasamy, P. L. Bigliardi, M. Bigliardi-Qi and Z. Wang, "Full-thickness human skin-on-chip with enhanced epidermal morphogenesis and barrier function," *Materials Today,* vol. 21, no. 4, pp. 326-340, 2018.

[56] H. Y. Lim, J. Kim, H. J. Song, K. Kim, K. C. Choi, S. Park and G. Y. Sung, "Development of wrinkled skin-on-a-chip (WSOC) by cyclic uniaxial stretching," *Journal of Industrial and Engineering Chemistry,* vol. 68, pp. 238-245, 2018.

[57] H. M. Jeon, K. Kim, K. C. Choi and G. Y. Sung, "Side-effect test of sorafenib using 3-D skin equivalent based on microfluidic skin-on-a-chip," *Journal of Industrial and Engineering Chemistry,* vol. 82, pp. 71-80, 2020.

[58] B. Jeon, G. H. Lee, M. Wufuer, H. Huang, Y. Choi, S. Kim and T. H. Choi, "Enhanced predictive capacity using dual-parameter chip model that simulates physiological skin irritation," *Toxicology in Vitro,* vol. 68, 2020.

[59] P. Zoio, S. Ventura and A. Oliva, "Biomimetic Full-Thickness Skin-on-a-Chip Based on a Fibroblast-Derived Matrix," *Micro,* vol. 2, no. 1, pp. 191-211, 2022.

[60] N. Sasaki, K. Tsuchiya and H. Kobayashi, "Photolithography-free Skin-on-a-chip for Parallel Permeation Assays," *Sensors and Materials,* vol. 31, no. 1, pp. 107-115, 2018.

[61] N. Sasaki, M. Tatanou, T. Suzuki, Y. Anraku, A. Kishimura, K. Kataoka and K. Sato, "A Membrane-integrated Microfluidic Device to Study Permeation of Nanoparticles through Straight Micropores toward Rational Design of Nanomedicines," *Analytical Sciences,* vol. 32, 2016.

[62] B.-h. Chueh, D. Huh, C. R. Kyrtsos, T. Houssin, N. Futai and S. Takayama, "Leakage-Free Bonding of Porous Membranes into Layered Microfluidic Array Systems," *Analytical Chemistry,* vol. 79, pp. 3504-3508, 2007.

[63] J. Zhang, Z. Chen, Y. Zhang, X. Wang, J. Ouyang, J. Zhu, Y. Yan, X. Sun, F. Wang, X. Li, H. Ye, S. Sun, Q. Yu, J. Sun, J. Ge, Q. Li, Q. Han, Y. Pu and Z. Gu, "Construction of a high fidelity epidermis-on-a-chip for scalable in vitro irritation evaluation," *Lab on a Chip,* vol. 21, pp. 3804-3818, 2021.

[64] H. Stanjek and W. Häusler, "Basics of X-ray Diffraction," *Hyperfine Interactions,* vol. 154, pp. 107-119, 2004.

[65] A. A. Bunaciu, E. G. Udristioiu and H. Y. Aboul-Enein, "X-Ray Diffraction: Instrumentation and Applications," *Critical Reviews in Analytical Chemistry,* vol. 45, pp. 289-299, 2015.

[66] M. Schmitt and J. Popp, "Raman spectroscopy at the beginning of the twenty-first century," *Journal of Raman Spectroscopy,* vol. 37, pp. 20-28, 2006.

[67] D. W. Shipp, F. Sinjab and A. I. Notingher, "Raman spectroscopy: Techniques and applications in the life sciences," *Advances in Optics and Photonics,* 2017.

[68] M. Aziz and A. F. Ismail, "Chapter 5 - X-ray Photoelectron Spectroscopy (XPS)," in *Membrane Characterization*, Elsevier, 2017, pp. 81-93.

[69] E. Ellobody, R. Feng and B. Young, "Chapter 3 - Finite Element Modeling," in *Finite Element Analysis and Design of Metal Structures*, Elsevier, 2014, pp. 31-55.

[70] I. C. Ghiran, "Introduction to Fluorescence Microscopy," in *Light Microscopy*, 2011.

[71] J. W. Lichtman and J.-A. Conchello, "Fluorescence microscopy," *Nature Methods,* vol. 2, pp. 910-919, 2005.

[72] A. Nwaneshiudu, C. Kuschal, F. H. Sakamoto, R. R. Anderson, K. Schwarzenberger and R. C. Young, "Introduction to confocal microscopy," *Journal of Investigative Dermatology,* vol. 132, pp. 1-5, 2012.

[73] P. S. W, "Confocal Laser Scanning Microscopy," *BioTechniques,* vol. 27, no. 5, pp. 992-1004, 2018.

[74] P. L. Sanches, W. Souza, S. Gemini-Piperni, A. L. Rossi, S. Scapin, V. Midlej, Sade Y, A. F. Paes Leme, M. Benchimol, L. A. Rocha, R. B. V. Carias, R. Borojevic, J. M. Granjeiro and A. R. Ribeiro, "Rutile nano–bio-interactions mediate dissimilar intracellular destiny in human skin cells," *Nanoscale Advances,* no. 6, 2019.

[75] S. M. Gupta and M. Tripathi, "A review of TiO2 nanoparticles," *Physical Chemistry,* vol. 56, no. 16, pp. 1639-1657, 2011.

[76] M. M. Viana, V. F. Soares and N. D. S. Mohallem, "Synthesis and characterization of TiO2 nanoparticles," *Ceramics International,* vol. 36, no. 7, pp. 2047-2053, 2010.

[77] K. Thamaphat, P. Limsuwan and B. Ngotawornchai, "Phase Characterization of TiO2 Powder by XRD and TEM," *National Science,* vol. 42, pp. 357-361, 2008.

[78] U. Balachandran and N. G. Eror, "Raman Spectra of Titanium Dioxide," *Journal of Solid State Chemistry ,* vol. 42, pp. 276-282, 1982.

[79] T. K. Sham and M. S. Lazarus, "X-ray photoelectron spectroscopy (XPS) studies of clean and hydrated TiO2 (rutile) surfaces," *Chemical Physics Letters,* vol. 68, no. 2-3, pp. 426-432, 1979.

[80] J. S. Taurozzi, V. A. Hackley and M. R. Wiesner, "Ultrasonic dispersion of nanoparticles for environmental, health and safety assessment – issues and recommendations," *Nanotoxicology,* vol. 5, no. 4, pp. 711-729, 2011.

[81] J. Jiang, G. Oberdörster and P. Biswas, "Characterization of size, surface charge, and agglomeration state of nanoparticle dispersions for toxicological studies," *Journal of Nanoparticle Research ,* vol. 11, pp. 77-89, 2009.

[82] T. Mudalige, H. Qu, D. V. Haute, S. M. Ansar, A. Paredes and T. Ingle, "Chapter 11 - Characterization of Nanomaterials: Tools and Challenges," in *Nanomaterials for Food Applications*, Elsevier, 2019, pp. 313-353.

[83] J. Qi, Y. Y. Ye, J. J. Wu, H. T. Wang and F. T. Lee, "Dispersion and stability of titanium dioxide nanoparticles in aqueous suspension: effects of ultrasonication and concentration," *Water Science & Technology,* vol. 67, no. 1, pp. 147-151, 2013.

[84] Z. Ji, X. Jin, S. George, T. Xia, H. Meng, X. Wang, E. Suarez, H. Zhang, E. M. V. Hoek, H. Godwin, A. E. Nel and J. I. Zink, "Dispersion and Stability Optimization of TiO2 Nanoparticles in Cell Culture Media," *Environmental Science & Technology,* vol. 44, no. 19, pp. 7309-7314, 2010.

[85] E. Sutterby, P. Thurgood, S. Baratchi, K. Kloshmanesh and E. Pirogova, "Microfluidic Skin-on-a-Chip Models: Toward Biomimetic Artificial Skin," *Nano-Micro Small,* 2020.

[86] C. Yavuz, S. N. B. Oliaei, B. Cetin and O. Yesil-Celiktas, "Sterilization of PMMA microfluidic chips by various techniques and investigation of material characteristics.," *The Journal of Supercritical Fluids,* vol. 107, pp. 114-121, 2016.

[87] M. T. J. A. G, S. E. C. M. van de Vijfeijken, C. S. Mulder, V. Vespasiano, A. G. Becking and C. J. Kleverlaan, "Effects of sterilization on the mechanical properties of poly(methylmethacrylate) based personalized medical devices," *Journal of the Mechanical Behavior of Biomedical Materials,* vol. 81, pp. 168-172, 2018.

[88] A. M. D. Wan, D. Devadas and E. W. K. Young, "Recycled Polymethylmethacrylate (PMMA) Microfluidic Devices," *Sensors and Actuators B,* 2017.

[89] Y. Imura, Y. Asano, K. Sato and E. Yoshimura, "A Microfluidic System to Evaluate Intestinal Absorption," *Analytical Sciences,* vol. 25, 2009.

[90] H. Kimura, T. Yamamoto, H. Sakai, Y. Sakai and T. Fujii, "An integrated microfluidic system for long-term perfusion culture and on-line monitoring of intestinal tissue models," *Lab on a Chip,* vol. 8, pp. 741-746, 2008.

[91] V. M. Schoop, N. E. Fusenig and N. Mirancea, "Epidermal Organization and Differentiation of HaCaT Keratinocytes in Organotypic Coculture with Human Dermal Fibroblasts," *Journal of Investigative Dermatology,* vol. 112, no. 3, pp. 343-353, 1999.

[92] A. L. Rusanov, N. G. Luzgina and A. V. Lisitsa, "Sodium Dodecyl Sulfate Cytotoxicity towards HaCaT Keratinocytes: Comparative Analysis of Methods for Evaluation of Cell Viability," *Bulletin of Experimental Biology and Medicine,* vol. 163, no. 2, pp. 284-288, 2017.

[93] P. Zoio, S. Ventura, M. Leite and A. Oliva, "Pigmented Full-Thickness Human Skin Model Basedon a Fibroblast-Derived Matrix for Long-Term Studies," *Tissue Engineering Part C: Methods,* vol. 27, no. 7, pp. 401-443, 2021.

[94] M. C. Moran, R. P. Pandya, K. A. Leffler, T. Yoshida, L. A. Beck and M. G. Brewer, "Characterization of Human Keratinocyte Cell Lines for Barrier Studies," *JID Innovations,* vol. 1, no. 2, 2021.

[95] ProciGenome, "Microfluidic Solutions Provider - Inline Bubble Trap with PTFE Membrane," [Online]. Available: https://www.precigenome.com/bubble-trap. [Accessed october 2022].

[96] I. M. Dijkhoff, B. Petracca, R. Prieux, G. Valacchi, B. Rothen-Rutishauser and M. Eeman, "Cultivating a Three-dimensional Reconstructed Human Epidermis at a Large Scale," *JoVE Journal,* 2021.

[97] E. Montano , M. Vivo, A. M. Guarino, O. Di Martino, B. Di Luccia, V. Calabrò, S. Caserta and A. Pollice, "Colloidal Silver Induces Cytoskeleton Reorganization and E-Cadherin Recruitment at Cell-Cell Contacts in HaCaT Cells," *Pharmaceuticals,* vol. 12, no. 2, 2019.

[98] I. Colombo, E. Sangiovanni, R. Maggio, C. Mattozzi, S. Zava, Y. Corbett, M. Fumagalli, C. Carlino, P. A. Corsetto, D. Scaccabarozzi, S. Calvieri, A. Gismondi, D. Taramelli and M. Dell'Agli, "HaCaT Cells as a Reliable In Vitro Differentiation Model to Dissect the Inflammatory/Repair Response of Human Keratinocytes," *Mediators of Inflammation,* 2017.

[99] C. A. Mini, S. A. C. Dreossi, F. R. Abe, S. S. Maria-Engler and D. P. Oliveira , "Immortalized keratinocytes cells generates an effective model of Epidermal Human Equivalent for irritation and corrosion tests," *Toxicology In Vitro,* vol. 71, 2021.

[100] R. Sun, A. Celli, D. Crumrine, M. Hupe, L. C. Adame, S. D. Pennypacker, K. Park, Y. Uchida, K. R. Feingold, P. M. Elias, D. Ilic and T. M. Mauro, "Lowered Humidity Produces Human Epidermal Equivalents with Enhanced Barrier Properties," *Tissue Engineering Part C: Methods,* vol. 21, no. 1, 2014.

[101] J. Font, F. Braut-Boucher, J. Pichon, M. S. Noel-Hudson, M. P. Muriel, M. Bonnet, J. Wepierre and M. Aubery, "A new three-dimensional culture of human keratinocytes: optimization of differentiation," *Cell Biology and Toxicology,* vol. 10, pp. 353-359, 1994.

[102] N. Okada, Y. Kitano and K. Ichihara, "Effect of Cholera Toxin on Proliferation of Cultured Human Keratinocytes in Relation to Intracellular Cyclic AMP Levels," *The Journal of Investigative Dermatology,* vol. 79, pp. 42-47, 1982.

[103] M. R. Stampfer, "Cholera toxin stimulation of human mammary epithelial cells in culture," *In Vitro Cellular & Developmental Biology,* vol. 18, pp. 531-537, 1982.

[104] D. P. Chopra, K. M. Siddiqui and R. A. Cooney, "Effects of Insulin, Transferrin, Cholera Toxin, and Epidermal Growth Factor on Growth and Morphology of Human Fetal Normal Colon Epithelial Cells," *GASTROENTEROLOGY ,* vol. 92, pp. 891-904, 1987.

[105] D. A. Clark and R. Coker, "Transforming growth factor-beta (TGF-beta)," *The International Journal of Biochemistry & Cell Biology,* vol. 30, no. 3, pp. 293-298, 1998.

[106] D. Hoheisel, T. Nitz, H. Franke, J. Wegener, A. Hakvoort, T. Tilling and H.-J. Galla, "Hydrocortisone Reinforces the Blood–Brain Barrier Properties in a Serum Free Cell Culture System," *Biochemical and Biophysical Research Communications,* vol. 244, no. 1, pp. 312-316, 1998.

[107] S. R. Chowdhury, B. S. Aminuddin and B. H. I. Ruszymah, "Effect os supplementation of dermal fibroblasts conditioned medium on expansion of keratinocytes through enhancing attachment," *Indian Journal of Experimental Biology,* vol. 50, no. 5, pp. 332-339, 2012.

[108] M. Matsusaki, K. Fujimoto, Y. Shirakata, S. Hirakawa, K. Hashimoto and M. Akashi, "Development of full-thickness human skin equivalents with blood and lymph-like capillary networks by cell coating technology," *Journal of Biomedical Materials Research: Part A,* vol. 103, no. 10, pp. 3386-3396, 2015.

[109] M. Odijk, A. D. Van der Meer, D. Levner, H. J. Kim, M. W. Van der Helm, L. I. Segerink, J.-P. Frimat, G. A. Hamilton, D. E. Ingber and A. Van der Berg, "Measuring direct current trans-epithelial electrical resistance in organ-on-a-chip microsystems," *Lab on a Chip,* vol. 15, pp. 745-752, 2015.

[110] J. R. Bickenbach, J. M. Greer, D. S. Bundman, J. A. Rothnagel and D. K. Roop, "Loricrin Expression Is Coordinated with Other Epidermal Proteins and the Appearance of Lipid Lamellar Granules in Development," *Journal of Investigative Dermatology,* vol. 104, no. 3, pp. 405-410, 1995.

[111] E. Boelsma, M. C. H. Verhoeven and M. Ponec, "Reconstruction of a Human Skin Equivalent Using a Spontaneously Transformed Keratinocyte Cell Line (HaCaT)," *Journal of Investigative Dermatology,* vol. 112, no. 4, pp. 489-498, 1999.

[112] S. Shuchat, G. Yossifon and M. Huleihel, "Perfusion in Organ-on-Chip Models and Its Applicability to the Replication of Spermatogenesis In Vitro," *International Journal of Molecular Sciences,* vol. 23, no. 10, 2022.